UNIVERSITY OF SOUTHAMPTON

FACULTY OF NATURAL & ENVIRONMENTAL SCIENCES

Ocean and Earth Science

The Global Meridional Overturning Circulation's Response to Variable Buoyancy Forcing

by

Edward D. Butler

Thesis for the degree of Doctor of Philosophy

January 2015

UNIVERSITY OF SOUTHAMPTON

ABSTRACT

FACULTY OF NATURAL & ENVIRONMENTAL SCIENCES
Ocean and Earth Science

Doctor of Philosophy

THE GLOBAL MERIDIONAL OVERTURNING CIRCULATION'S RESPONSE TO VARIABLE BUOYANCY FORCING

by Edward D. Butler

The meridional overturning circulation (MOC) is a large-scale circulation throughout the global ocean and plays a significant role in the complex global climate system. However, our traditional understanding of the processes driving the MOC has been questioned in recent years. In particular, it has been suggested that surface buoyancy forcing plays little energetic role in driving the MOC. Furthermore, doubt has also been cast over the relationship between meridional overturning and meridional density gradients. In this thesis, we revisit these two ideas using a series of equilibrium and transient numerical ocean simulations.

We begin by diagnosing the global ocean's gravitational potential energy (GPE) budget at steady state in the coupled atmosphere-ocean model HadCM3, utilising the available gravitational potential energy (AGPE) framework to distinguish between the effects of adiabatic and diabatic processes on background GPE and the portion available for adiabatic conversion to kinetic energy (AGPE). We show that surface buoyancy forcing plays an active energetic role in diabatically sustaining large-scale ocean circulation, making available background GPE generated by diapycnal mixing. We then carry out a series of transient experiments using a global configuration of the NEMO ocean modelling framework, periodically varying North Atlantic surface buoyancy forcing over a broad range of timescales. It is shown that the ocean exhibits a highly nonlinear, frequency-dependent response to forcing of the same amplitude, which is well predicted by a scaled overturning streamfunction based on twice-integrated density differences at multi-decadal timescales and longer. Finally, we analyse the AGPE generated by surface buoyancy forcing during each forcing cycle, finding a strong relationship between the AGPE power input by surface buoyancy fluxes and the magnitude of the MOC response. We conclude by discussing the remote effect of North Atlantic buoyancy forcing on lower cell overturning in the Southern Ocean, considering regional changes in AGPE generation.

Contents

List of Figures

List of Tables

Declaration of Authorship

I, Edward D. Butler, declare that the thesis entitled *The Global Meridional Overturning Circulation's Response to Variable Buoyancy Forcing* and the work presented in it are my own and have been generated by me as the result of my own original research. I confirm that:

- this work was done wholly or mainly while in candidature for a research degree at this University;
- where any part of this thesis has previously been submitted for a degree or any other qualification at this University or any other institution, this has been clearly stated;
- where I have consulted the published work of others, this is always clearly attributed;
- where I have quoted from the work of others, the source is always given. With the exception of such quotations, this thesis is entirely my own work;
- I have acknowledged all main sources of help;
- where the thesis is based on work done by myself jointly with others, I have made clear exactly what was done by others and what I have contributed myself;
- parts of this work have been published as:
  - Butler, E. D., K. I. Oliver, J. M. Gregory, and R. Tailleux (2013), The ocean's gravitational potential energy budget in a coupled climate model, Geophys. Res. Lett., 40, 5417-5422.
  - Butler, E. D., K. I. Oliver, J. J.-M. Hirschi, and J. V. Mecking (2014), Predicting global overturning from meridional density gradients, Clim. Dyn. (in submission)

Signed:.....

Date:.....

Acknowledgements

I would like to begin by expressing my sincere gratitude to my supervisory team of Kevin Oliver, Joël Hirschi, and Neil Wells for their patient tutelage as I transitioned from mathematician to oceanographer. Without their support, guidance and trust, granting me the freedom to pursue my own ideas, this thesis would never have been possible. I would also like to thank my advisory panel chair, Alberto Naveira Garabato, for offering me constant encouragement throughout. Further thanks go to the collective staff of the Institute for Complex Systems Simulation for their illuminating introduction to the computational modelling of complex systems.

Without the technical input of both Jeff Blundell and Andrew Coward, conducting my own ocean simulations using the NEMO ocean model would have been far more laborious and stressful. I am extremely grateful to Jonathan Gregory and Remi Tailleux at the University of Reading for making model output from the HadCM3 coupled climate model available for my use in my own analysis and for their invaluable insights and expertise which helped me on the way to my first academic publication. I am also indebted to Jenny Mecking for sharing model output from a high-resolution, stochastic simulation of NEMO that she had run at the GEOMAR Helmholtz Centre for Ocean Research in Kiel.

I am also very grateful to my office mates in 256/16 (Maike Sonnewald, Josie Robinson, Craig Rye, Stephen Fawcett, and Jian Buchan) for their knowledge, company, and friendship. I would also like to thank the wider Marine Systems Modelling group at NOCS for their warm welcome to the world of academia. Great credit must also go to the inspiring birds and wildlife of Hampshire for helping me to maintain perspective and to Coco the kitten for keeping my lap warm.

I would like to express my heartfelt gratitude to my parents, not only for their support throughout my undergraduate and postgraduate education, but also for instilling in me an innate fascination for the natural and physical world and the curiosity and desire to understand its inner workings. Finally, and by no means least, it is impossible for me to adequately convey my thanks to my wonderfully supportive wife, Sarah, who has been so understanding of the lost evenings and weekends that writing this thesis has entailed.

List of Acronyms and Abbreviations

Acronym	**Description**
MOC	meridional overturning circulation
AMOC	Atlantic meridional overturning circulation
NADW	North Atlantic deep water
AABW	Antarctic bottom water
NAO	North Atlantic oscillation
ACC	Antarctic circumpolar current
AAIW	Antarctic intermediate water
GPE	gravitational potential energy
KE	kinetic energy
GPE_{ref}	reference state of minimum GPE
AGPE	available gravitational potential energy
(A)GPE	both GPE and AGPE
AIE	available internal energy
APE	available potential energy, AGPE + AIE
GCM	general circulation model
AOGCM	atmosphere-ocean general circulation model
HadCM3	Hadley Centre Coupled Model, version 3
NEMO	Nucleus for European Modelling of the Ocean
ORCA2	global configuration of NEMO, 2° resolution
ORCA05	global configuration of NEMO, 0.5° resolution
CORE	Coordinated Ocean-ice Reference Experiment
CMIP3	Coupled Model Intercomparison Project, phase 3
CanESM2	Canadian Earth System Model, version 2
BUOY	buoyancy forcing
CON	convection
ADV	advection
DIA	diapycnal mixing
ISO	isopycnal mixing
GM	Gent and McWilliams

List of Symbols

Symbol	Description	Units
ρ	density	kg m^{-3}
ρ_0	density (representative value)	kg m^{-3}
g	gravitational constant	m s^{-2}
z	vertical displacement relative to the surface ($z = 0$)	m
p	pressure	Pa
θ	potential temperature	°C
S	salinity	psu
α	thermal expansion coefficient	°C^{-1}
β	saline contraction coefficient	psu^{-1}
z_{ref}	reference state displacement	m
$\mathbf{u}$	velocity vector (u, v, w)	m s^{-1}
$\mathbf{u}^*$	eddy-induced bolus velocity	m s^{-1}
κ_h	isopycnal diffusion coefficient	m^2 s^{-1}
$\mathbf{K}_{\text{Redi}}$	Redi isopycnal diffusion operator	1
κ_v	background vertical diffusion coefficient	m^2 s^{-1}
F	periodic temperature forcing function	°C
A	sinusoidal amplitude of oscillation	°C
P	period of oscillation	year
Ψ	overturning streamfunction (model simulated)	m^3 s^{-1}
Ψ_p	overturning streamfunction (inferred from meridional pressure gradients)	m^3 s^{-1}
L_x	zonal length scale	m
L_y	meridional length scale	m
h	depth scale	m
$\Delta\rho_y$	meridional density difference	kg m^{-3}
ρ_N	northern boundary density	kg m^{-3}
ρ_S	southern boundary density	kg m^{-3}
f_0	Coriolis parameter (representative value)	s^{-1}
V	basin-scale meridional velocity	m s^{-1}
B	conversion from (A)GPE to KE	W
G	generation of AGPE by surface buoyancy fluxes	W
B^A	areal concentration of B	W m^{-2}
G^A	areal concentration of G	W m^{-2}
Q	surface heat flux	W
I	function describing the penetration of solar radiation	1
ξ_a	APE density	m^2 s^{-2}
b_{ref}	buoyancy relative to reference profile	m s^{-2}

Chapter 1

Introduction

1.1 The large-scale ocean's role in the global climate system

The global ocean is vastly complex, comprising a multitude of component processes that span a broad range of spatial and temporal scales and interact with each other in a nonlinear fashion. For instance, the ocean has numerous dynamical regimes, ranging from small scale turbulence $O(<1\text{m})$, through Kelvin waves $O(10\text{km})$, mesoscale eddies $O(100\text{km})$ and Rossby waves $O(100\text{-}1{,}000\text{km})$, to the large-scale global meridional overturning circulation (MOC) $O(10{,}000\text{km})$. These small-scale physical processes are able to influence the strength, structure, and variability of the large-scale MOC (e.g., small-scale mixing (Munk and Wunsch, 1998), mesoscale eddies (Thomas and Zhai, 2013), Kelvin and Rossby waves (Johnson and Marshall, 2002)). Through its high heat capacity and large-scale circulation, the ocean has the ability to both store and transport heat (Rahmstorf, 2002). It is, thus, an integral component of the global climate system, of which there is currently much discussion in the context of contemporary climate change (e.g. IPCC AR5 - Stocker et al. (2013)). In particular, the ocean's global meridional overturning circulation (MOC) plays an important role in this redistribution of heat

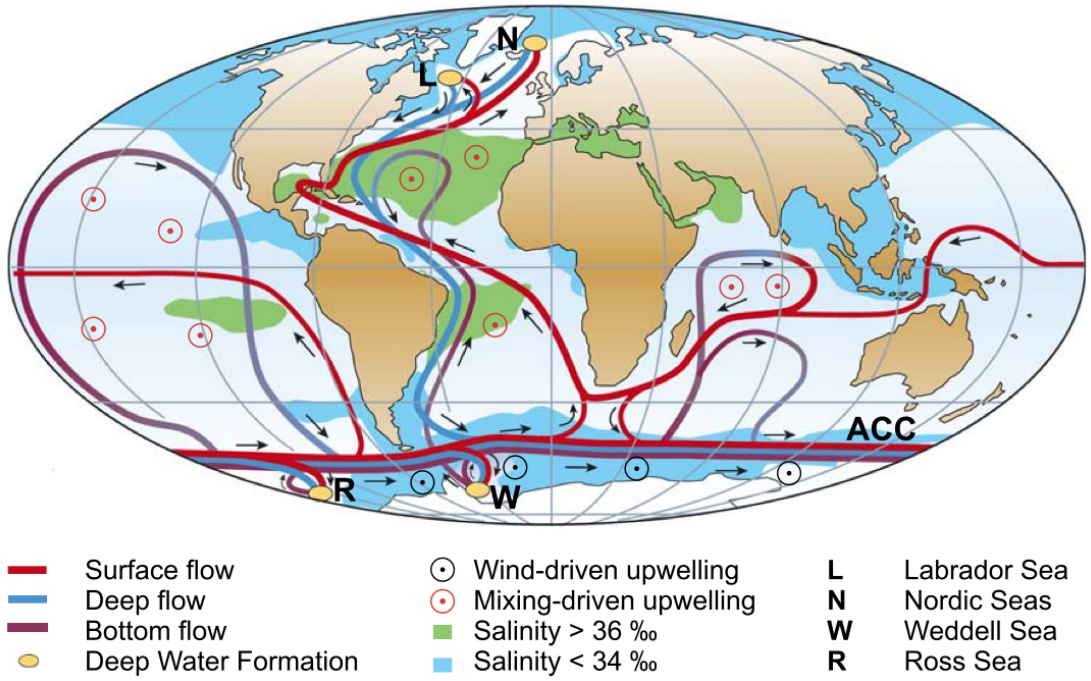

Figure 1.1: A schematic illustration of the global meridional overturning circulation (MOC) depicting the surface flow (red line), deep flow (blue line), and bottom flow (purple line). Regions of high (green shading) and low (blue shading) sea surface salinity are shown, along with the localised regions of deep water formation (yellow circles) in both the North Atlantic and in the Southern Ocean. From: *Kuhlbrodt, T., Griesel, A., Montoya, M., Levermann, A., Hofmann, M., and Rahmstorf, S. (2007), On the driving processes of the Atlantic meridional overturning circulation, Reviews of Geophysics, 45(2).* Reprinted with permission from John Wiley and Sons.

and has been implicated in both past and future climate transitions (Rahmstorf, 2002; Srokosz et al., 2012).

The Atlantic MOC (AMOC) consists of a warm, northward surface flow, high-latitude deepwater formation and a cold, deep return flow to areas of upwelling at low-latitudes and in the Southern Ocean (Kuhlbrodt et al., 2007), as schematically illustrated in Figure 1.1. The AMOC is, in effect, the recirculation of North Atlantic Deepwater (NADW), the dense water mass formed in the Labrador and Nordic Seas. In a global context, the AMOC is referred to to as the "upper cell', overlying a reverse "lower cell' associated with Antarctic Bottom Water (AABW). This AABW is formed around Antarctica in the Weddell and Ross Seas and can be found throughout the abyssal global ocean. The structure of the observed global

overturning streamfunction (constructed using hydrographic sections) is depicted in Figure 1.2, in which the upper and lower overturning cells are both clearly visible. According to observational estimates, the maximum strength of the lower cell is approximately 20 Sv (1 Sv = 10^6 m^3 s^{-1}), though this estimate is subject to large uncertainties (Lumpkin and Speer, 2007). The mean AMOC, or upper cell, strength is approximately 18 Sv, as measured using arrays situated at 26.5°N (Cunningham et al., 2007; McCarthy et al., 2012).

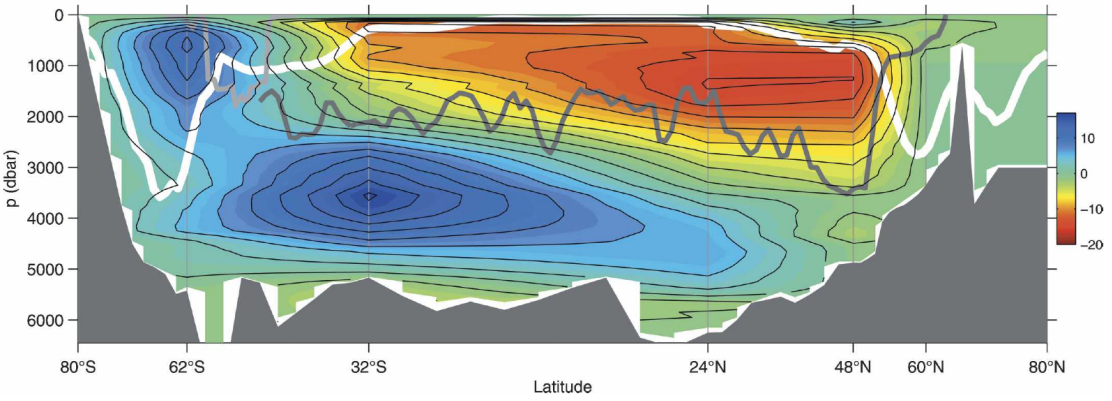

Figure 1.2: The global Lagrangian MOC streamfunction calculated using inverse techniques (contours every 2 Sv). The location of World Ocean Circulation Experiment (WOCE) hydrographic sections are depicted by vertical grey lines. Linear interpolation is used in between sections. The figure also shows the winter mixed layer depth (white), the mean depth of mid-ocean ridges (dark grey), and the profile of the Drake Passage (light gray). From: *Lumpkin, R. and Speer, K. (2007), Global Ocean Meridional Overturning, Journal of Physical Oceanography, 37(10):2550-2562.* ©American Meteorological Society. Used with permission.

The difference in temperature between the poleward surface flow and the deep return flow of the AMOC results in a net meridional heat transport of approximately 1.3 TW in the Atlantic at approximately 25°N (Ganachaud and Wunsch, 2000; Lumpkin and Speer, 2007; Johns et al., 2011). This heat transport is responsible for significant anomalous warming of the North Atlantic region, with a coupled climate model experiment suggesting that this is locally as much as 8°C (Vellinga and Wood, 2002). Indeed, observations show that the region overlying the northeastern Atlantic is 5-10°C warmer than the zonal average air temperature (Rahmstorf and Ganopolski, 1999). The potential climatic consequences of variability in the AMOC are broad and far-reaching, impacting air temperature

(Stouffer et al., 2006), sea-level (Brunnabend et al., 2014), biological productivity (Schmittner, 2005), ecosystem services (Rocha et al., 2015), deep ocean heat storage (Kostov et al., 2014), the ocean uptake of carbon (Zickfeld et al., 2008), storm-track intensity and global patterns of rainfall (Vellinga and Wood, 2002).

1.2 Understanding the steady-state AMOC

1.2.1 The Stommel box model of 'thermohaline circulation'

The MOC was traditionally referred to as the 'thermohaline circulation', thought to be driven by the meridional density difference between high and low-latitudes. In the present ocean, these density differences are set up by high-latitude cooling leading to the formation of dense water, which is then convectively mixed throughout the water column. The earliest conceptual model of thermohaline circulation is that of Stommel (1961). Whilst not initially conceived to describe meridional overturning, this model has since been widely utilised as the theoretical basis and inspiration of many conceptual models of the AMOC.

In the Stommel (1961) model (depicted schematically in Figure 1.3), the thermohaline volume transport is assumed to be proportional to the density difference between the two boxes. This density difference is jointly dependent on both temperature ('thermo') and salinity ('haline'). The dense high-latitude box is characterised by cold, fresh water whilst the light low-latitude box is characterised by warm, saline water. Two different equilibrium modes of overturning, Ψ, exist in the Stommel (1961) model: a strong, thermally-driven circulation with high-latitude deepwater formation and a weak reversed salinity-driven circulation with low-latitude deepwater formation. Their stability is determined as a function of the freshwater forcing parameter, F (the freshwater flux from low to high-latitudes). Linear stability analysis shows that there exists a range of freshwater forcing for which both modes of circulation are stable. Consequently, changing freshwater

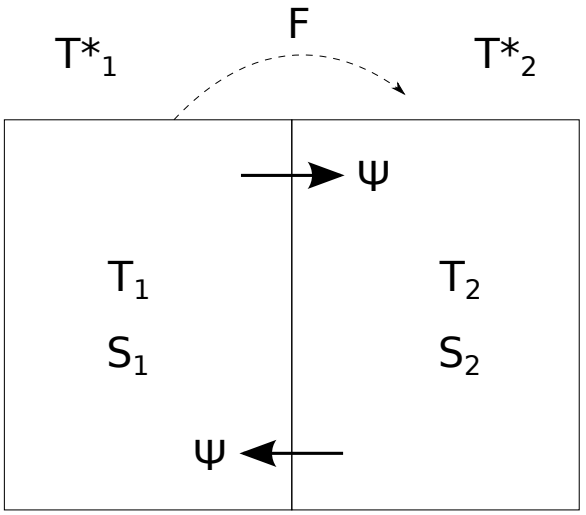

Figure 1.3: A schematic depiction of the Stommel (1961) box model of thermohaline circulation. Each box is well-mixed with salinity, S, and temperature, T. There is a freshwater flux, F, from low-latitudes to high-latitudes, whilst temperature, T, restores to the overlying atmospheric temperature, $T*$. The thermohaline transport Ψ is linearly proportional to the density difference, $\rho_2 - \rho_1$, between boxes. Density is a function of both salinity and temperature.

flux can trigger an abrupt, nonlinear change in circulation that can persist even when the flux is restored to its original value.

When expressing the system in (F, Ψ) space, we see stability patterns known as hysteresis loops in which abrupt, irreversible transitions can occur (as schematically illustrated in Figure 1.4). Furthermore, this simple model also exhibits both positive and negative feedback effects. For example, the positive salt advective feedback (see, for instance, the review of Kuhlbrodt et al. (2007)), in which the thermally-dominated mode of circulation (for which the colder, but fresher, high-latitude box is denser) advects salt from the more saline low-latitudes to high-latitudes, further increasing high-latitude density and supporting continued overturning. Conversely, if the model is in the salinity-dominated mode of circulation with low-latitude deepwater formation, there is no export of salt to high-latitudes and the prospect of high-latitude deepwater formation recommencing is further inhibited. Despite the simplicity of the Stommel (1961) box model, such models can be highly instructive. Indeed, bistability, hysteresis loops, and positive salt advection feedbacks have all since been observed in much more complex coupled climate

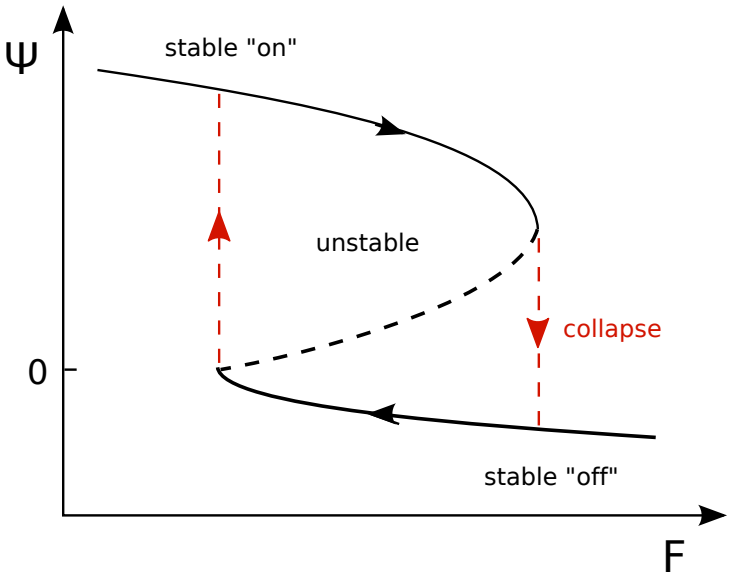

Figure 1.4: A schematic illustration of a hysteresis loop in the Stommel (1961) box model on a diagram of overturning strength, Ψ, against freshwater forcing, F. Solid black lines depict stable model solutions; the upper and lower curves correspond to overturning circulations in which high-latitude convection is switched "on" and "off", respectively. There exists an intermediate range of F for which there are two stable solutions and the dashed black line depicts the corresponding unstable solution that exists within this range. The dashed red lines indicate where abrupt transitions between the stable "on" and the stable "off" modes can occur. The arrows demonstrate the hysteresis loop that forms when F is incrementally increased and then incrementally decreased.

models (e.g., Manabe and Stouffer (1988); Rahmstorf et al. (2005); Hawkins et al. (2011)).

1.2.2 Driving processes of the AMOC

In recent years, the question about which physical processes can actually be considered to be mechanically 'driving' the AMOC has come to fore (see Kuhlbrodt et al. (2007) for a comprehensive review of this literature). We adopt the convention of Kuhlbrodt et al. (2007) and consider a process to be driving meridional overturning if it is providing a portion of the mechanical energy required to sustain it. Sandström (1908) conducted a series of thermally-forced tank experiments in which he found that differential heating and cooling at the surface could only drive a shallow overturning circulation that was confined to the surface layer.

Munk and Wunsch (1998) argued that without an input of potential energy, dense water masses formed at high-latitudes would simply fill the deep ocean within $O(1000)$ years. Therefore, the strength of the overturning circulation must be rate limited by the amount of energy available to upwell this dense water (i.e., to overturn the ocean, as opposed to fill the ocean). Munk and Wunsch (1998) suggested that this energy is supplied by turbulent diapycnal mixing occurring throughout the global ocean. However, doubt has been cast over whether interior mixing rates are large enough to supply the required energy (Wunsch and Ferrari, 2004).

Alternatively, it has been hypothesised that the majority of the AMOC upwelling occurs in the Southern Ocean through wind-driven Ekman pumping (e.g., Webb and Suginohara (2001)). More specifically, Ekman divergence brings deep water to the surface, whereupon surface Ekman transport returns it northward (Toggweiler and Samuels, 1995; Samelson, 2004). This interpretation is supported by Toggweiler and Samuels (1998), in which it was demonstrated that a vigorous wind-driven overturning circulation still exists in the limit of no vertical mixing. The location of regions of wind-driven upwelling and mixing-driven upwelling are schematically illustrated in Figure 1.1. Due to the body of evidence that suggests diapycnal mixing and wind-driven upwelling play an important role in sustaining the present-day ocean overturning circulation, the term 'meridional overturning circulation' is now favoured within the literature (as opposed to 'thermohaline circulation'), because it provides an accurate geographical description of what is observed without alluding its driving processes (Wunsch, 2002).

The relative roles of different oceanic processes in the driving of global ocean circulation can be quantified by evaluating their contribution to the ocean's mechanical energy budget (e.g., Munk and Wunsch (1998); Wunsch and Ferrari (2004); Gregory and Tailleux (2011)). However, large uncertainties still exist in the magnitude of the ocean's sources and sinks of mechanical energy based on observations (Wunsch and Ferrari, 2004) and the energetics of realistic ocean models are not well understood (in particular, the effects of parameterised model processes) (Hughes et al., 2009).

Therefore, the role that surface buoyancy forcing plays in driving the MOC remains much debated. Whilst conventional energetics arguments suggest that the best estimate of the mechanical energy supplied by surface buoyancy fluxes is 0 TW (Wunsch and Ferrari, 2004), it is clear from a multitude of modelling studies that the MOC is sensitive to changes in surface buoyancy forcing (e.g., Thorpe et al. (2001); Stouffer et al. (2006); Hogg et al. (2013) amongst many others). Kuhlbrodt et al. (2007) argue that although driving processes (supplying mechanical energy) are required to return dense water to the surface, they do not determine where this dense water is formed and where downwelling occurs and, thus, the overall structure of the MOC. Surface buoyancy fluxes, however, do play an important role in the location of deepwater formation (though this process is, of course, the result of a complex combination of factors including: local air-sea buoyancy fluxes, brine rejection from the formation of sea ice, open ocean convection, sill overflows, and entrainment processes - see Kuhlbrodt et al. (2007) and references therein). The effect of surface buoyancy fluxes have, consequently, been likened to that of 'valve', releasing potential energy generated by the Southern Ocean Ekman 'pump' (Samelson, 2004).

1.2.3 The development of conceptual box models of the AMOC

In addition to direct energetic considerations, whether a simple relationship can be found between meridional volume transport and meridional density gradients (such as the one used in the Stommel (1961) model of 'thermohaline' circulation) has also been questioned (e.g., de Boer et al. (2010)). This is because the ocean's meridional velocity in geostrophic balance is determined by zonal pressure gradients, as opposed to meridional pressure gradients (due to the influence of the Coriolis effect). However, evidence supporting a linear relationship between meridional overturning and meridional density gradients has been found in a number of modelling studies. For example, Rahmstorf (1996) found a strong relationship

between the strength of the AMOC and the deep-ocean meridional density difference ($\Psi \sim \Delta\rho$) in a global ocean simulation. However, Thorpe et al. (2001) found a linear relationship between the strength of the AMOC and once-integrated upper-ocean meridional density gradients in a global coupled climate model ($\Psi \sim \Delta\rho H$, where H is the overturning scale depth) and Hughes and Weaver (1994) found a linear relationship between the strength of meridional overturning and twice-integrated meridional density gradients in a series of idealised two-basin ocean-only simulations ($\Psi \sim \Delta\rho H^2$). It is, therefore, evident that there remains a lack of cross-model consensus as to the exact nature of the relationship between meridional overturning and meridional density gradients. In particular, it is not clear how $\Delta\rho$ and H should be defined in a consistent, rather than simply empirical, manner (de Boer et al., 2010).

Attempts have also been made to relate the strength of meridional overturning, Ψ, to the vertical diffusivity coefficient, κ. By combining the geostrophic relationship described above (under the assumption that zonal and meridional velocities are linearly proportional) with an advective-diffusive tracer balance (as discussed in the context of ocean energetics by Munk and Wunsch (1998)), one can show that $\Psi \sim \kappa^{2/3}\Delta\rho^{1/3}$ (e.g., Park and Bryan (2000)). Whilst this relationship has been tested in numerous idealised modelling studies with mixed results (see Park and Bryan (2000) for an overview), Park and Bryan (2000) found good agreement with the $\kappa^{2/3}$ scaling law in single-hemisphere configurations of both a z-coordinate and an isopycnal-coordinate model. However, they did find that this scaling underestimated the strength of meridional overturning when κ is small. In this limit, wind-driven transport plays an increasingly significant role. When revisited in a global ocean model, Dijkstra (2008) found that a $\kappa^{2/3}$ law held in the Pacific, but a $\kappa^{1/3}$ law held in the Atlantic, citing the fact that advective processes, rather than an advective-diffusive balance, control the pycnocline depth in the Atlantic as a possible explanation for the difference in scaling behaviour. The timescale over which such a diffusivity scaling is valid is set by the centennial/millennial diffusive timescale and, thus, makes it unsuitable for the study of higher frequency variability in ocean overturning. This long timescale also makes it more challenging to

verify whether this scaling holds in high-resolution ocean simulations or, indeed, in the physical ocean. There, thus, remains a great deal of uncertainty as to whether this scaling is robust or not.

Despite the debate surrounding simple scales for meridional volume transport, many developments of the Stommel (1961) box model have been posited since its inception, incorporating our growing understanding of the MOC as a mechanically-driven circulation as opposed to a simple 'thermohaline'-driven phenomenon. One of the most immediate drawbacks of Stommel (1961)-style box models is the fact that the low-latitude ocean is not well-represented by a homogenous, well-mixed box. A well-mixed low-latitude box requires an implicit source of mechanical energy (Johnson et al., 2007) (supplied by Stommel (1961) through external stirring devices that play no dynamical role in the evolution of the system). A more realistic representation of North Atlantic stratification is as a two layer ocean with a buoyant low-latitude surface layer separated by a (variable depth) pycnocline from the dense deep ocean (which connects to the surface at high-latitudes). The northward meridional volume transport is then taken to be jointly proportional to the density difference between the two layers and the square of the depth of the low-latitude pycnocline (e.g., Gnanadesikan (1999); Nilsson and Walin (2001); de Boer et al. (2010)). This is an important development in conceptual modelling of the MOC as it allows the upwelling branch, which Munk and Wunsch (1998) argued was rate-limiting, to be parameterised. For example, Nilsson and Walin (2001) explored the nonlinear impact that different physically well-motivated parameterisations of upwelling balanced by diapycnal mixing have on traditional thermohaline feedbacks, finding that overturning can either be enhanced or impeded by the input of freshwater depending on the mixing parameterisation used.

It is also apparent from Figure 1.1 and Figure 1.2 that the upper overturning cell is not confined to the North Atlantic and is, in fact, an inter-hemispheric circulation. Gnanadesikan (1999) constructed a simple model of an inter-hemispheric upper cell using the low-latitude pycnocline depth as the prognostic variable. This model is arguably the most important development in the conceptual modelling of the AMOC since the Stommel (1961) box model was first proposed. The effects

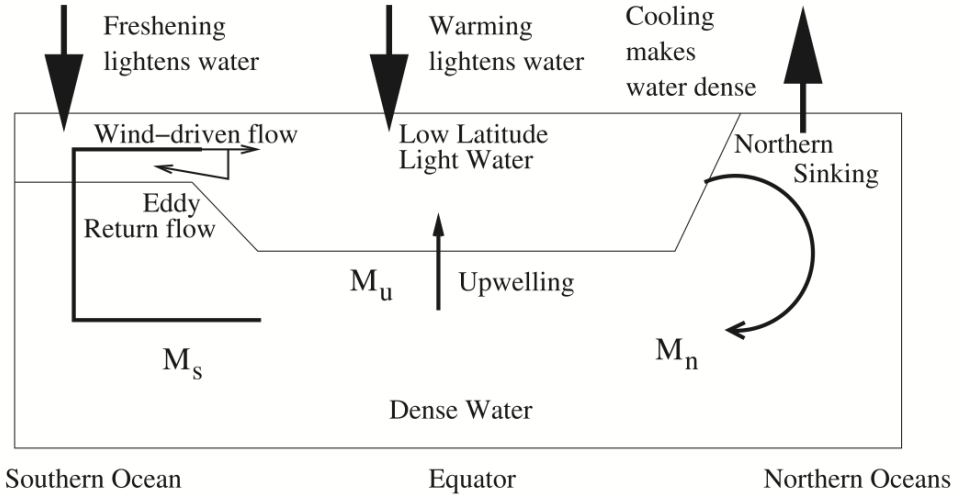

Figure 1.5: A schematic illustration of the Gnanadesikan (1999) model of the global pycnocline. From: *Gnanadesikan, A. (1999), A simple predictive model for the structure of the oceanic pycnocline, Science, 283(5410):2077-2079.* Reprinted with permission from AAAS.

of northern deepwater formation and low-latitude upwelling are both incorporated in this model, but the traditional configuration is extended to include the effects of Southern Ocean controls on the depth of the low-latitude pycnocline (namely, the northward Ekman flux of dense water and the opposing eddy-induced return flow of light water). This model highlights the role that Southern Ocean processes play in setting the depth of the global pycnocline (Gnanadesikan, 1999) and has been highly influential in subsequent modelling studies of the AMOC (e.g. Johnson et al. (2007); Fürst and Levermann (2011) amongst many others). However, unlike the Stommel (1961) box model, this model does not allow thermohaline feedbacks since it is a function of pycnocline depth only (with a prescribed density contrast between the light and dense ocean partitions). Furthermore, it has only one solution, not permitting the multiple equilibria seen previously (Johnson et al., 2007). These two different conceptual approaches to modelling the AMOC have been integrated into a single model by Johnson et al. (2007), reconciling the notion of a mechanically-driven circulation with one that is influenced by thermohaline forcing and feedbacks. This model, subsequently, recovers the multiple equilibria of Stommel (1961).

Due to the intrinsic nature of conceptual models, they represent informative simplifications of the real system. These simplifications are intended to be the minimal set of processes necessary to accurately describe the fundamental dynamics of the system. More complicated models might, in principle, provide a better representation of reality. However, the more complicated a conceptual model becomes, the harder it is to interpret. Reconciling these conflicting notions presents a great challenge when attempting to describe and understand a phenomenon as complex as the MOC. It is clear that establishing a robust and universal scale for meridional transport is vital to the development of conceptual models of the meridional overturning circulation and our understanding of its variability.

1.3 Variability in the AMOC

Over the course of the last decade, direct measurements of the AMOC have been made using the RAPID mooring array situated at 26.5°N. These observations have demonstrated that the AMOC is not a constant circulation, but undergoes large amplitude oscillations on short timescales (e.g., Cunningham et al. (2007); Kanzow et al. (2009); McCarthy et al. (2012)). This high frequency variability has been linked to changes in Ekman transport (due to fluctuations in surface wind) and to changes in the ocean's thermal wind balance (due to fluctuations in ocean density) (Hirschi et al., 2007). Observed variability in the strength of the AMOC has been shown to have a direct impact on the upper ocean heat content in the subtropical Atlantic (Cunningham et al., 2013; Sonnewald et al., 2013; Bryden et al., 2014). Fluctuations in the meridional heat transport associated with the AMOC have subsequently been implicated in the onset of northwestern Europe's cold winter of 2010-2011 and the intensification of the summer 2010 Atlantic hurricane season, with variability in regional air-sea fluxes only contributing 10% to the reduction of ocean heat content north of 25°N (Bryden et al., 2014).

Due to the AMOC's climatic importance and its dependence on surface buoyancy fluxes, there has been much speculation as to whether the strength of the AMOC

is weakening (or will weaken) in response to climate change (e.g., Thorpe et al. (2001)). Recent measurements by the RAPID mooring array show that a decline in the strength of the AMOC was observed between 2004 and 2012 (Smeed et al., 2014), but the observational timeseries is still too short to determine whether this is a forced trend or simply the result of interannual variability (Roberts et al., 2014). Due to the limited observational dataset, numerical general circulation models (GCMs) are, thus, essential for the study of both short-term and long-term AMOC variability (in addition to the simulation of future climates, past climates, and alternative climates).

The focus of this thesis will be on longer multi-decadal through millennial timescale variability, with particular emphasis on the response to external buoyancy forcing. A strong multi-decadal signal in mean North Atlantic temperature has been observed in the past 150 years of instrumental data and over many centuries in paleoclimate reconstructions. This oscillation in surface temperature is known as the Atlantic Multidecadal Oscillation and has been linked to variability in the AMOC (Knight, 2005). The proposed mechanisms for explaining long timescale AMOC variability in numerical modelling studies vary. For example, multi-decadal AMOC variability (of period 40-80 years) simulated in a coupled climate modelling study found that it was instigated by low frequency variability in atmospheric forcing that was similar in pattern to the North Atlantic Oscillation (NAO) with heat flux anomalies the dominant factor (Delworth and Greatbatch, 2000). Conversely, it has been suggested that multi-decadal and centennial variability in the AMOC in HadCM3 is predominantly driven by variations in high-latitude salinity due to the multi-decadal advection of salinity anomalies from the tropics (triggered by rainfall-related feedbacks) (Vellinga and Wu, 2004; Jackson and Vellinga, 2013) and fluctuations in Arctic freshwater export (Jackson and Vellinga, 2013). In a simplified box model study, Griffies and Tziperman (1995) found that AMOC variability arose from a combination of these two factors, with stochastic variability in atmospheric forcing exciting an internal oscillation driven by advective feedbacks.

Variability in overturning transport at the northern, high-latitude basin boundary can be rapidly propagated throughout the basin via a combination of western boundary waves and internal Rossby waves (Johnson and Marshall, 2002). Propagation from high-latitudes to the equator can occur in a matter of months (Czeschel et al., 2010). This signal is then transmitted across the equator and along the eastern boundary from which westward-propagating Rossby waves communicate anomalies to the ocean interior (Johnson and Marshall, 2002). This wave propagation theory was supported by the idealised modelling study of Lucas et al. (2005), in which Rossby waves were found to play an important role in determining the AMOC response to periodic perturbations in the meridional density gradient (on decadal timescales). On much shorter timescales, the conceptual model of Hirschi et al. (2007) has also demonstrated how Rossby waves can induce sub-annual variability in the AMOC due to phase differences between the eastern and western boundaries.

In addition to sub-annual and decadal variability in the AMOC, it is also thought that large amplitude, millennial-timescale reorganisations of ocean overturning have occurred in the past (see the review of Rahmstorf (2002)). These transitions have been implicated in the abrupt 'Dansgaard-Oeschger' warming events that occurred during the last glacial period (Rahmstorf, 2002). Such oscillations have been recreated in general circulation models of glacial climate (e.g., Ganopolski and Rahmstorf (2001)). Due to a larger freshwater input between 40°N and 60°N (compared to the present day climate), the stable AMOC simulated during this period was a weak overturning cell with no high-latitude deepwater formation. However, small changes in freshwater flux in the Nordic Seas were sufficient to trigger the rapid onset of a vigorous 'flush' oscillation, in which deepwater formation shifts from low-latitudes to high-latitudes and the build-up of potential energy in the water column is rapidly released (Ganopolski and Rahmstorf, 2001). This marginally unstable mode can then persist for $O(100$ years) and the change in circulation can lead to an 8°C increase in air temperature over the northern North Atlantic. Such nonlinear responses to small perturbations are reminiscent of the abrupt transitions that have been seen to occur in simple box models (as described

in Section 1.2.1). In this way, the AMOC can act as an amplifier of small changes in the complex climate system (Rahmstorf, 2002).

To conclude this introduction, it is clear that the AMOC can vary across a multitude of timescales and respond to external buoyancy forcing in a highly nonlinear way. It is likely that different physical processes might drive AMOC variability on different timescales. As described above, wind-driven fluctuations in Ekman transport can induce high-frequency variability in the AMOC, whilst the propagation of buoyancy anomalies and changes in internal stratification have been shown to influence ocean circulation on longer timescales. However, the energetics and, therefore, the driving processes of the transient AMOC have yet to be fully explored or understood.

1.4 An outline of this thesis

The aim of this thesis is to investigate the processes driving the global meridional overturning circulation, at both steady state and in response to variability in external buoyancy forcing, using a series of general circulation model (GCM) experiments. In particular, I will re-examine some of the traditional ideas about meridional overturning that have been questioned in recent years. Namely, are large-scale meridional density gradients really predictive of meridional volume transport and, if so, at what timescales? Furthermore, do surface buoyancy fluxes really play little energetic role in sustaining meridional overturning?

Firstly, I will begin by diagnosing the ocean's gravitational potential energy (GPE) budget in the control simulation of the coupled climate model HadCM3 in order to identify the sources and sinks of GPE in a model ocean (Chapter 2). In recent years there has been an increased discussion about what portion of GPE generation can actually be used to power ocean circulation (e.g. Hughes et al. (2009); Tailleux (2009)). To quantify this, I will also diagnose the ocean's available gravitational potential energy (AGPE) budget. This will enable us to discuss GPE and AGPE in a unified way, highlighting and explaining both the similarities and differences

between the GPE and AGPE frameworks for different physical processes, such as large-scale advection and surface buoyancy forcing.

Despite the debate that exists over the energetic driving processes of the AMOC, it remains a popular idea in physical oceanography that the strength of the AMOC is determined by meridional density differences between low and high-latitudes. However, this concept has been questioned by de Boer et al. (2010). In Chapter 3, I will investigate whether such a relationship does exist in a global configuration of the NEMO ocean modelling framework (Madec, 2008), focussing on the role of western boundary density gradients. I will construct a scaled overturning stream-function that retains function of depth, testing it in both the upper and abyssal ocean using a series of transient experiments in which air temperature over the North Atlantic is periodically varied over a broad range of timescales.

I will then combine both of these ideas in Chapter 4, exploring the local, transient energetics of the AMOC response to periodic surface buoyancy forcing, diagnosing the potential energy input by each forcing scenario and the subsequent conversion to kinetic energy (KE) that occurs along the western boundary. Finally, I will present a hypothesis of how variability in North Atlantic buoyancy forcing can affect lower cell overturning in the Southern Ocean by relating its strength to the amount of potential energy made available regionally.

The implications of this work, along with potential avenues for future research, are discussed in Chapter 5.

Chapter 2

Diagnosing the ocean's gravitational potential energy budget in a coupled climate model

The work presented in this chapter has been published in a peer-reviewed journal:

Butler, E. D., K. I. Oliver, J. M. Gregory, and R. Tailleux (2013), The ocean's gravitational potential energy budget in a coupled climate model, Geophys. Res. Lett., 40, 5417-5422.

2.1 Introduction

Global ocean circulation has a significant effect on the Earth's climate, but the relative importance of the processes responsible for driving global ocean circulation are still debated (e.g., Kuhlbrodt et al. (2007)). It has been postulated that the ocean's budget of mechanical energy, comprising kinetic energy (KE), gravitational potential energy (GPE), and the work of expansion and compression, can provide insights into the nature of this circulation and its driving processes (e.g., Munk

and Wunsch (1998); Oliver and Edwards (2008); Urakawa and Hasumi (2009); Tailleux (2010); Gregory and Tailleux (2011)). In this study, we focus our analysis on the ocean's GPE budget.

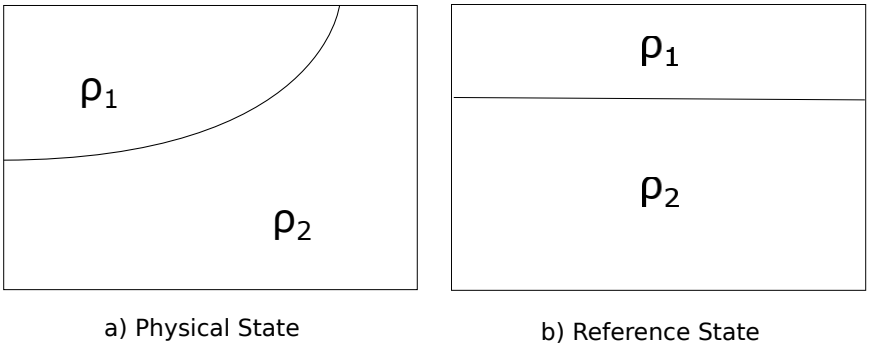

Figure 2.1: A schematic illustration of a) a physical ocean state in which light water (ρ_1) overlies dense water (ρ_2) (separated by a pycnocline which outcrops at high latitudes) and b) its corresponding reference state of minimum GPE obtained through reversible, adiabatic rearrangement of water masses.

Sources of GPE, such as turbulent diapycnal mixing (e.g., Munk and Wunsch (1998)) and the wind-driven upwelling of dense water (e.g., Webb and Suginohara (2001)), are required to sustain the meridional overturning circulation. It is a widely held idea that surface buoyancy forcing cannot supply this mechanical energy and that the work done by buoyancy forcing is effectively zero (Wunsch and Ferrari, 2004; Kuhlbrodt et al., 2007). This is because buoyancy is gained and lost at approximately the same pressure level (i.e. the surface) and, thus, has a negligible effect on globally integrated GPE (Huang and Jin, 2006). However, it has been argued that analysing GPE alone can produce misleading conclusions (Hughes et al., 2009) and that a distinction must be made between overall GPE and the portion of this which can be converted to KE by adiabatic processes, available gravitational potential energy (AGPE). AGPE is defined to be the difference between the GPE of the physical state and the GPE of the reference state, which is a hypothetical state of minimum GPE achieved through reversible, adiabatic rearrangement of water masses (e.g., Lorenz (1955); Toggweiler and Samuels (1998); Huang (1998)). The reference state of an idealised ocean is illustrated schematically in Figure 2.1.

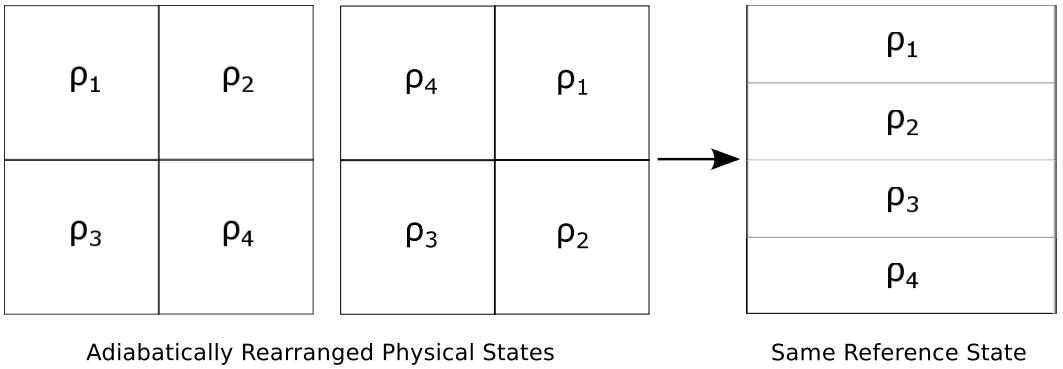

Figure 2.2: A schematic illustration of the effect of adiabatic processes on reference state GPE: the left panel shows two adiabatic rearrangements of an idealised 4-box ocean (for which $\rho_4 > \rho_3 > \rho_2 > \rho_1$) and the right panel demonstrates that they have identical reference states. Note: an incompressible equation of state is assumed.

Not all oceanic processes affect GPE and AGPE in the same manner. Physical processes in the ocean can be identified as adiabatic or diabatic through their effects on the GPE reference state (Winters et al., 1995; Tailleux, 2009). Adiabatic processes are defined here (according to Winters et al. (1995)) as those that do not involve the transfer of heat or molecular mass between fluid parcels (and a diabatic process as one that is not adiabatic). Adiabatic processes move fluid parcels reversibly without mixing and, therefore, do not alter the frequency distribution of temperature or salinity and, accordingly, do not affect the GPE of the reference state (as illustrated schematically in Figure 2.2). Consequently, adiabatic processes have the same effect on both GPE and AGPE. The AGPE budgets of ocean models with idealised configurations have been analysed previously (e.g., Toggweiler and Samuels (1998); Huang (1998); Hughes et al. (2009)) and AGPE has been discussed extensively in a theoretical context by Tailleux (2009). Hughes et al. (2009) demonstrated that spatial variations in surface buoyancy forcing can generate AGPE from background GPE, without changing the GPE of the physical ocean (as illustrated schematically in Figure 2.3).

However, the energetics of the global ocean and realistic ocean models are still poorly understood, even at steady state (Wunsch and Ferrari, 2004; Hughes et al., 2009). In this chapter, we present both the GPE and AGPE (hereafter (A)GPE) budgets from the control simulation of the atmosphere–ocean general circulation

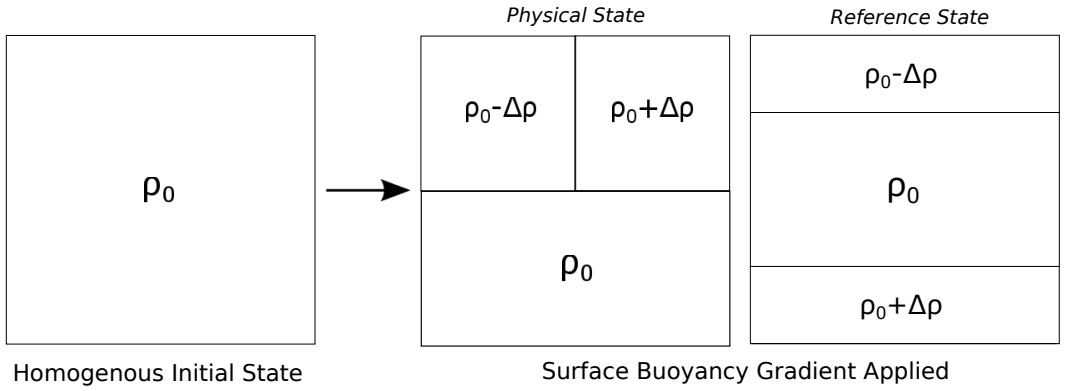

Figure 2.3: A schematic illustration of the effect of spatial variations in surface buoyancy forcing on AGPE: the application of a buoyancy gradient across the surface layer of a homogenous initial state has no net effect on globally-integrated GPE, but it does reduce the GPE of the reference state by lowering its centre of mass ($\Delta\rho > 0$).

model (AOGCM) HadCM3 in a unified fashion. We begin by describing the method by which the GPE and AGPE budgets are calculated in Section 2.2. The globally integrated (A)GPE budgets are then presented in Section 2.3.1 and its local composition (by latitude) is given in Section 2.3.2. Finally, the implications of these results are discussed in Section 2.4.

2.2 Method

Model output from the control simulation of the Hadley Centre coupled model, version 3 (HadCM3) is used in this study. HadCM3 is a coupled atmosphere-ocean global climate model that requires no flux adjustments to maintain a stable, reasonably realistic climate (Gordon et al., 2000) and was used in both the Third and Fourth IPCC climate assessments. The oceanic component has a nonlinear equation of state, realistic bottom topography, a rigid lid, 20 depth levels and a horizontal resolution of 1.25°.

The local contribution to global GPE of a single model cell is defined to be equal to the volume integral of the product of density, gravity and vertical displacement. In the fixed geometry of a volume conserving, z-coordinate ocean model, cell

volume, V, and vertical displacement (defined at the centre of the cell), z, are time-invarient. Consequently, differentiation with respect to time yields:

$$\frac{\partial \mathrm{GPE}_{(i,j,k)}}{\partial \mathrm{t}} = g\frac{\partial \rho_{(i,j,k)}}{\partial t} V_{(i,j,k)} z_{(i,j,k)} \tag{2.1}$$

in which g = the gravitational constant, ρ = density, V = volume, z = vertical displacement, and (i, j, k) are the model cell coordinates. z must be defined relative to the surface to avoid spurious GPE generation and dissipation associated with the conservation of volume, rather than mass (see Appendix A). Density is a function of potential temperature θ, salinity S, and pressure p. In an Eulerian framework, we have:

$$\frac{1}{\rho_0}\frac{\partial \rho}{\partial t} = -\alpha\frac{\partial \theta}{\partial t} + \beta\frac{\partial S}{\partial t}; \quad \alpha := -\frac{1}{\rho_0}\frac{\partial \rho}{\partial \theta}, \quad \beta := \frac{1}{\rho_0}\frac{\partial \rho}{\partial S} \tag{2.2}$$

AGPE is defined as the difference between the GPE of the physical state and the GPE of the reference state, $\mathrm{GPE}_{\mathrm{ref}}$: AGPE = GPE − $\mathrm{GPE}_{\mathrm{ref}}$. The widely used quasi-geostrophic approximation for available potential energy (e.g. Toggweiler and Samuels (1998)) is inadequate for distinguishing between adiabatic and diabatic processes, because its reference state is constructed from horizontally averaging the density field and cannot, in general, be obtained through adiabatic readjustment (Huang, 2005). Instead, reference states of minimal GPE are calculated here according to the sorting algorithm devised by Huang (2005). Model cells are sorted according to density and rearranged adiabatically into layers spanning the global ocean, such that the densest cell is spread across the bottom of the ocean and the lightest is at the surface. Variations in ocean area with depth are accounted for in this calculation, such that the reformed layer has a thickness, $\Delta z_{(i,j,k)}$, given by:

$$\Delta z_{(i,j,k)} = \frac{V_{(i,j,k)}}{A(z_{\mathrm{ref}})} \tag{2.3}$$

in which $V_{(i,j,k)}$ = cell volume and $A(z_{\mathrm{ref}})$ = ocean area at z_{ref}. This sorting procedure is complicated, however, by the use of a nonlinear equation of state so

that the order of the sorted density profile depends on the pressure at which it is evaluated. Consequently, the method of Huang (2005) uses an iterative approach to find a reference state that is, by construction, stably stratified. Model cells are initially sorted according to density evaluated at the bottom of the ocean and the ocean is then "refilled" accordingly. Fluid parcels that lie above a smaller (shallower) reference pressure in the initial reference state are then sorted again according to their density evaluated at this new reference level. This process is repeated until the surface is reached. It should be noted that the ocean is treated as a single basin when constructing the reference state and, consequently, total AGPE may be overestimated as topographically trapped dense water masses are permitted to redistribute into the deep global ocean. This implications of this issue are discussed further in Section 2.3.2.

Reference state GPE is defined analogously to physical state GPE with the actual vertical displacement, z, replaced by the vertical position in the reference state, z_{ref}, and in situ density, $\rho = \rho(\theta, S, p(z))$, replaced by density in the reference state, $\rho_{\mathrm{ref}} = \rho(\theta, S, p(z_{\mathrm{ref}}))$. The evolution of $\mathrm{GPE}_{\mathrm{ref}}$ is given by

$$\frac{\partial \mathrm{GPE}_{\mathrm{ref}}}{\partial \mathrm{t}} = \int g \left(\frac{\partial \rho_{\mathrm{ref}}}{\partial t} z_{\mathrm{ref}} + \rho_{\mathrm{ref}} \frac{\partial z_{\mathrm{ref}}}{\partial t} \right) \mathrm{d}V. \tag{2.4}$$

It has been demonstrated that the second term of Equation 2.4 integrates identically to zero (Winters et al., 1995; Tailleux, 2009). Therefore, we define the local contribution to global $\mathrm{GPE}_{\mathrm{ref}}$ of density changes in a single model grid cell to be:

$$\frac{\partial \mathrm{GPE}_{\mathrm{ref}(i,j,k)}}{\partial \mathrm{t}} = g \frac{\partial \rho_{\mathrm{ref}(i,j,k)}}{\partial t} V_{(i,j,k)} z_{\mathrm{ref}(i,j,k)}, \tag{2.5}$$

in which

$$\frac{1}{\rho_0}\frac{\partial \rho_{\mathrm{ref}}}{\partial t} := -\alpha_{\mathrm{ref}} \frac{\partial \theta}{\partial t} + \beta_{\mathrm{ref}} \frac{\partial S}{\partial t}; \quad \alpha_{\mathrm{ref}} := -\frac{1}{\rho_0}\frac{\partial \rho}{\partial \theta}\bigg|_{p=p(z_{\mathrm{ref}})}, \quad \beta_{\mathrm{ref}} := \frac{1}{\rho_0}\frac{\partial \rho}{\partial S}\bigg|_{p=p(z_{\mathrm{ref}})} \tag{2.6}$$

Variations in $\mathrm{GPE}_{\mathrm{ref}}$ due to changes in reference state pressure are neglected from Equation 2.6, because calculation of this term is intractable for the individual

processes described below. We note, however, that the contribution of this term to net $\partial \mathrm{GPE}_{\mathrm{ref}}/\partial \mathrm{t}$ (in offline calculations, not shown) is small.

This study makes use of 140 years of monthly averaged model output in the calculations described above. α, β, α_{ref}, β_{ref}, and z_{ref} are calculated offline using monthly averages of θ and S. Potential temperature and salinity tendencies due to each model process are diagnosed online and we adopt the following decomposition of the respective budgets:

1. Buoyancy forcing (BUOY): penetrative solar radiation, fluxes of temperature and salinity due to exchange with the atmosphere and sea ice.

2. Convection (CON): the convective readjustment to remove static instabilities in the water column. This term includes mixed layer deepening driven by KE released during convection and a small contribution from mixed layer mixing due to wind-driven turbulence according to the Kraus-Turner energetics parameterisation (Gordon et al., 2000).

3. Advection (ADV): the intercell transport of temperature and salinity due to the resolved circulation.

4. Diapycnal mixing (DIA): the diffusive scheme representing the combined effect of turbulent advection and irreversible mixing by applying diffusivity coefficients far greater than molecular values. This is calculated according to the depth-dependent background coefficients of vertical diffusion (varying from 1.03 x 10^{-5} m^2 s^{-1} between surface layers to 14.68 x 10^{-5} m^2 s^{-1} in the abyssal ocean (Gordon et al., 2000)) and monthly averaged θ, S fields.

5. Isopycnal diffusion (ISO): the parameterisation of along-isopycnal eddy fluxes using a constant diffusion coefficient of 1000 m^2 s^{-1} (Gordon et al., 2000).

6. Gent and McWilliams (GM): the parameterisation of bolus fluxes due to mesoscale eddies. This represents unresolved advection in the model and is carried out by the Visbeck et al. (1997) implementation of the Gent and

McWilliams (1990) parameterisation. The thickness diffusion coefficient varies spatially and temporally (between an imposed minimum of 350 $m^2\ s^{-1}$ and a maximum of 2000 $m^2\ s^{-1}$) so as to enhance mixing in regions of baroclinic instability (Gordon et al., 2000).

This decomposition can be expressed mathematically as follows (where τ represents either potential temperature, θ, or salinity, S):

$$\frac{\partial \tau}{\partial t} = -\underbrace{\nabla \cdot (\mathbf{u}\tau)}_{\text{ADV}} - \overbrace{\nabla \cdot (\mathbf{u}^*\tau)}^{GM} + \underbrace{\nabla \cdot (\kappa_h \mathbf{K}_{\text{Redi}} \nabla \tau)}_{ISO} + \overbrace{\frac{\partial}{\partial z}\left(\kappa_v \frac{\partial \tau}{\partial z}\right)}^{\text{DIA}} + \underbrace{\mathrm{F}_\tau}_{BUOY} + \overbrace{\mathrm{q}_{\text{con}}}^{CON},$$

in which $\mathbf{u}$ = velocity, $\mathbf{u}^*$ = bolus velocity, κ_h = isopycnal diffusion coefficient, $\mathbf{K}_{\text{Redi}}$ = Redi isopycnal diffusion operator, κ_v = background vertical diffusion coefficient, F_τ = surface buoyancy fluxes (including fluxes of penetrative radiation to subsurface model layers), and q_{con} = fluxes due to parameterised convection (which cannot be given by an analytic expression).

2.3 Results

2.3.1 The global energy balance

The globally integrated GPE, reference state GPE, and AGPE budgets are presented in Table 2.1. There is a large drift (that is, a nonzero budget sum) in GPE, but not AGPE (this is discussed further in Section 2.4). Within our global decomposition, advection is a primary source of GPE (+0.57 TW) and of AGPE (+0.59 TW). Physically, this implies a net conversion of KE into (A)GPE, similarly as was found by Toggweiler and Samuels (1998) and Gnanadesikan et al. (2005). This indicates that, globally, work done by Ekman transport and wind-driven upwelling

against the horizontal pressure gradient (raising dense fluid parcels and pushing down light fluid parcels) dominates over flows driven by horizontal pressure gradients, as discussed by Gregory and Tailleux (2011).

The largest sink of GPE (-0.82 TW) and AGPE (-0.74 TW) is through the parameterised bolus fluxes due to eddies. These act to flatten isopycnals (surfaces of equal density). This implies a downwelling of dense water and an upwelling of light water and acts as a sink of (A)GPE. Our result is larger in magnitude than the work of the bolus velocity estimated by Aiki and Richards (2008) from an eddy-resolving ocean model (-0.46 TW). However, the ratio of GPE generation by the resolved circulation (cf. the mean isopycnal velocity in Aiki and Richards (2008)) to GPE dissipation by the bolus velocity is consistent between both studies. This is suggestive of an enhanced energy cycle in HadCM3, as opposed to poor parameterisation of mesoscale eddies.

Diapycnal mixing is a leading order GPE source (+0.33 TW). By mixing warmer surface waters down and colder deep waters up, the GPE of the ocean is increased. This is a diabatic process and has a comparable, but not identical, effect on the GPE of the reference state as it does on the GPE of the actual state. Since the reference state is stably stratified, mixing raises its centre of mass and increases $\mathrm{GPE}_{\mathrm{ref}}$ (+0.44 TW). Conversely, diapycnal mixing is a (small) sink of AGPE (-0.12 TW).

It has been suggested previously that surface buoyancy fluxes can play an active energetic role in sustaining global ocean circulation by generating AGPE (Tailleux, 2009). This notion is supported by our analysis, in which surface buoyancy forcing is the largest source of AGPE (+0.72 TW). Previous studies (e.g., Huang and Jin (2006)) have indicated that surface buoyancy forcing is not a significant source of GPE, even taking nonlinearities in the equation of state into account. However, in HadCM3, surface buoyancy fluxes are a GPE source of +0.26 TW, comparable in magnitude to the effects of diapycnal diffusion. This is principally due to solar radiation penetrating to subsurface model layers, an effect neglected in Hughes et al. (2009).

Table 2.1: The globally integrated GPE, GPE_{ref} and AGPE tendencies of the HadCM3 control climate (calculated using monthly averaged data) and the FAMOUS control climates (calculated using annually averaged data) obtained using both a linear and nonlinear equation of state (units: 1 TW = 10^{12} W; positive values indicate energy sources, negative values indicate energy sinks; values preceded by ± indicate the standard deviation of the decadal mean tendencies).

Term	BUOY	CON[a]	ADV	DIA	ISO	GM	CORR[b]	Sum
a) HadCM3								
GPE	+0.26 ± 0.00	-0.39 ± 0.01	+0.57 ± 0.02	+0.33 ± 0.00	-0.07 ± 0.00	-0.82 ± 0.01	-	-0.13 ± 0.02
GPE_{ref}	-0.46 ± 0.02	+0.04 ± 0.01	-0.02 ± 0.02	+0.44 ± 0.01	-0.11 ± 0.02	-0.08 ± 0.01	-	-0.18 ± 0.02
AGPE	+0.72 ± 0.02	-0.44 ± 0.01	+0.59 ± 0.02	-0.12 ± 0.01	+0.04 ± 0.02	-0.74 ± 0.01	-	+0.05 ± 0.02
b) Linear FAMOUS								
GPE	-0.15 ± 0.00		+0.09 ± 0.01	+0.26 ± 0.00	+0.00 ± 0.00	-0.63 ± 0.00	+0.43 ± 0.01	-0.01 ± 0.01
GPE_{ref}	-0.87 ± 0.02		-0.00 ± 0.01	+0.47 ± 0.01	+0.00 ± 0.00	-0.07 ± 0.00	+0.43 ± 0.01	-0.05 ± 0.02
AGPE	+0.72 ± 0.02		+0.09 ± 0.01	-0.21 ± 0.01	+0.00 ± 0.00	-0.56 ± 0.01	-0.00 ± 0.00	+0.04 ± 0.02
c) Nonlinear FAMOUS								
GPE	-0.06 ± 0.01		+0.17 ± 0.01	+0.18 ± 0.00	-0.07 ± 0.00	-0.50 ± 0.01	+0.33 ± 0.01	+0.05 ± 0.01
GPE_{ref}	-0.58 ± 0.03		+0.13 ± 0.01	+0.30 ± 0.00	-0.04 ± 0.00	-0.12 ± 0.00	+0.33 ± 0.01	+0.02 ± 0.03
AGPE	+0.52 ± 0.03		+0.04 ± 0.01	-0.12 ± 0.00	-0.03 ± 0.00	-0.38 ± 0.00	-0.00 ± 0.00	+0.03 ± 0.03

[a]Convective events in the ocean are brief and the corresponding vertical instabilities in the stratification are not reflected in the annually averaged θ, S fields upon which our FAMOUS GPE reference states are based. Therefore, one cannot distinguish between the surface buoyancy forcing that generates static instabilities and the convective readjustment that follows in the FAMOUS (A)GPE budgets.

[b]FAMOUS includes a salinity drift correction term, CORR, applied uniformly in 3D (Smith et al., 2008). Surface freshwater fluxes are converted to surface salinity fluxes using local salinity values. As a result, global conservation of salinity is not guaranteed. HadCM3 requires no such correction as a global reference salinity is used for freshwater conversions.

In contrast, convective readjustment is a GPE (-0.39 TW) and AGPE (-0.44 TW) sink; downwelling density and lowering the centre of mass of the ocean. Convection typically occurs in direct response to buoyancy forcing and the combined effect of the two processes is to produce AGPE (+0.28 TW), but to consume GPE (-0.13 TW).

Finally, isopycnal diffusion is a small sink of GPE and source of AGPE. If the equation of state were linear, isopycnal diffusion would not change GPE since it is only mixing water masses of equal density. With a nonlinear equation of state, however, cabbelling and thermobaricity can destroy or create buoyancy, leading to these small globally integrated effects.

2.3.2 Local contributions to the global energy balance

Figure 2.5 presents the zonally and vertically integrated (A)GPE tendencies as a function of latitude. The budgets are in approximate local balance. If the density of a water column is increased, the GPE of the water column is decreased (and vice versa). The deeper a density change takes place, the greater the energetic effect. This can be understood in the physical ocean in terms of the expansion/contraction of a fluid parcel. If this occurs at depth, a greater mass of overlying water is displaced than if it occurred nearer the surface. In addition to local generation and dissipation, GPE can also be fluxed between water columns (in the same way that density can be). AGPE, on the other hand, is more complicated to interpret by latitude. Processes that increase the density of water lying above its reference level in the physical ocean increase AGPE, whilst processes that decrease the density of such water decrease AGPE. The reverse is true of water below its reference level. The AGPE budget is dominated by regions of large $|z - z_{\mathrm{ref}}|$ since spatial variations in density tendency are comparatively small. The reference state displacement of the surface layer is shown in Figure 2.4. The most significant local contributions are in the Southern Ocean, the high latitude North Atlantic, the Arctic, and the Mediterranean Sea; areas in which dense water is significantly higher in the physical ocean than in the reference state. Large areas of low latitude

ocean are almost negligible in terms of AGPE generation and dissipation, despite being evident in the GPE budget. This is reflected in Figure 2.5.

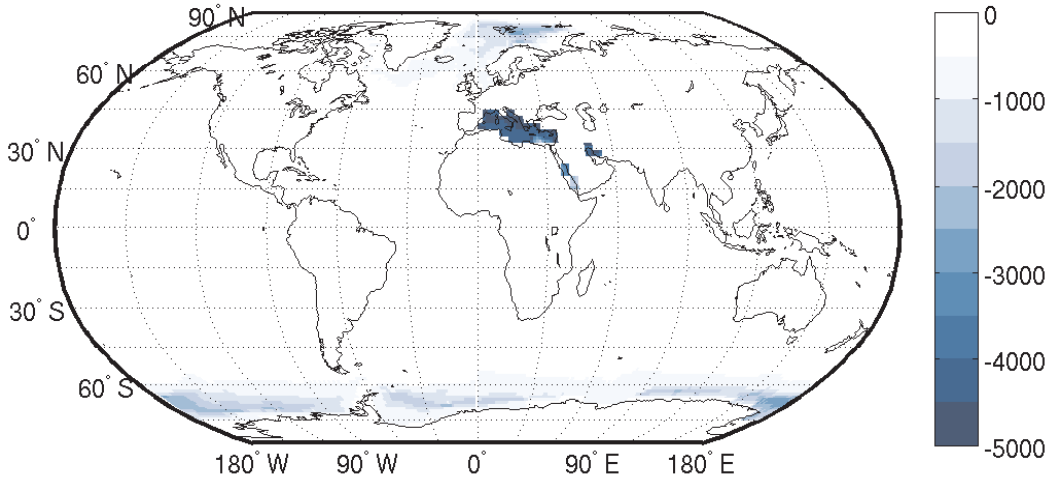

Figure 2.4: The reference state displacement, z_{ref}, of the surface layer in the HadCM3 control simulation, calculated from monthly model output and then averaged over 140 years (units: m).

The dominant role of the Southern Ocean in the global energy budget is immediately apparent from Figure 2.5 (as observed in the HadCM3 KE budget (Gregory and Tailleux, 2011) and the GPE budget of an idealised ocean model (Urakawa and Hasumi, 2009)). The primary balance in this region is adiabatic, between the generation of (A)GPE through advection and the removal of (A)GPE through parameterised eddy fluxes. Across most of this region, wind-driven upwelling deflects isopycnals and raises dense water towards the surface, creating GPE. Mesoscale eddies oppose this, acting to flatten isopycnals. Isopycnal slopes across the ACC are steep and, consequently, the energy dissipation by eddies is large.

Neglecting numerical leakage and the variable compressibility of seawater, the GPE tendency due to advection is well-approximated by:

$$\left.\frac{\partial \mathrm{GPE}}{\partial \mathrm{t}}\right|_{\mathrm{ADV}} \approx \int -\nabla \cdot (\rho g z \mathbf{u}) + \rho \mathrm{g} w \, \mathrm{dV} \tag{2.7}$$

in which ρ = density, g = the gravitational constant, $\mathbf{u}$ = velocity, and w = the vertical component of velocity. Therefore, this term includes both divergence of

GPE transport and local generation and dissipation. The divergence term vanishes in the global integral, but not when integrated regionally. Consequently, the local change in GPE due to the resolved circulation can appear counterintuitive. For example, advection decreases GPE at low-latitudes and increases GPE at high northern latitudes, whereas one might expect to see a positive peak in GPE generation through advection at low-latitudes as equatorial upwelling draws denser water to the surface. This discrepancy is due to divergence in GPE transport as GPE generated at low-latitudes, in part by diabatic processes, is advected to high northern latitudes.

Similarly, GPE that is generated through wind-driven upwelling at the southern boundary of the Antarctic Circumpolar Current (ACC) is transported northwards, with the resulting divergence producing a small local decrease in GPE due to advection. Conversely, convergence of GPE at the northern boundary of the ACC contributes to the local increase in GPE due to advection. The net effect of advection across the ACC is to generate (A)GPE. The ACC is approximately centred at $45°S$ west of Kerguelen and $55°S$ east of Kerguelen, producing the two peaks visible in Figure 2.5a.

GPE gain through diapycnal diffusion is greatest in low-latitude equatorial regions where vertical stratification is strongest (implying larger diffusive fluxes). In this region, buoyancy forcing is also a significant source of GPE due to the intensity of penetrative solar radiation. However, isopycnals in the low-latitude ocean are relatively horizontal and the Gent and McWilliams parameterisation plays little role.

At mid- to high-latitudes, convection is a sink of (A)GPE due to readjustments occurring in the mixed layer (triggered by surface cooling), with contributions at $60°N$ and $60°S$ due to the effects of convection extending deeper into the ocean. At high-latitudes, buoyancy forcing is a substantial source of AGPE in both hemispheres through the surface cooling of already dense water.

Figure 2.6 presents the zonally and vertically integrated (A)GPE tendencies as a function of latitude in the Atlantic only. The Mediterranean is excluded from the

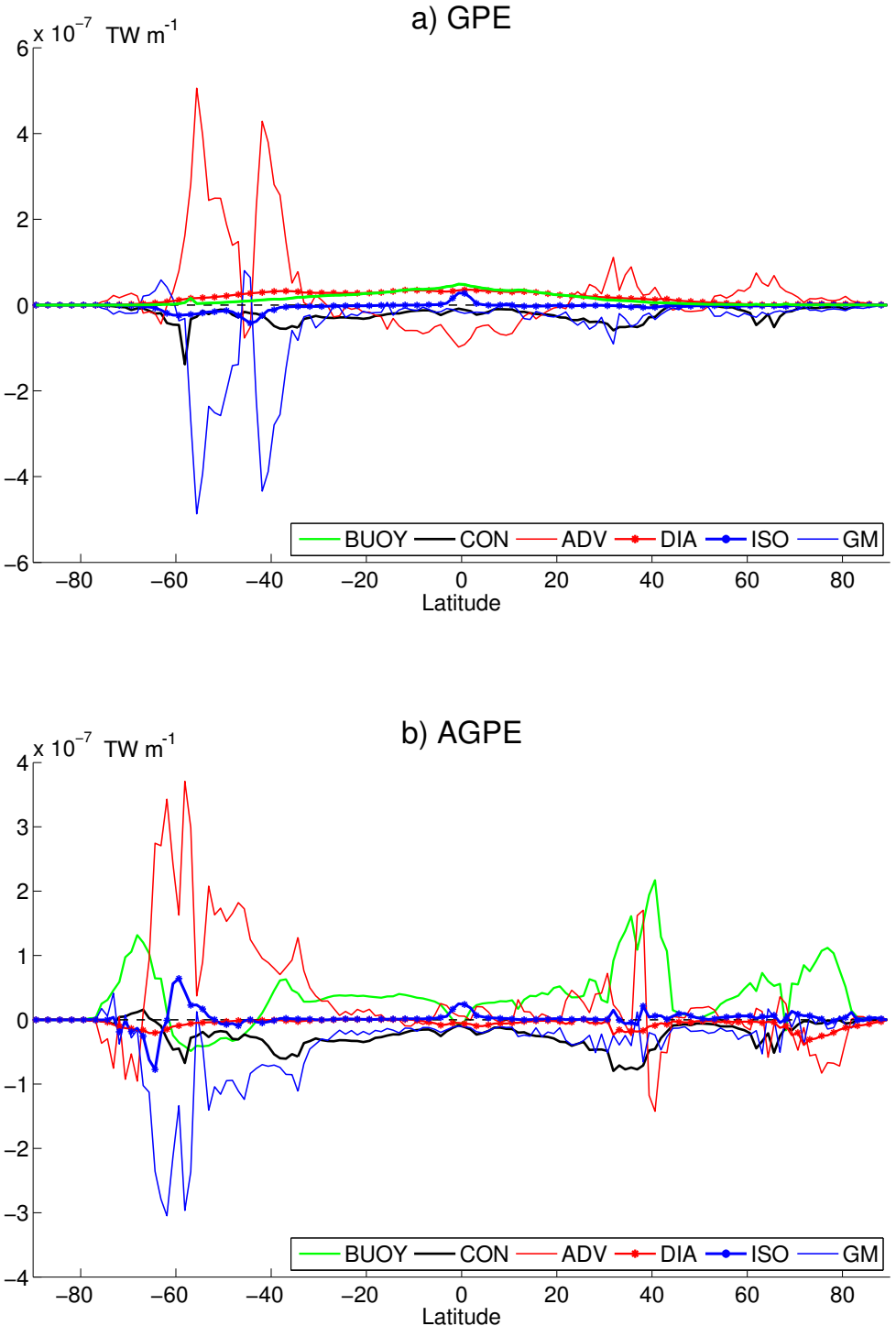

Figure 2.5: The zonally and vertically integrated a) GPE and b) AGPE tendencies due to surface buoyancy forcing (BUOY), convection (CON), advection (ADV), diapycnal diffusion (DIA), isopycnal mixing (ISO), and Gent and McWilliams mixing (GM) in the HadCM3 control climate, plotted as a function of latitude. Note that each graph has a different scale on the vertical axis. Positive values indicate local increases in energy and negative values indicate local decreases. Units: 1 TW $m^{-1} = 10^{12}$ W m^{-1}.

Atlantic (A)GPE tendencies shown here, but it is included in the global reference state from which they are calculated. As in the global case, it can be seen that the (A)GPE budgets are in approximate local balance. However, the GPE and AGPE balance is markedly different in the Atlantic. GPE is adiabatically gained through advection in both the western boundary current and at high latitudes and, in both locations, is lost locally through the effects of convection and mesoscale eddies. Surface buoyancy fluxes are a low order source of GPE throughout the Atlantic. Conversely, significant AGPE is diabatically gained in the western boundary current and at high-latitudes through surface buoyancy forcing. This is dissipated by the effects of convection and, at high-latitudes, the resolved circulation.

The spike in activity in the global AGPE budget at $40°N$ (Figure 2.5) is, in part, due to the significant displacement of the Mediterranean Sea in the reference state (because of its high density in comparison to the global ocean), enhancing AGPE generation by surface buoyancy fluxes and AGPE dissipation by advection. It features much more prominently in the reference state in HadCM3 than in the ORCA2 ocean-only configuration of the NEMO ocean modelling framework (Chapter 4, Figure 4.1). However, HadCM3 has previously been shown to simulate a Mediterranean that is too dense, being both colder and saltier than observations suggest in a simulation of late 20^{th}-century climate (Marcos and Tsimplis, 2008). The connection between the Mediterranean and the global ocean is restricted by a shallow sill. It has been suggested that the adiabatic redistribution of topographically restricted waters to the deep ocean is unrealistic and that the reference state calculated may not be physically attainable by the ocean (Huang, 2005). A recent study by Stewart et al. (2014) examined the impact of topographical trapping of dense water on the calculation of both the total AGPE reservoir and the AGPE generation by surface forcing using simplified ocean model configurations to compare a number of proposed methods for calculating the GPE reference state. In this instance, whilst a single basin adiabatic resort (such as that used here) overestimates total AGPE, it suffices for estimating AGPE generation. In fact, provided the reference state is obtained via adiabatic sorting methods, the estimation of AGPE power input by surface buoyancy fluxes is relatively insensitive to the treatment of

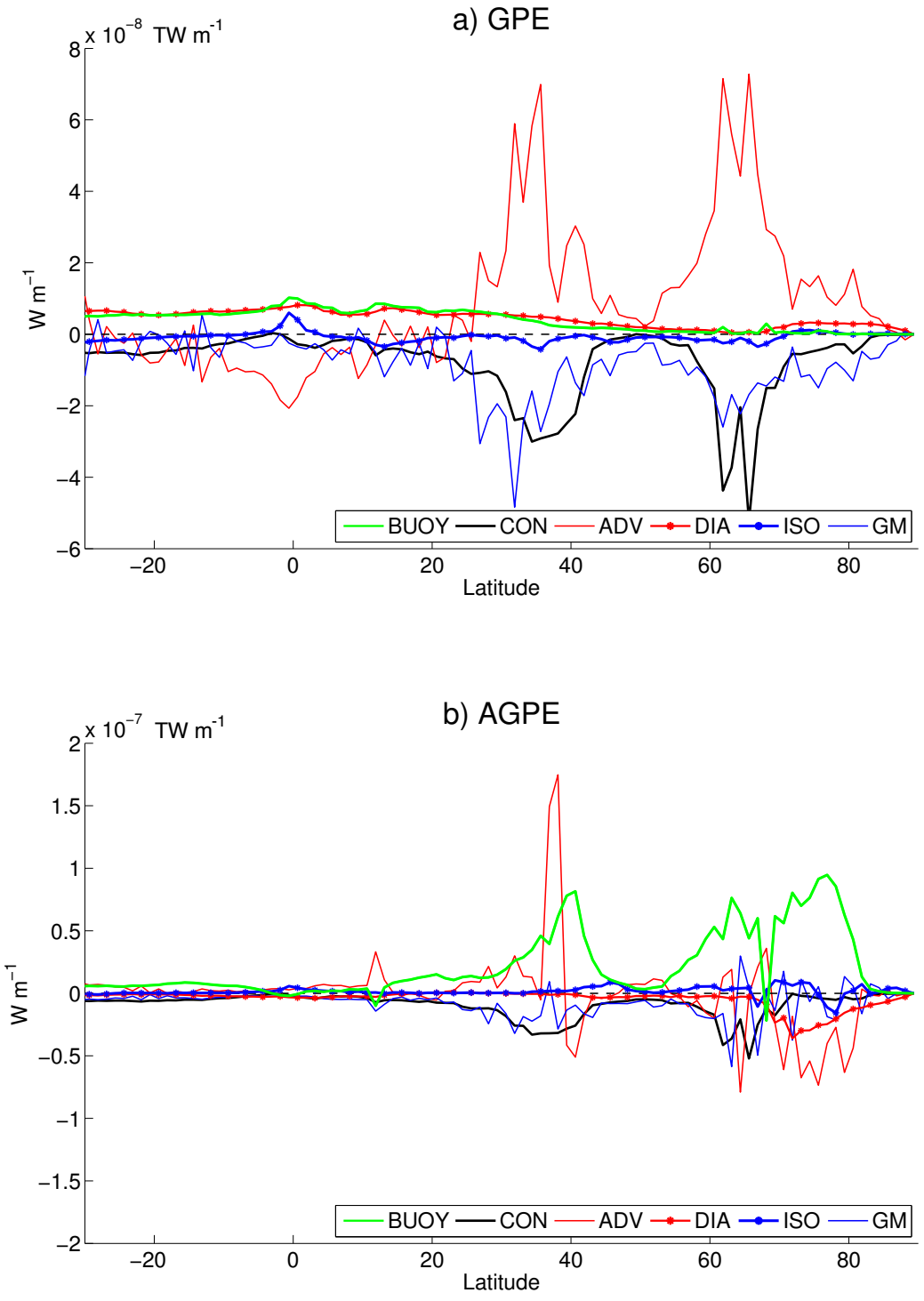

Figure 2.6: The zonally and vertically integrated a) GPE and b) AGPE tendencies due to surface buoyancy forcing (BUOY), convection (CON), advection (ADV), diapycnal diffusion (DIA), isopycnal mixing (ISO), and Gent and McWilliams mixing (GM) integrated over the Atlantic basin only (excluding the Mediterranean), plotted as a function of latitude. Note that each graph has a different scale on the vertical axis. Positive values indicate local increases in energy and negative values indicate local decreases. Note: the Atlantic integrals are calculated using data from a only single decade of the control simulation. Units: 1 TW m^{-1} = 10^{12} W m^{-1}.

topographic barriers. Stewart et al. (2014) advocate calculating the GPE reference state using an adiabatic resort method of "multi-basin relaxation" in which only dense water lying above sill depth is allowed to exchange with the global ocean basin, arguing that these waters can adiabatically redistribute to the deep ocean without any energetic expense. In HadCM3, we find that the dominant controls on the AGPE budget in the Mediterranean (advection and surface buoyancy forcing) are predominantly acting on waters lying above sill depth. Therefore, we consider the inclusion of the Mediterranean not to be problematic. As a sensitivity study, the Mediterranean Sea was removed entirely from the reference state calculation and the key conclusions of this chapter were unaltered (not shown). It should be noted that, in practice, exchanges between the Mediterranean Sea and the Atlantic Ocean are parameterised in HadCM3 (Gordon et al., 2000).

2.4 Discussion and conclusions

In this chapter, we have presented the GPE and AGPE budgets of the ocean component of the coupled climate model HadCM3. This is, to our knowledge, the first time that the (A)GPE budgets of the ocean have been calculated simultaneously using output from a global coupled climate model. Whilst available potential energy is the accepted energetic paradigm in the atmosphere, the mechanical energetics of global ocean circulation are still often discussed in the context of the more traditional GPE framework (e.g. Wunsch and Ferrari (2004); Huang and Jin (2006); Johnson et al. (2007); Kuhlbrodt et al. (2007)). The application of available potential energetics to oceanography has, thus far, been limited due to its interpretational difficulties and the complications arising from the nonlinear equation of state for seawater. However, we have shown in this study that there are clear differences in the energetic role of physical processes in the ocean depending on whether they are viewed from the perspective of the GPE or AGPE frameworks.

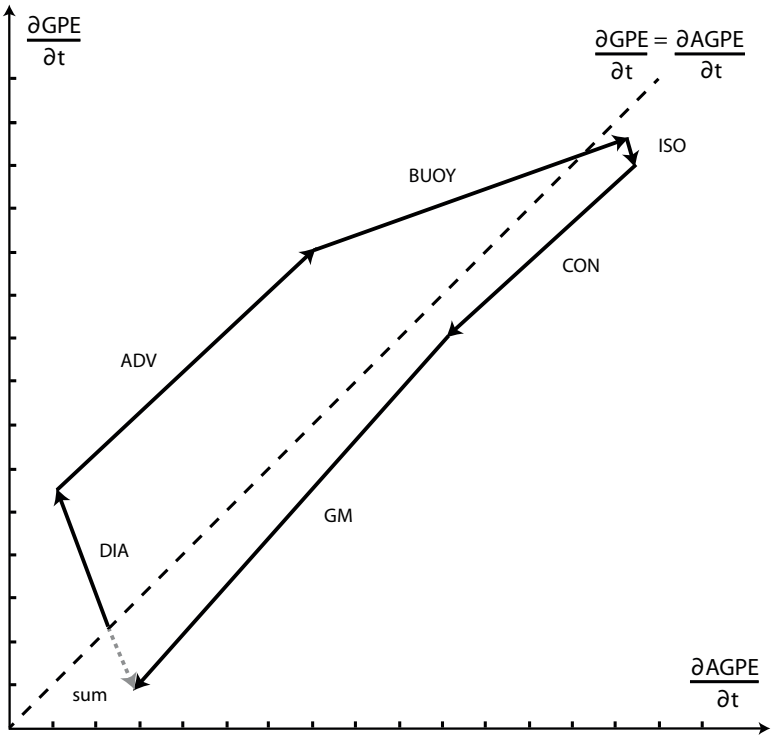

Figure 2.7: HadCM3 (A)GPE tendencies (as quoted in Table 2.1) depicted together on a plot of ∂GPE/∂t against ∂AGPE/∂t. Positive vector components imply an increase in energy. The dashed line indicates ∂GPE/∂t = ∂AGPE/∂t. Ticks are at 0.1 TW intervals.

Figure 2.7 illustrates this by depicting the GPE and AGPE tendencies of each term on a plot of ∂GPE/∂t against ∂AGPE/∂t. This diagnostic tool allows us to analyse the relative effects of each physical process on GPE and AGPE simultaneously. Advection (resolved: ADV, unresolved: GM) dominates the global energy budget in Figure 2.7: the large-scale, resolved circulation is the primary global source of (A)GPE, whilst the small-scale, unresolved eddy fluxes are the largest global sink of (A)GPE. Since adiabatic processes have no effect on the GPE of the reference state (as described in Section 2.1), they run parallel to the line given by ∂GPE/∂t = ∂AGPE/∂t when plotted as a vector on this diagram. Thus, adiabatic processes can generate/remove (A)GPE in a single step.

Conversely, (A)GPE tendencies due to diabatic processes have components perpendicular to the dashed line in Figure 2.7 and produce the distinctive trapezoidal shape of the schematic. Whilst adiabatic processes have the same effect on both potential energy reservoirs, diabatic processes have differing effects on (A)GPE

by mixing the reference state. Both a process to generate GPE and a process to make this available are required to diabatically sustain large-scale ocean circulation. In the decomposition presented here, vertical mixing is a substantial source of background GPE, but a small sink of AGPE. Conversely, surface buoyancy forcing is substantial source of AGPE, reducing the GPE of the reference state. Consequently, these diabatic processes are effectively playing complementary roles in the diabatic generation of AGPE.

Though convection is carried out through an intrinsically diabatic parameterisation (mixing fluid layers down through the water column until stable stratification is achieved), it has the distinct appearance of an adiabatic process in our (A)GPE energetics framework. This is because the convective scheme mixes fluid parcels of very similar density and, consequently, at very similar depths in the reference state. In effect, convective columns in the physical ocean are vertically condensed in the reference state and, thus, have little impact on global $\mathrm{GPE}_{\mathrm{ref}}$.

Taken together, advective processes (ADV+GM) represent the global sink of (A)GPE that balances the diabatic energy source. The distinction between resolved and unresolved advection is merely an artificial scale separation due to the limitations of the model. Our results suggest that if mesoscale advection were resolved (e.g. in an eddy resolving model, trivially in the physical ocean), advection would constitute a net (A)GPE sink, thus implying net conversion from AGPE to KE (as opposed to the net conversion from KE to AGPE determined by Gregory and Tailleux (2011)). However, such a lack of scale distinction would mask the significant (A)GPE generation by the large-scale circulation. Indeed, a recent study by Saenz et al. (2012) using an idealised eddy-permitting ocean model with a linear equation of state supports this assertion, finding that in almost all their experimental configurations net energy conversion is from AGPE to KE. Whilst it is evident that unresolved mesoscale processes play an important role in closing HadCM3's (A)GPE budget, the energy released is assumed to be dissipated and is not incorporated into HadCM3's KE budget (only the resolved circulation is, Gregory and Tailleux (2011)).

Figure 2.7 shows that both resolved and unresolved advection have small diabatic components in HadCM3. These could be caused either by the effects of nolinearities in equation of state on numerical mixing (resulting in cabbelling or thermobaricity) or by numerical diapycnal mixing (diapycnal leakage). Cabbeling leads to water mass densification and is a sink of GPE. Conversely, diapycnal mixing raises GPE. Thus, the negative sign of $\partial \mathrm{GPE}_{\mathrm{ref}}/\partial \mathrm{t}$ due to ADV and GM (Table 2.1) is consistent with the former hypothesis. However, the tendency is small.

Throughout this chapter, we have described several instances in which nonlinearities in the equation of state are influential in both the construction of the GPE reference state (from which AGPE tendencies are calculated) and in the energetic representation of certain physical processes, such as isopycnal mixing and advection. However, the usage of linear equation of states in numerical models is relatively commonplace, particularly in idealised eddy-resolving configurations. It is, therefore, of interest to know whether our results are robust to the choice of equation of state. In order to determine this, we repeat our analysis using two simulations from FAMOUS (a fast, course resolution version of HadCM3 (Smith et al., 2008)): a control simulation (using a nonlinear equation of state) and an additional steady-state simulation that uses a linear equation of state. The simulated climate of the linear FAMOUS run is not unrealistic (e.g., the strength of Atlantic meridional overturning - Figure 2.8) and is similar to the nonlinear FAMOUS run in many respects. Due to limitations in the available model output, we are only able to calculate (A)GPE budgets using annually averaged data from both FAMOUS simulations. Convective events in the ocean are brief and the corresponding vertical instabilities in the stratification are not reflected in the annually averaged θ, S fields upon which our GPE reference states are based. Therefore, one cannot distinguish between the surface buoyancy forcing that generates static instabilities and the convective readjustment that follows in the $\mathrm{GPE}_{\mathrm{ref}}$ and AGPE budgets of FAMOUS so we consider only the net effect of these two terms: BUOY+CON.

The (A)GPE budgets of both FAMOUS simulations are presented in Table 2.1 and plotted schematically in Figure 2.9. Whilst it is noted that the magnitude

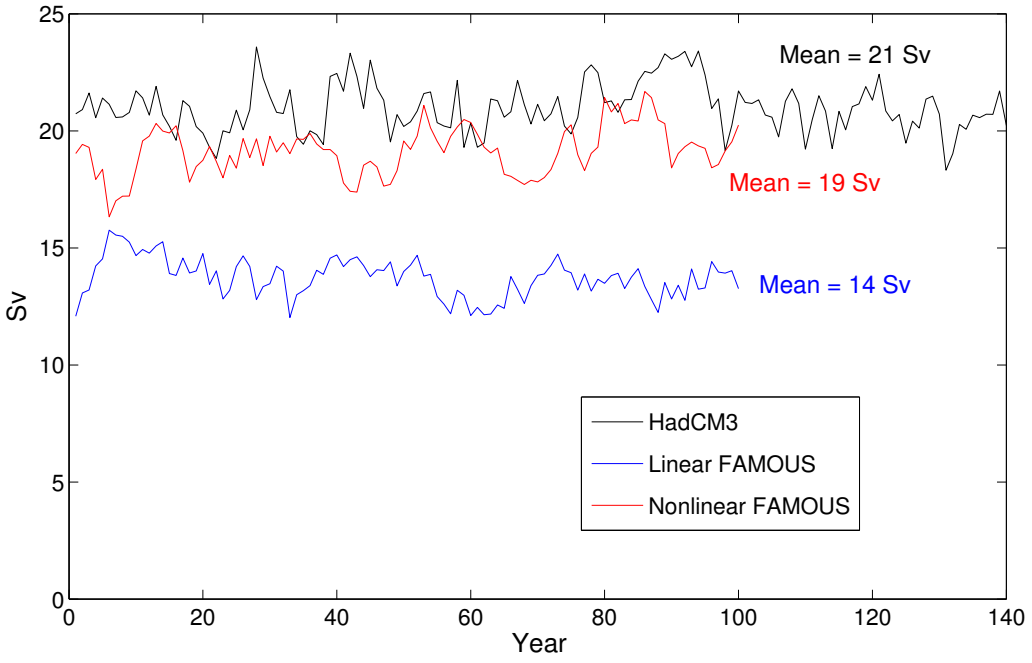

Figure 2.8: The maximum Atlantic meridional overturning streamfunction (below 300m) for the HadCM3 and FAMOUS control simulation and a simulation of FAMOUS using a linear equation of state. Units: 1 Sv = 10^6 m^3 s^{-1}.

of the ADV term is significantly smaller in the FAMOUS (A)GPE budget than in HadCM3, this term varies greatly between models (see the discussion of term B in the KE analysis of Gregory and Tailleux (2011)). It is a function of the resolved velocity field and is, thus, highly dependent on model configuration and resolution. The diabatic component of the ADV and GM terms are zero in the linear FAMOUS simulation and negative in the nonlinear FAMOUS simulation. This supports the conclusion that the energetic effect of numerical diapycnal leakage is not significant in the model and that the perturbations we see are due to nonlinearities in the equation of state. We also note that under a linear equation of state the energetic effect of isopycnal diffusion diminishes to zero as expected. Despite the variation in magnitude between terms, the energy budgets of both of the FAMOUS simulations and the HadCM3 control simulation are schematically very similar (see Figures 2.7 and 2.9) and the sign of the dominant (A)GPE tendencies are consistent, thus supporting the key conclusions of this study.

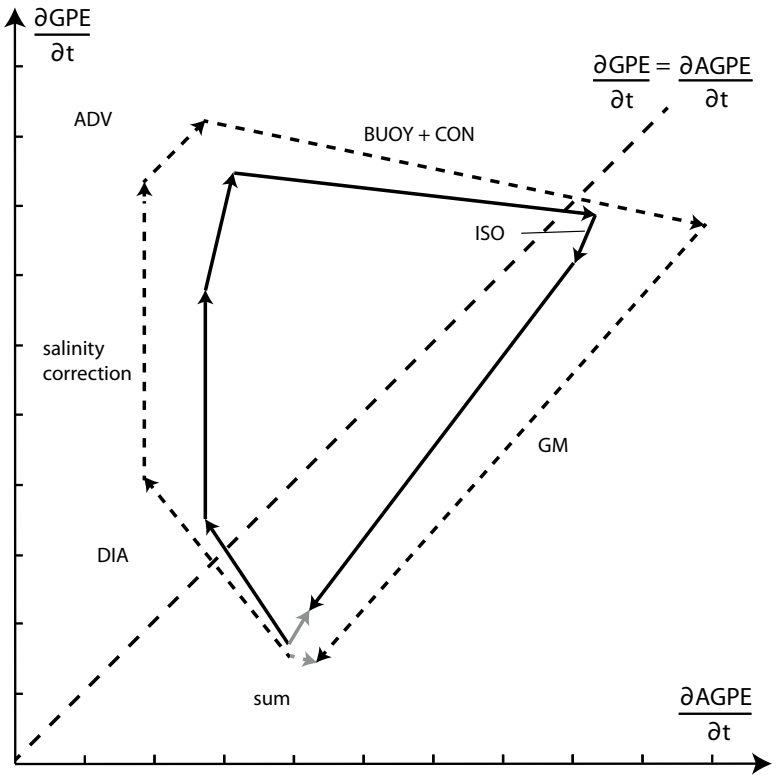

Figure 2.9: FAMOUS (A)GPE tendencies (as quoted in Table 2.1) depicted together on a plot of ∂GPE/∂t against ∂AGPE/∂t. Solid arrows indicate terms in the FAMOUS control simulation and dashed arrows indicate terms in the simulation equipped with a linear equation of state. Positive vector components imply an increase in energy. The dashed line indicates ∂GPE/∂t = ∂AGPE/∂t. Ticks are at 0.1 TW intervals.

As touched upon previously in this chapter, the advective production of (A)GPE by the resolved circulation is often regarded as the conversion between KE and (A)GPE. However, KE loss (the term -B in Gregory and Tailleux (2011)) generally differs from both GPE gain and AGPE gain due to nonlinearities in the equation of state and, in models, numerical mixing. This correspondence is approximately true of HadCM3 (-B = 0.49 TW) and nonlinear FAMOUS (-B = 0.06 TW) and exactly true of the linear simulation of FAMOUS (-B = 0.09 TW). This relationship is discussed in more detail in Chapter 4, where changes in meridional overturning are discussed in the context of changes in the conversion rate between (A)GPE and KE.

Finally, a spatially uniform tracer correction is applied in FAMOUS to remove globally integrated salinity drift (Smith et al., 2008). This has a large effect on

GPE, but a negligible impact on AGPE (see Table 2.1). This is because the equation of state is almost linear with respect to salinity and, as such, a uniform correction has no effect on internal density gradients. Similarly, there is a (uncorrected) GPE drift in HadCM3 due to non-zero surface fluxes (resulting in a 0.03°C century^{-1} decrease in global mean temperature and a 0.001 psu century^{-1} increase in global mean salinity). Such surface exchanges can take a long time to fully equilibrate in a coupled AOGCM and this small continued drift has little effect on internal density gradients. Moreover, the HadCM3 control climate is dynamically stable (as evidence by the small 0.01 Sv century^{-1} trend in maximum Atlantic overturning stream function; standard deviation 1.06 Sv - see Figure 2.8) and this is reflected in the smaller closure error in AGPE; the partition intrinsically linked to the dynamic properties of the circulation. These findings support the notion that global AGPE is a more dynamically relevant quantity than global GPE.

To conclude, we have presented the ocean's global GPE and AGPE budgets in a unified way, using output from a realistic coupled climate model. In doing so, the different roles of adiabatic and diabatic processes in driving ocean circulation have been clearly illustrated. The steady-state analysis presented here will act as the basis from which to interpret the energetics of transient ocean simulations in Chapter 4.

Chapter 3

Predicting global overturning from meridional density gradients

The work presented in this chapter has been submitted to a peer-reviewed journal:

Butler, E. D., K. I. Oliver, J. J.-M. Hirschi, and J. V. Mecking (2014), Predicting global overturning from meridional density gradients, Clim. Dyn. (in submission)

3.1 Introduction

The Meridional Overturning Circulation (MOC) is a large-scale global circulation of water throughout the World's ocean. The strength of global overturning has a significant effect on climate through meridional heat transport and the ventilation of the deep ocean. However, the ocean is a highly complex system and the driving processes of, and energetic constraints on, global ocean circulation are still extensively discussed in the literature (see Chapter 2 and e.g. Kuhlbrodt et al. (2007); Wunsch and Ferrari (2004)). Nevertheless, numerous attempts have been made to scale the strength of overturning, principally in the North Atlantic, with large-scale physical properties such as vertical diffusivity (Park and Bryan, 2000) and kinetic energy/potential energy conversion in the North Atlantic (Gregory and

Tailleux, 2011). Such scalings can be used to inform parameterisations in theoretical box modelling studies and infer how ocean circulation might, qualitatively, respond to changes in climatic forcing. In particular, many previous studies have sought to relate the strength of meridional overturning in the North Atlantic to the meridional density gradient (e.g. Thorpe et al. (2001); de Boer et al. (2010); Sijp et al. (2012)). The idea of a linear relationship between overturning and meridional density gradients dates back to early conceptual models of 'thermohaline' circulation. Whilst the MOC has been shown to be highly sensitive to high-latitude surface buoyancy forcing in the North Atlantic in numerous modelling studies (e.g.: Stouffer et al. 2006), certain model results suggest that this relationship is far from linear with some idealised studies finding that meridional overturning can even decrease with increasing meridional density gradient in some circumstances (e.g. de Boer et al. (2010)).

However, density gradients do not directly drive flow. Instead, vertically integrated horizontal density gradients translate into horizontal pressure gradients (via the hydrostatic relationship) that, in turn, are able to transfer momentum. Moreover, geostrophic meridional flow is set by zonal pressure gradients, not meridional pressure gradients, due to the influence of the Coriolis force. Therefore, a direct link between meridional overturning and meridional density gradients is far from clear. If we take the large-scale thermal wind equations applied to a rectangular basin (obtained from the hydrostatic equation and the vertical derivative of the geostrophic equation) and we assume that meridional and zonal pressure gradients can be related by a dimensionless constant of proportionality, c_ρ, then we obtain the following expression:

$$\frac{\partial V}{\partial z} = \frac{c_\rho g}{f \rho_0 L_y} \Delta\rho_y(z) \tag{3.1}$$

in which V = basin-scale meridional velocity, $\Delta\rho_y$ = meridional density difference (as a function of vertical displacement, z), L_y = the meridional length scale, g = the gravitational constant, and ρ_0 and f_0 are representative values for density and the Coriolis parameter, respectively. This is effectively a 'rotated', scaled

form of the conventional thermal wind equation. Of course, the validity of this equation relies on the validity of the assumption that a linear relationship exists between zonal and meridional pressure gradients at basin-wide scales. This has been shown to hold at equilibrium in a general circulation modelling study with idealised bathymetry (Park and Bryan, 2000) and has been rationalised theoretically by Wright et al. (1995) and Marotzke (1997), arguing that a meridional pressure gradient across a basin will set up an eastward zonal flow that converges at the eastern boundary, producing a zonal pressure gradient that in turn drives a meridional flow (Kuhlbrodt et al., 2007).

Equation 3.1 is typically scaled directly to yield a meridional velocity scale $V \sim \Delta\rho_y H$ (e.g., for an upper overturning cell of scale depth H) and, therefore, an overturning transport $\Psi \sim VH \sim \Delta\rho_y H^2$ (e.g. de Boer et al. (2010)). The way in which this scaling is implemented and exploited varies significantly across the literature. Considering H to be fixed yields a linear relationship between overturning and density difference (Rahmstorf, 1996). Alternatively, considering the density difference to be constant yields a quadratic relationship between overturning and scale depth (Gnanadesikan, 1999). However, Levermann and Fürst (2010) demonstrated (using a coupled climate model) that both of these quantities vary simultaneously and considering either to be fixed is unphysical. Thus, suitable scales for both $\Delta\rho_y$ and H must be chosen, but the approach to this can appear ad hoc with definitions sometimes chosen empirically because they yield positive results within a particular model and experimental setup, despite a lack of cross model support. de Boer et al. (2010) carried out a methodical evaluation of a wide range of both $\Delta\rho_y$ and H scale candidates in an idealised GCM, finding that traditional measures of $\Delta\rho_y$ (e.g., depth-averaged meridional density gradient) and H (e.g. pycnocline depth) do not predict overturning well. Instead, better correlations are found when using depth scales derived from a measure of the meridional pressure gradient, as would be expected from the central theoretical considerations.

An alternative approach to the direct scaling of Equation 3.1 (and the subsequent loss of information) is to retain the depth dependence in $\Delta\rho_y$ and integrate twice

vertically to obtain an expression for the meridional overturning streamfunction derived from meridional pressure gradients, hereafter referred to as Ψ_p, at depth z:

$$\Psi_p(z) = L_x \int_z^0 V(z')\,\mathrm{d}z' \tag{3.2}$$

in which L_x = the zonal basin length scale (assuming vertical walls) and:

$$V(z) = \frac{c_\rho g}{f_0 \rho_0 L_y} \left(\frac{1}{h} \int_{-h}^{0} \left(\int_{z'}^{0} \Delta\rho_y(s)\,\mathrm{d}s \right) \mathrm{d}z' - \int_z^0 \Delta\rho_y(z')\,\mathrm{d}z' \right) \tag{3.3}$$

where h is the bottom depth and V is the basin-scale meridional velocity determined by local anomalies from the depth averaged pressure gradient (Oliver et al., 2005). The constant of integration is fixed by the constraint of zero net vertically integrated meridional flow. It follows that meridional overturning should scale with the twice-integrated meridional density difference (Hughes and Weaver, 1994) as opposed to once-integrated meridional density difference (Thorpe et al., 2001). Moreover, Equation 3.3 implicitly defines the overturning scale depth sought by previous studies in a manner directly consistent with the scaling derivation: that is, the level of no meridional flow at the boundary between the upper and lower overturning cells given by $V(H) = 0$. In fact, when a $\Psi \sim \Delta\rho_y H^2$ scaling is used with H determined in such a way (alongside a depth-averaged measure meridional density gradient) then good correlation has been seen with model simulated overturning (Equation 8, de Boer et al. (2010)).

Previous scaling studies have typically focussed on steady state simulations, rectilinear bathymetry and/or the Atlantic only. In this study, we investigate the validity and robustness of this scaling approach in a general circulation model (GCM) with realistic topography under a transient forcing experimental setup, testing the overturning inferred from twice-integrated meridional density gradients against model simulated overturning in both the Atlantic and Indo-Pacific basins. We explore a wide range of forcing timescales ranging from sub-decadal to

millennial periods through a series of deterministic, periodically varying surface buoyancy forcing experiments in a coarse resolution GCM, allowing us to isolate the ocean's response at each timescale. We then extend our analysis to a higher resolution, stochastic simulation forced with North Atlantic Oscillation (NAO) structured stochastic variability in all surface buoyancy and surface momentum forcing components.

3.2 Method

3.2.1 Model description

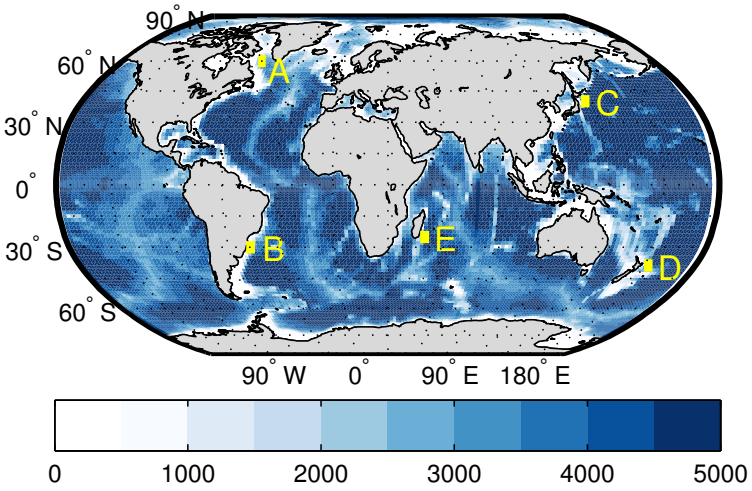

Figure 3.1: Map of ORCA2 model bathymetry with the density locations used in meridional density difference calculations marked in yellow. Units: m.

The periodically forced numerical experiments in this study were conducted using the Nucleus for European Modeling of the Ocean (NEMO) ocean general circulation model (OGCM) in the global ORCA2 configuration (Madec, 2008). This configuration solves the primitive equations on a tri-polar grid (avoiding a singularity in the Arctic Ocean) with a nominal horizontal resolution of 2°, refined to 0.5° in the equatorial region. The vertical grid structure has 31 levels (varying from 10m thick near the surface to approximately 500m thick in the deep ocean) and uses partial bottom cells for better representation of bottom topography (see

Figure 3.1). The model is equipped with a full nonlinear equation of state and the effect of mesoscale eddies is parameterised using the Gent and McWilliams (1990) advective scheme with spatially varying diffusion coefficients. A no-slip lateral momentum boundary condition is applied at the coastline. Vertical mixing is parameterised using a turbulent kinetic energy closure scheme. We use an ocean-only setup in which unperturbed surface boundary conditions are computed from Coordinated Ocean-ice Reference Experiment (CORE) bulk formulae incorporating active ocean variables and prescribed atmospheric data (Large and Yeager, 2004, 2009). The model is initially spun-up from rest and integrated for a 2000 year control period using atmospheric variables given by the CORE v2.0 normal year atmospheric dataset repeated annually (Large and Yeager, 2009). The ocean component is coupled to the LIM2 sea-ice model (Madec, 2008).

3.2.2 The control simulation

After 2000 years of model spin-up, meridional overturning has reached a steady state in both the upper and abyssal North Atlantic (Figure 3.2).

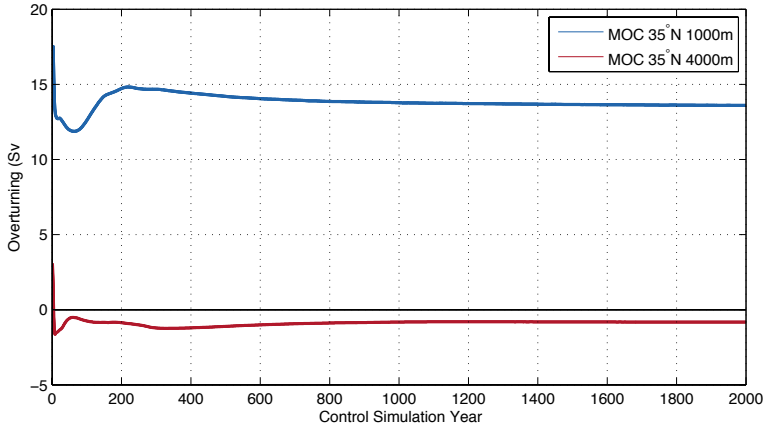

Figure 3.2: Timeseries of the meridional overturning streamfunction evaluated at 1000m and 4000m (35°N) in the North Atlantic, plotted for the 2000 year spin-up period.

The overturning streamfunction for the Atlantic and Indo-Pacific basins at the end of the 2000 year spin-up period is shown in Figure 3.3. In the Atlantic we have an upper overturning cell of strength 15.0 Sv associated with North Atlantic Deep

Water (NADW) in which warm surface waters flow poleward, lose their heat to the atmosphere, sink in regions of deepwater formation and return at depth to regions of upwelling. This overlays a reverse abyssal cell associated with Antarctic Bottom Water (AABW) of strength -3.5 Sv in the North Atlantic. Meridional overturning is qualitatively different in the Pacific with a single dominant overturning cell associated with Antarctic Bottom Water (AABW) of strength -14.2 Sv in the deep ocean. Unlike in the Atlantic, there is no vigorous upper ocean overturning cell. The strength and structure of global ocean circulation is in good agreement with observations in both the upper and deep ocean.

3.2.3 Experimental setup

After the initial 2000 year spin-up period, the model is then forced using periodically varying surface buoyancy forcing of different periods in the North Atlantic. In these transient experiments, a 10m air temperature perturbation is superimposed on the normal year cycle and fed into the bulk formulae. A zonally-constant, sinusoidal perturbation is applied between 0°N and 90°N, peaking in amplitude at 60°N. The prescribed air temperature perturbation is given as a function, F, of latitude, θ, and time, t:

$$F(\theta, t; A, P) := \begin{cases} A \sin\left(\frac{2\pi t}{P}\right) \sin\left(\frac{\theta\pi}{120}\right) & \text{if} \quad 0°\text{N} \leq \theta \leq 60°\text{N} \\ A \sin\left(\frac{2\pi t}{P}\right) \sin\left(\frac{\theta\pi}{60} - \frac{\pi}{2}\right) & \text{if} \quad 60°\text{N} < \theta \leq 90°\text{N} \end{cases} \tag{3.4}$$

in which the sinusoidal amplitude of oscillation, A, is set at 5°C for all experiments and the period of oscillation, P, takes sub-decadal to millennial values: $P =$ 8, 16, 32, 64, 128, 256, 512, 1024 and 2048 years. The shape of the forcing cycle as a function of latitude at different stages in an oscillation is depicted in Figure 3.4. The forcing period is increased sequentially in a style similar to Lucas et al. (2005), such that the 2^{n+1} year forcing cycle is applied directly after the 2^n year forcing cycle has completed (see Figure 3.5). Each forcing period is repeated for 4 cycles or a minimum of 128 years (excluding the 2048 year cycle for which

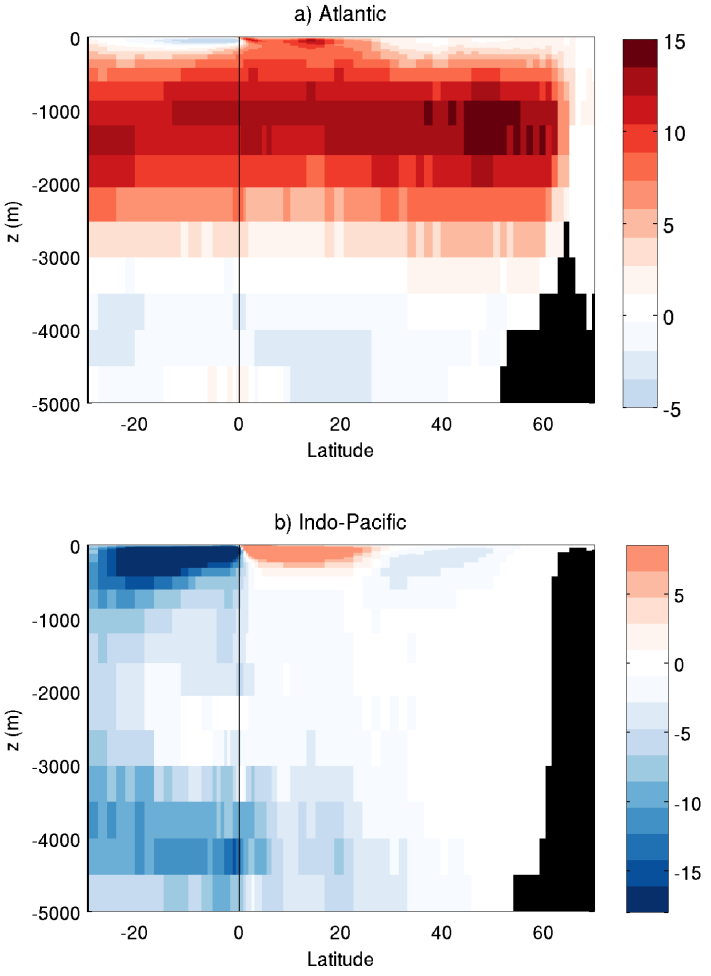

Figure 3.3: The control a) Atlantic and b) Indo-Pacific overturning stream-functions (units: 1 Sv = 10^6 m^3 s^{-1}) plotted as a function of latitude and depth, averaged over the final 50 years of the 2,000 year control simulation in ORCA2. Note: colour scheme is saturated for near-surface wind-driven overturning cells.

just two repetitions are made) to reach a cyclostationary state in oceanic response. Aside from the background CORE seasonal cycle, no additional buoyancy forcing perturbations are applied outside of the North Atlantic.

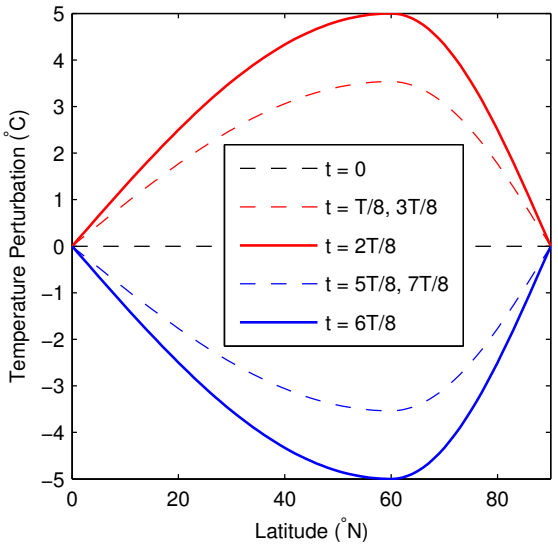

Figure 3.4: Air temperature perturbation applied over the North Atlantic plotted as a function of latitude for an arbitrary forcing period of length T. Units: °C.

3.3 Scaling the AMOC response to deterministic forcing

For conciseness, we hereafter refer to the model simulated overturning streamfunction as Ψ and the overturning streamfunction constructed from twice-integrated meridional density gradients (given by Equations 3.2 and 3.3) as Ψ_p. The density scale is set as $\rho_0 = 10^3$ kg m^{-3}, the gravitational constant is taken to be $g = 10$ m s^{-2}, and we define $f_0 = 10^{-4}$ s^{-1} as a representative value of the mid-latitude Coriolis parameter. The meridional length scale, L_y, is taken to be 10,000 km. The zonal length scale, L_x, varies with latitude and depth. However, for simplicity, we choose a single zonal length scale of $L_x = 5{,}000$ km in the Atlantic. We consider the dimensionless ratio of meridional to zonal velocity, c_ρ, to be a function of location only and, therefore, may be fitted to individual basins, depths, and latitudes, but may not be fitted to individual timescales of variability. In principle, this value should be relatively consistent between locations since large-scale variations in geometry are encapsulated in the zonal and meridional length scales.

We define our meridional density difference, $\Delta\rho_y$, to be that measured along the

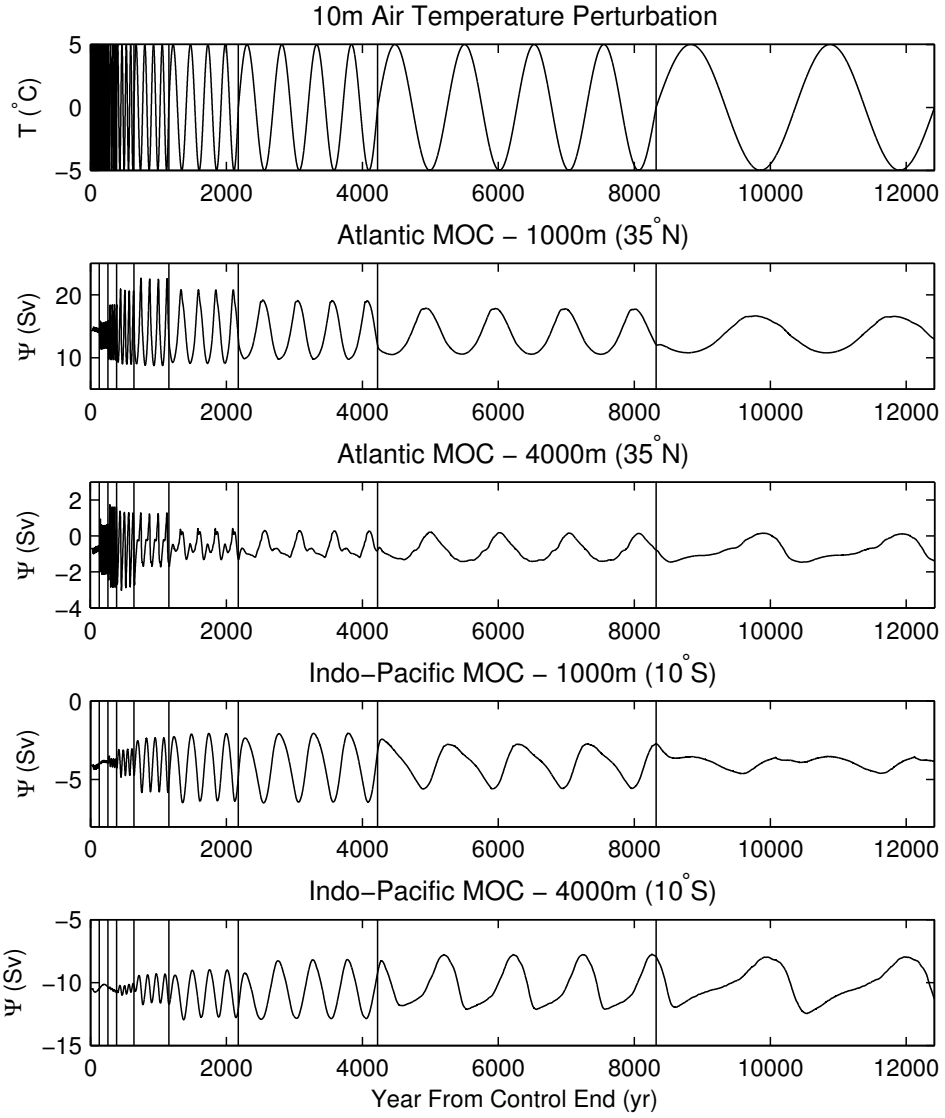

Figure 3.5: Timeseries of the 10m air temperature forcing profile (illustrated for 60°N, the latitude of maximum forcing) and the response timeseries of the meridional overturning streamfunction, Ψ, at 1000m and 4000m in both the Atlantic (at 35°N) and the Indo-Pacific (at 10°S) ocean basins.

western boundary between 60°N and 30°S in the Atlantic (as illustrated by markers A and B in Figure 1). The western boundary is the primary region in which strong ageostrophic flow can occur and, consequently, where the potential energy associated with meridional density (strictly, pressure) gradients can be converted into kinetic energy (Gregory and Tailleux, 2011; Sijp et al., 2012). Gnanadesikan (1999) also employs boundary layer theory to link meridional pressure gradients to a meridional frictional flow near the western boundary. The calculation of western

boundary gradients in our experimental setup is complicated due to the configuration's realistic topography. In order to minimise the impact of local topographic features and model resolution we avoid taking an exact western boundary value and, instead, take our western boundary quantities to be those averaged over a 10° longitude band adjacent to the western boundary. The precise width of this averaging band is not critical, but the emphasis on the western boundary is. Markedly diluting this contribution by, for example, doubling the width of the averaging band to 20° has a detrimental effect on the scaling accuracy, particularly in the abyssal Atlantic (not shown).

Another choice that must be made is the northern and southern location for the meridional density difference calculation. We use 60°N and 30°S respectively, but show that scaling is relatively insensitive to either choice in Section 3.3.3.

3.3.1 Scaling steady-state overturning as a function of depth

In this subsection, we demonstrate Equation 3.2's ability to predict the approximate vertical structure of model overturning as a function of depth in the control state ocean. One of the most significant advantages of the scaling proposed in Equation 3.2 is that it allows the meridional overturning streamfunction to be predicted at all depths as opposed to providing a single scale for each basin. This is particularly relevant in the Atlantic where there are two very different overturning cells overlaid on one another (Figure 3.3) that cannot necessarily be described by the same scale on a transient basis (Figure 3.5). A vertical profile of Atlantic Ψ_p computed from the control simulation is shown in Figure 3.6 alongside a vertical profile of basin-scale meridional overturning (taken to be the maximum magnitude of the overturning streamfunction - of either sign - between the equator and 30°N at each depth level). The free constant, c_ρ, has been constrained as the gradient of the linear fit between Ψ and Ψ_p: 0.79 (with a corresponding correlation coefficient of $r = 0.989$). There is an associated 1.7 Sv offset between Ψ and Ψ_p. This is, approximately, consistent with the fact that the model simulated overturning streamfunction, Ψ, integrates vertically to 1.3 Sv (not zero) in the Atlantic. This

discrepancy is likely associated with Bering Strait transport (of strength 1.1 Sv in the control experiment), which is not corrected for in the model streamfunction calculation. The upper 250m of the ocean feature shallow wind-driven overturning cells and have been excluded from this plot. Figure 3.6 demonstrates that the model provides a realistic estimate of the relative magnitude of overturning in both the upper and deep ocean and that the constructed depth profile is representative of the overturning simulated in the model. It is also seen that Ψ_p produces an accurate estimate of the depth scale of the upper overturning cell (in this case, approximately 3000m).

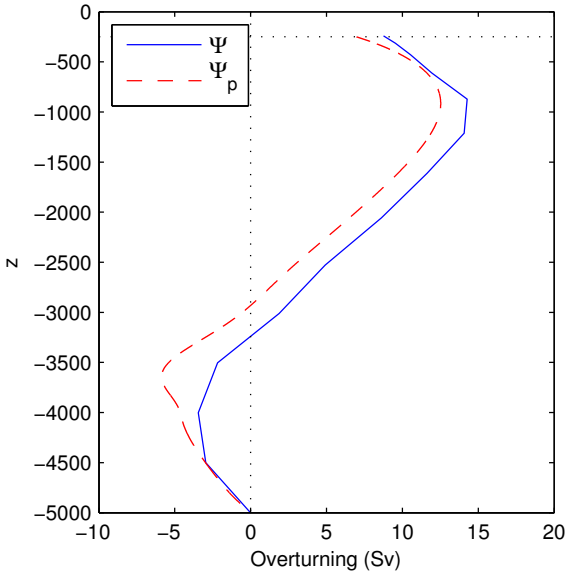

Figure 3.6: Vertical profile of Ψ (blue solid line) and Ψ_p (red dashed line) for the control overturning in the Atlantic. $\Psi(z)$ is the overturning streamfunction value of maximum amplitude at that level (whether positive of negative) taken between the equator and 30°N. Ψ_p is calculated from the twice integrated, basin-scale meridional density gradient.

3.3.2 Scaling transient overturning as a function of time

In this subsection, we investigate the predictability of upper and abyssal overturning in the Atlantic as a function of time at two fixed depths: 1000m and 4000m. These are the approximate depths of maximum overturning (associated with the NADW deep water cell) and minimum overturning (associated with the abyssal AABW cell) in the control run (see Figure 3.3 and Figure 3.6). In order

Forcing	1000m 35°N		4000m - 35°N	
Period (yrs)	Mean	Range	Mean	Range
8	14.3	0.1	-0.7	0.3
16	13.7	4.1	-0.7	2.7
32	13.6	8.7	-0.7	4.5
64	13.6	11.6	-0.4	4.1
128	13.7	13.7	-0.5	3.0
256	13.8	11.6	-0.6	1.7
512	13.8	9.3	-0.6	1.5
1024	13.6	7.2	-0.8	1.6
2048	13.5	5.8	-0.8	1.6

Table 3.1: Mean and range of Ψ at 1000m (35°N) and 4000m (35°N) in the Atlantic, computed for the final oscillation of each forcing series. All statistics are given in units of 1 Sv = 10^6 m^3 s^{-1}.

to determine the timescales over which such a scaling might be valid, we begin by exploring a series of periodic variable buoyancy forcing scenarios in a coarse resolution global ocean model as described in Section 3.2.3. The robustness of the scaling described by Equation 3.2 to model resolution and the nature of forcing variability is explored in Section 4.

3.3.2.1 Upper ocean overturning at 1000m, 35°N

The mean and range statistics of model simulated overturning, Ψ, at 1000m at 35°N in response to the periodic buoyancy forcing scenarios are tabulated in Table 3.1 (calculated for the final cycle of each forcing series), the timeseries of model simulated overturning response is plotted in Figure 3.5, and the spatial structure of induced Atlantic overturning variability is depicted in Figure 3.7.

The experimental forcing induces large amplitude, asymmetric oscillations in overturning, peaking in range at 13.7 Sv at 128 year timescales and declining for longer periods. This resonance-like behaviour is consistent with the findings of Lucas et al. (2005) who applied a similar experimental design to an idealised, single basin ocean model and determined that this behaviour in their model was linked to an interaction between the diffusive timescale and the timescale of Rossby wave anomaly propagation. The structure of the induced overturning variability also

changes with forcing period (Figure 3.7). High frequency overturning anomalies (8 and 16 year timescales) do not penetrate south of the equator until multi-decadal (32 and 64 year) timescales, consistent with the idea of an 'equatorial buffer' to high-frequency variability formalised by Johnson and Marshall (2002). At the longest timescales, the equator ceases to act as a buffer to the propagation of overturning anomalies. As a result, short timescale forcing is characterised by intense, deep overturning anomalies at high-latitudes, whilst longer timescale forcing results in a broader, but shallower, pattern of variability.

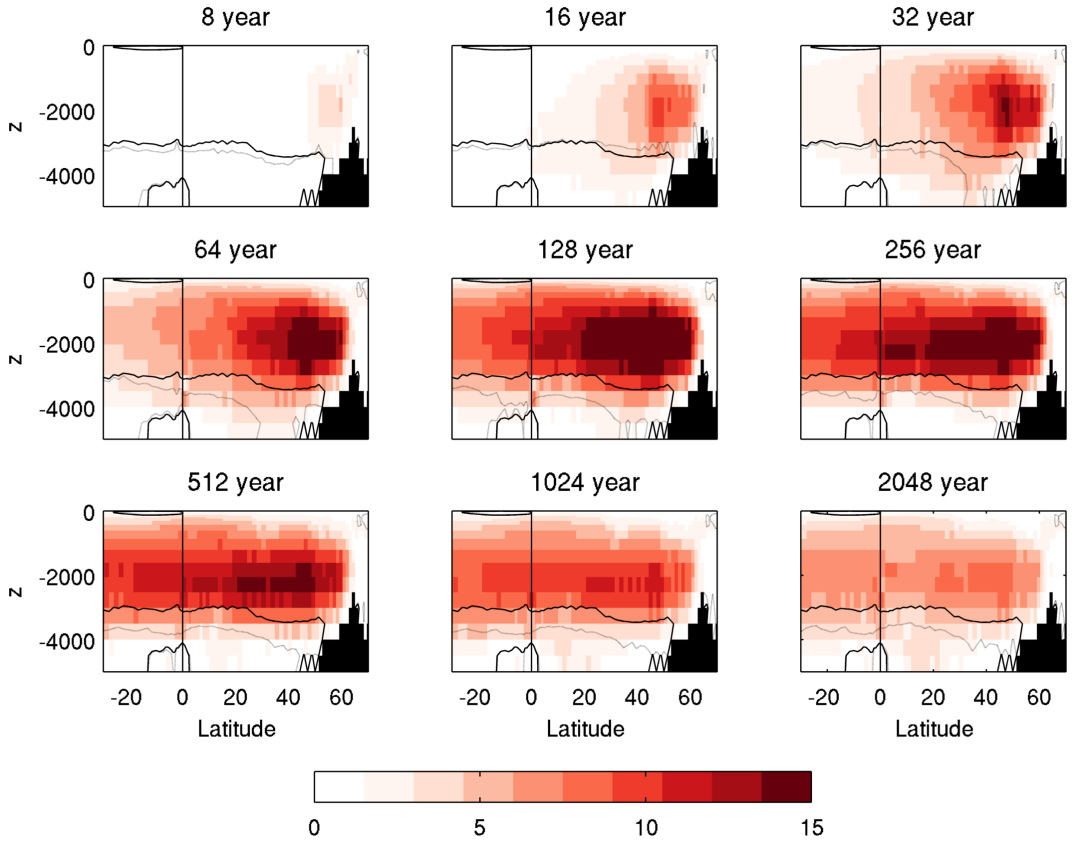

Figure 3.7: Meridional sections depicting the range of Ψ in the Atlantic for each of the forcing frequencies (units: 1 Sv = 10^6 m^3s^{-1}). The solid black contour indicates the zero overturning contour (separating the NADW and AABW cell) of the control simulation overturning and the dotted black contour represents the zero overturning contour at maximum meridional density gradient forcing.

The basin-scale overturning streamfunctions inferred from twice-integrated meridional density gradients, Ψ_p, are constructed for the transient experiments according to the method described in the introduction to Section 3.3. The values of the correlation coefficient between model simulated overturning, Ψ, and Ψ_p at 1000m are

given in Table 3.2. Timeseries of both Ψ and Ψ_p anomalies (with the temporal mean signal for each timescale removed) are plotted together for the upper ocean in Figure 3.8. The free geometric constant, c_ρ, is taken to be the gradient of linear fit Ψ against Ψ_p for the longest timescale forcing (in this case, 2048 year). This corresponds to 0.86 at 1000m. Whilst it is visually apparent in Figure 3.8 that there is a short lagged response between Ψ and Ψ_p in the Atlantic (in which Ψ_p precedes changes in overturning, Ψ, by approximately 4 years), all correlation coefficients are quoted without any lag for consistency and transparency.

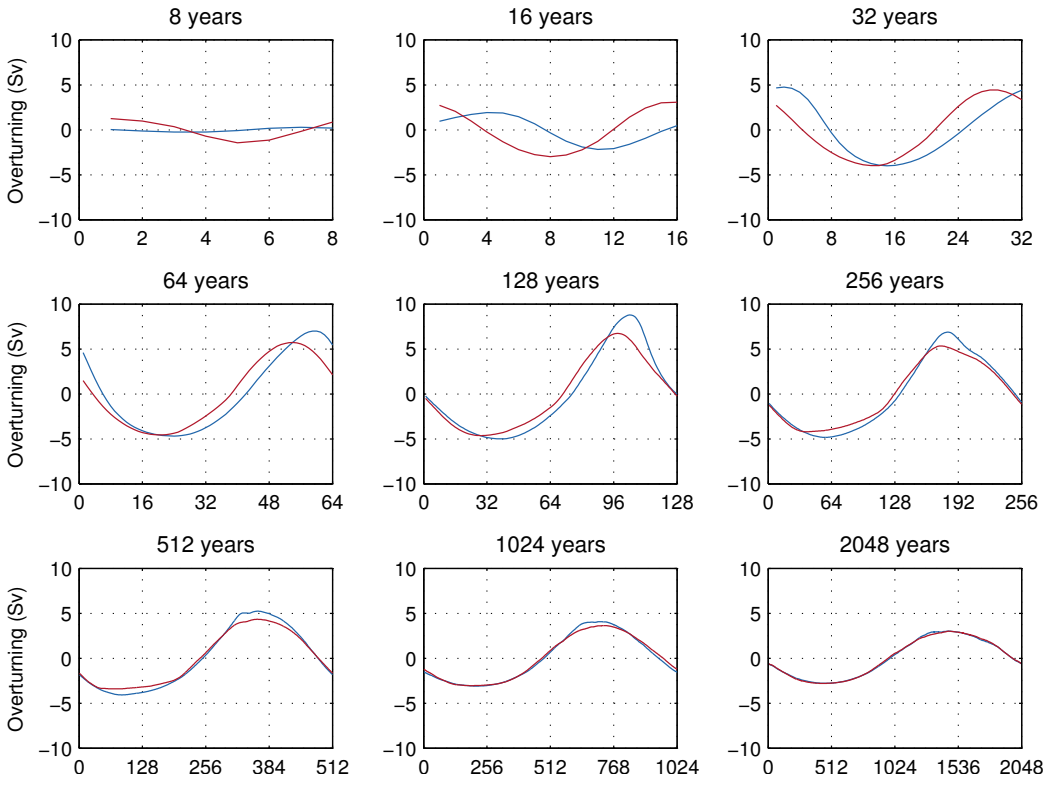

Figure 3.8: Timeseries depicting the variability (the signal minus the oscillation mean) of Ψ (blue) and Ψ_p (red) at 1000m (35°N) in the North Atlantic plotted for the final oscillation of each surface buoyancy forcing period in the deterministically forced ORCA2 simulation.

We see a weak predictive ability of Ψ_p at 8 year timescales with the magnitude of overturning overestimated by a factor of 5. At 16 year timescales, correlation is still weak (due to the lag described above), but the predicted range of overturning is more consistent with the model simulated Ψ at 35°N (though still overestimated by a factor 1.5). However, by the 32 year timescale both the pacing and range of overturning is accurately predicted. Correlation is greater than 0.9 for

Forcing Period (yrs)	Deterministic ORCA2		Timescale Band (yrs)	Stochastic ORCA05
	1000m	4000m		1000m
8	0.040	-0.989	6-10	0.354
16	0.130	0.600	10-25	0.421
32	0.739	0.963	25-50	0.861
64	0.923	0.935	50-80	0.793
128	0.969	0.897	80-180	0.898
256	0.991	0.918	180-325	0.987
512	0.998	0.878	325-600	0.909
1024	0.996	0.963	-	-
2048	0.999	0.952	Unfiltered	0.730

Table 3.2: Correlation coefficients between model simulated overturning, Ψ, in the Atlantic at 35°N and inferred overturning, Ψ_p, given for each forcing timescale. Correlations are quoted without lag. In the stochastically forced simulation, each timescale component is determined using a band pass filter.

all timescales longer than (and including) 64 years and greater than 0.99 for all timescales longer than (and including) 256 years. Changes in the magnitude of induced overturning with forcing timescale are predicted, including the resonant 128 year forcing period.

3.3.2.2 Abyssal ocean overturning at 4000m, 35°N

Unlike in previous scaling studies, Ψ_p retains a function of depth allowing us to also attempt to scale abyssal overturning in the Atlantic at 35°N at a depth of 4000m. In contrast to the large amplitude oscillations seen at 1000m, meridional overturning at 4000m has a much weaker response (Table 3.1). However, the response of abyssal overturning at 4000m is highly nonlinear (Figure 3.5). Indeed, there is a clear transition to a biharmonic signal at the intermediate 128 and 256 year forcing periods. Like in the upper ocean, there is also resonance-like behaviour observed in deep ocean overturning at 4000m, but, surprisingly, this occurs at the much shorter 32 year period forcing (cf. 128 year period forcing at 1000m). As discussed in Section 3.3.2.1, the upper overturning cell's response to high frequency buoyancy forcing is characterised by intense, deep overturning anomalies at mid- to high-northern latitudes (Figure 3.7). Indeed, the upper overturning cell expands to

occupy the entire water column at the 32 year forcing period, penetrating through the 4000m depth level. As a result, the greatest magnitude response at 4000m is actually observed at timescales far shorter than that at 1000m. Given the complex nature of the overturning response to simple periodic forcing seen here, we do not seek to understand the precise dynamics underlying this behaviour, but instead only seek to test whether Ψ_p can adequately predict the shape and amplitude of the response.

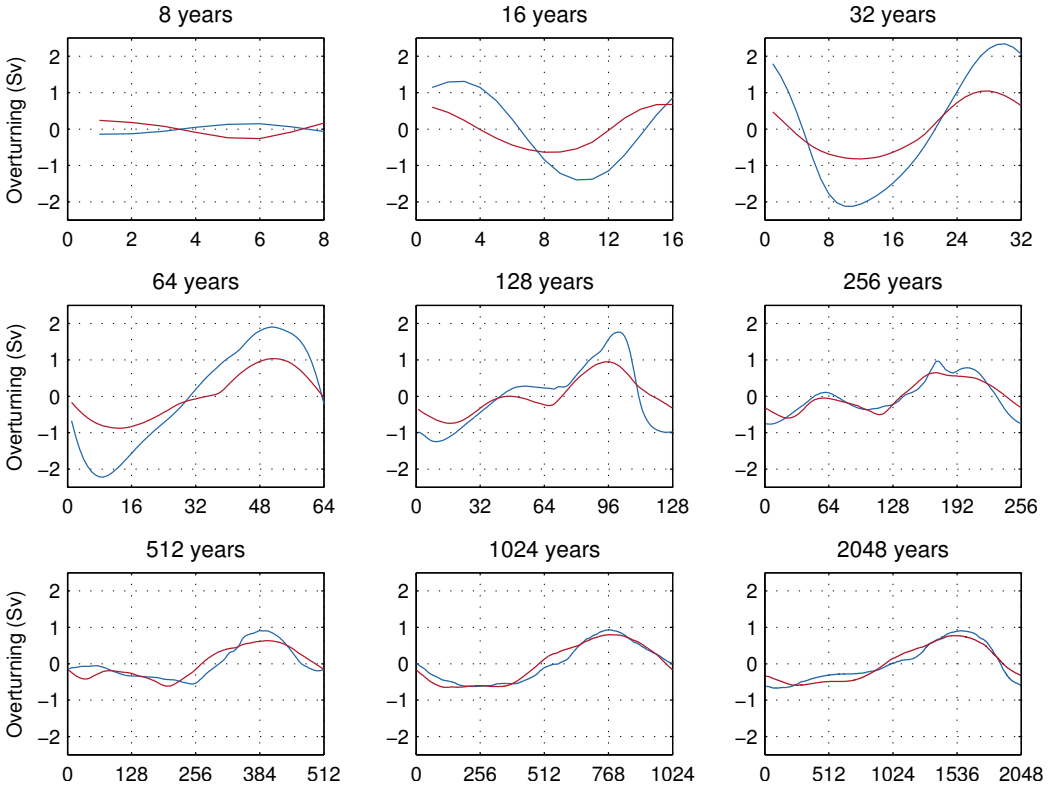

Figure 3.9: Timeseries depicting the variability (the signal minus the oscillation mean) of Ψ (blue) and Ψ_p (red) at 4000m (35°N) in the North Atlantic plotted for the final oscillation of each surface buoyancy forcing period in the deterministically forced ORCA2 simulation.

The values of the correlation coefficient between the model simulated overturning, Ψ, and density-gradient inferred overturning, Ψ_p, at 4000m are given in Table 3.2. Timeseries of both Ψ and Ψ_p anomalies (with the temporal mean signal for each timescale removed) are plotted for the abyssal Atlantic in Figure 3.9. The free constant, c_ρ, is equal to 0.26 at 4000m. This number is significantly smaller than that observed at 1000m. This is likely due to a reduction in the zonal length scale with depth, exacerbated by the presence of the mid-Atlantic ridge. As in the

upper ocean, good correlations are seen from 32 year forcing periods onwards, but the amplitude of response is not accurately predicted until 256 year forcing timescales. Since the large amplitude deep ocean response seen at shorter timescales is due to high-frequency, localised incursions of the upper overturning cell through the 4000m depth level (Figure 3.7), it is possible that these narrow events are not triggered by, or reflected in, basin-scale pressure gradients at this depth and, therefore, may not be well-captured by a basin-scale scaling relationship. However, it is worth noting that the high correlations at and beyond the 128 year forcing cycle are very strong, despite the highly nonlinear nature of the signal. Furthermore, Ψ_p correctly predicts the transition to the biharmonic overturning signals seen at 128, 256, and 512 year forcing periods and the relative magnitudes of each peak within these responses.

3.3.3 The relative roles of the northern and southern boundary

The forcing applied in our idealised scenarios is focussed on high northern latitudes. It is, thus, a valid question as to what proportion of the variability in the overturning streamfunction comes from density variations at the northern and southern boundary points respectively and, consequently, whether the veracity of the proposed scaling relationship has actually been successfully demonstrated in a transient scenario in which we also have variability at the southern boundary. Furthermore, can we determine how sensitive our results are to the choice of latitude of the northern and southern boundary points?

Temporal anomalies in Ψ_p are decomposed into northern and southern boundary variability contributions at 1000m (Figure 3.10) and 4000m (Figure 3.11) by using a fixed, time-mean density profile at the opposing boundary. Density variations at the southern boundary point make a negligible contribution to Ψ_p until 256 and 512 year forcing periods. This is, in part, because there is little propagation of induced variability beyond the equator at decadal timescales (Figure 3.7). Moreover, adjustment of the low-latitude pycnocline in response to overturning anomalies is

determined by the filling of the deep ocean with dense water and, consequently, occurs over long, centennial timescales. By 2048 year timescales, northern and southern boundary contributions to the variability in Ψ_p at 4000m are equal in magnitude.

At the longest forcing timescales, the anomalies in Ψ_p at 1000m due to northern and southern boundary variability appear out of phase. This is because when upper ocean overturning is strong, the deep ocean fills with dense water, the low-latitude pycnocline shoals, southern boundary density increases and the meridional density gradient decreases. It then follows that Ψ_p due to southern boundary variability decreases as a consequence of this. However, these processes only occur in phase at multi-centennial timescales.

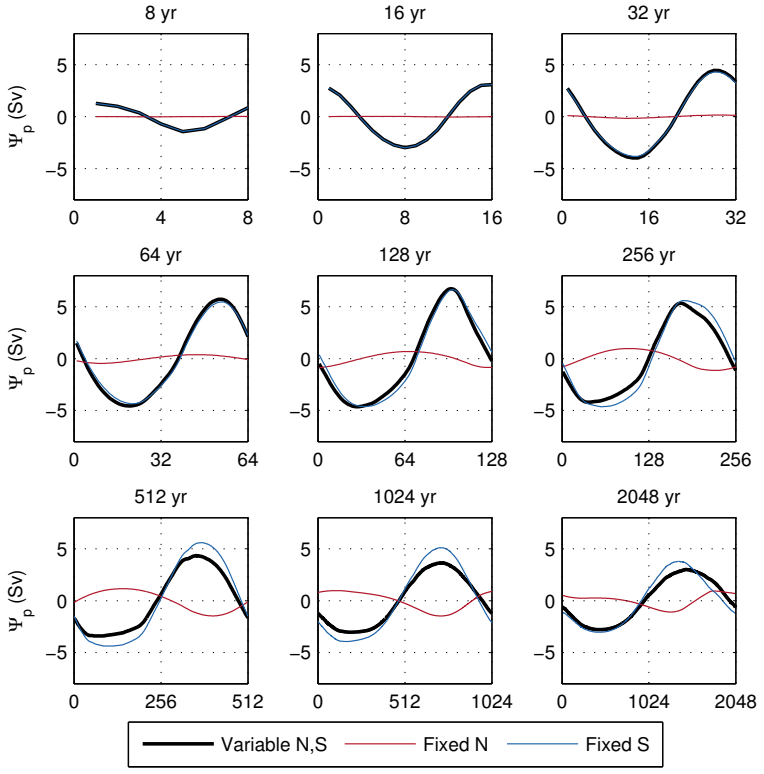

Figure 3.10: Temporal anomalies of Ψ_p in the Atlantic at 1000m constructed using a) both a variable northern and southern boundary (bold black), b) a fixed northern boundary corresponding to the temporal mean profile of ρ_N (red) and c) a fixed southern boundary corresponding to the temporal mean profile of ρ_S (blue).

In our analysis, we have chosen to use a northern boundary point at 60°N and a southern boundary point at 30°S. The corollary of the above paragraph is that

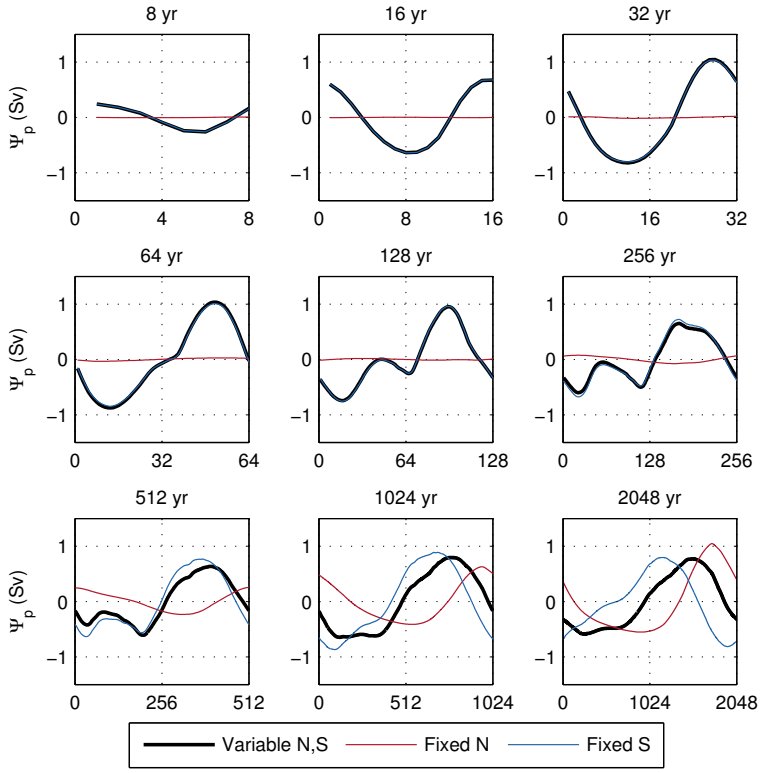

Figure 3.11: Temporal anomalies of Ψ_p in the Atlantic at 4000m constructed using a) both a variable northern and southern boundary (bold black), b) a fixed northern boundary corresponding to the temporal mean profile of ρ_N (red) and c) a fixed southern boundary corresponding to the temporal mean profile of ρ_S (blue).

the scaling used here is largely insensitive to the choice of southern boundary in our decadal to centennial timescale forcing scenarios. At millennial timescales, the choice of southern boundary becomes more important, particularly in the abyssal Atlantic where the southern boundary contribution is largest. Highest correlations are found when the southern boundary is set to that of the basin at 30°S (not shown). Whilst horizontal pressure gradients at low-latitudes in the subsurface ocean are typically weaker (as discussed by Griesel and Maqueda (2006)), the northern boundary does not need to be pinned to 60°N either. When scaling overturning at 1000m, the northern boundary can be moved southwards through the subpolar gyre to a latitude of 50°N without having a detrimental effect on the predictive ability of the scaling (not shown). However, in order to capture the nonlinear dynamics of the overturning signal at 4000m, the northern boundary must be taken no further south than 55°N. The topographic barrier between the

Atlantic and the Arctic at approximately 65°N (see Figure 3.3) acts as a northern limit to the choice of northern boundary latitude. Intervening topography disrupts the maintenance of large-scale meridional pressure gradients between the northern and southern basin boundaries in the deep ocean and the fundamental principles of the scaling then break down.

3.3.4 The AMOC sensitivity to density changes at different depths

Since Ψ_p is constructed using twice vertically integrated density gradients, it is dependent on meridional density differences throughout the water column, regardless of which depth it is evaluated at. Here, we investigate the sensitivity of scaled overturning, Ψ_p, to changes in meridional density difference, $\Delta\rho_y$, at different depths.

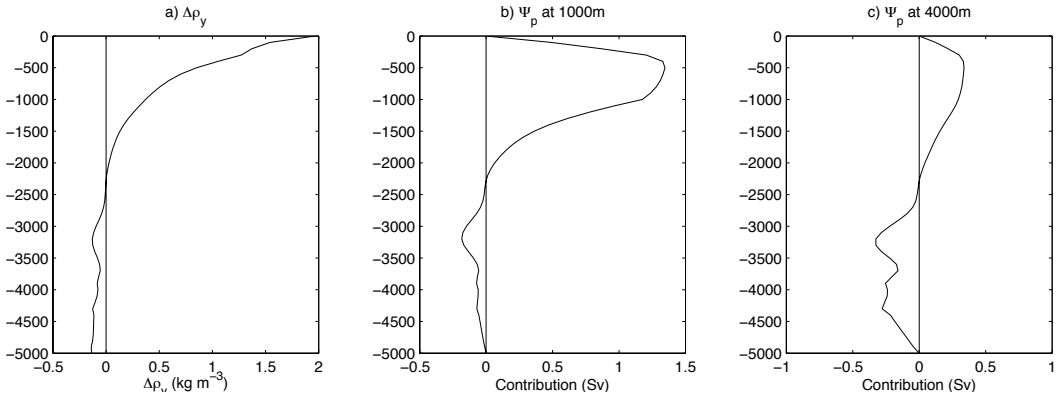

Figure 3.12: Vertical profiles of a) the meridional density difference (units: kg m^{-3}) in the control simulation and the contribution of the meridional density difference at different depths (integrated over 100m thick vertical levels constructed using linear interpolation of model output) to Ψ_p at both b) 1000m and c) 4000m (units: 1 Sv = 10^6 m^3 s^{-1}). Each contribution profile sums to the respective control value of overturning.

We begin by quantifying the contribution of $\Delta\rho_y$ at different depth levels to the control value of Ψ_p at both 1000m and 4000m (Figure 3.12). This is computed (at depth z) as the difference between Ψ_p calculated using a full density profile and Ψ_p calculated using a reduced density profile in which $\Delta\rho_y(z)$ is set to zero. Positive values indicate that depth z makes a positive contribution to Ψ_p (and vice versa).

Whilst the meridional density difference is largest near the surface, the strength of Ψ_p is determined, predominantly, by interior density gradients. Even density gradients below 3000m play a significant role in setting the strength of Ψ_p in the upper ocean.

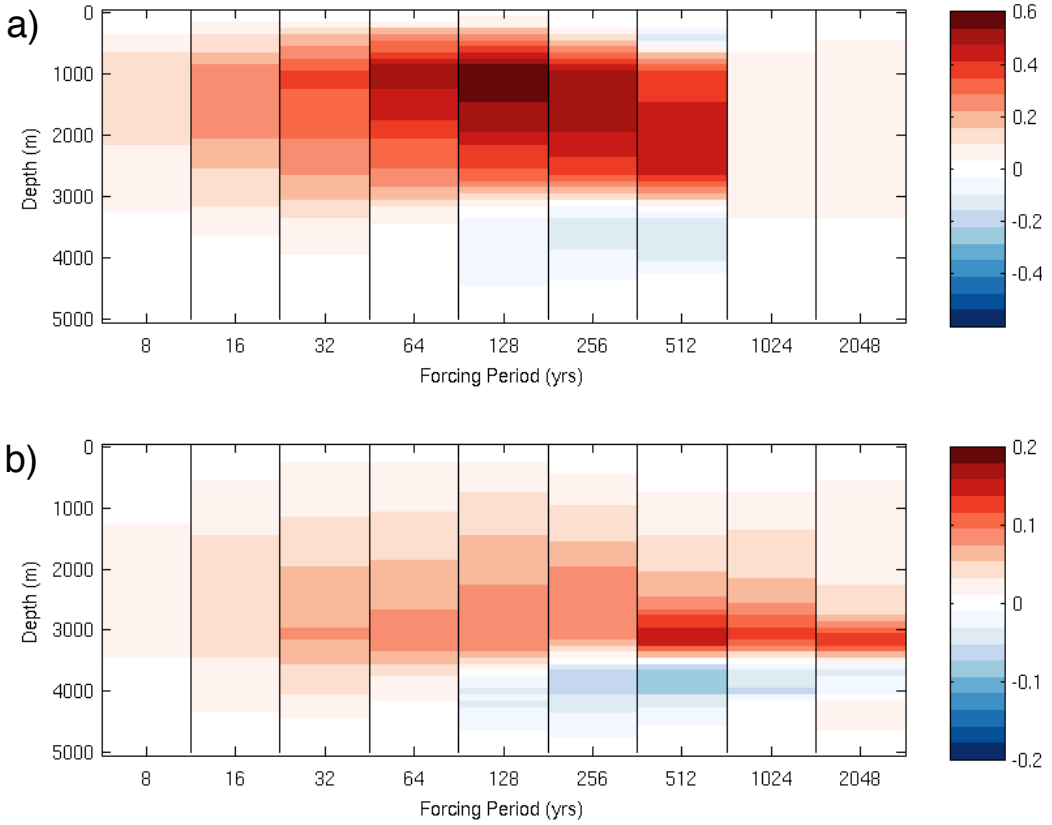

Figure 3.13: The sensitivity of Ψ_p at a) 1000m and b) 4000m to changes in meridional density difference at different depths and timescales. Positive values imply that $\Delta\rho_y$ is enhancing the overall variability in Ψ_p and negative values imply that $\Delta\rho_y$ is attenuating this variability. The latter can occur if $\Delta\rho_y(z)$ is anti-correlated to Ψ_p. Model output is interpolated onto 100m depth intervals. Please see Section 3.3.4 for full details of this construction.

The sensitivity of Ψ_p to density changes at different depths for different timescales can be determined in much the same way for the transient simulations. Figure 3.13 depicts the difference between the range of Ψ_p calculated using a full density profile and the range of Ψ_p calculated using the reduced density profile (for both the upper and abyssal ocean). It is clear that the sensitivity of overturning to changes in density at different depths varies significantly as a function of time. As

in the control simulation, changes in density throughout the water column can have a large impact on the variability of meridional overturning in both the upper and abyssal Atlantic. Therefore, simplified scaling relationships based on the surface meridional density gradient or fixed depth measures of meridional density/pressure difference (e.g. averaged over the upper ocean) alone are insufficient to capture the complexities of meridional overturning across multiple timescales.

3.4 Scaling the AMOC response to stochastic forcing

Scaling relationships are typically used to help improve our general understanding of ocean behaviour or used in simple box models to parameterise large-scale flows governed by unresolved dynamics. However, little practical usage has been demonstrated previously in the real ocean (or in high resolution ocean models). Whether a basin-scale meridional density gradient measure can be used to predict or reconstruct accurate timeseries of meridional overturning variability from hydrography remains an open question. In the previous section, we demonstrated that Ψ_p is a good predictor of meridional overturning at 1000m for timescales of 16 to 32 years and longer under sinusoidal buoyancy forcing. However, such periodic forcing scenarios (incorporating variability in just one atmospheric variable) are clearly idealised. Therefore, we extend our analysis to test the ability of twice-integrated meridional density gradients to predict upper Atlantic overturning in the higher resolution, stochastically forced simulation used in Mecking et al. (2014).

This simulation was conducted using the global ORCA05 configuration of NEMO with a nominal horizontal resolution of 0.5° and forced by North Atlantic Oscillation (NAO) inspired stochastic forcing. NAO based forcing fields were produced by regressing the CORE v2.0 interannually varying forcing fields onto the observed NAO index. A stochastic NAO index was generated with a white-noise spectrum in each month, normally distributed with mean and standard deviation taken from monthly-averaged observational data. The regression fields are then

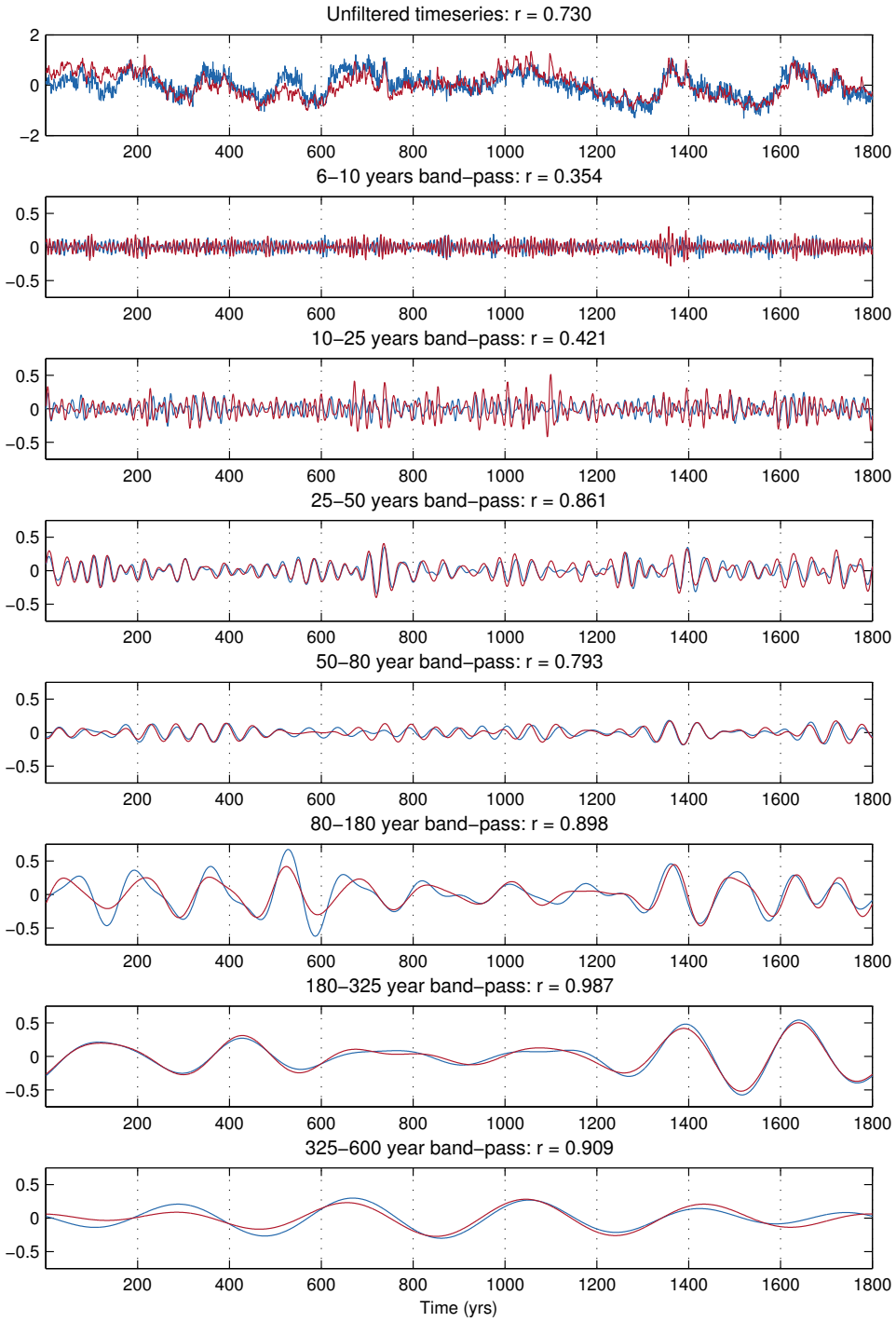

Figure 3.14: De-trended timeseries of Ψ (blue) and Ψ_p (red) at 1000m (35°N) in the North Atlantic for the stochastically forced ORCA05 simulation and band pass filtered for timescales comparable to the deterministic variable buoyancy forcing experiments.

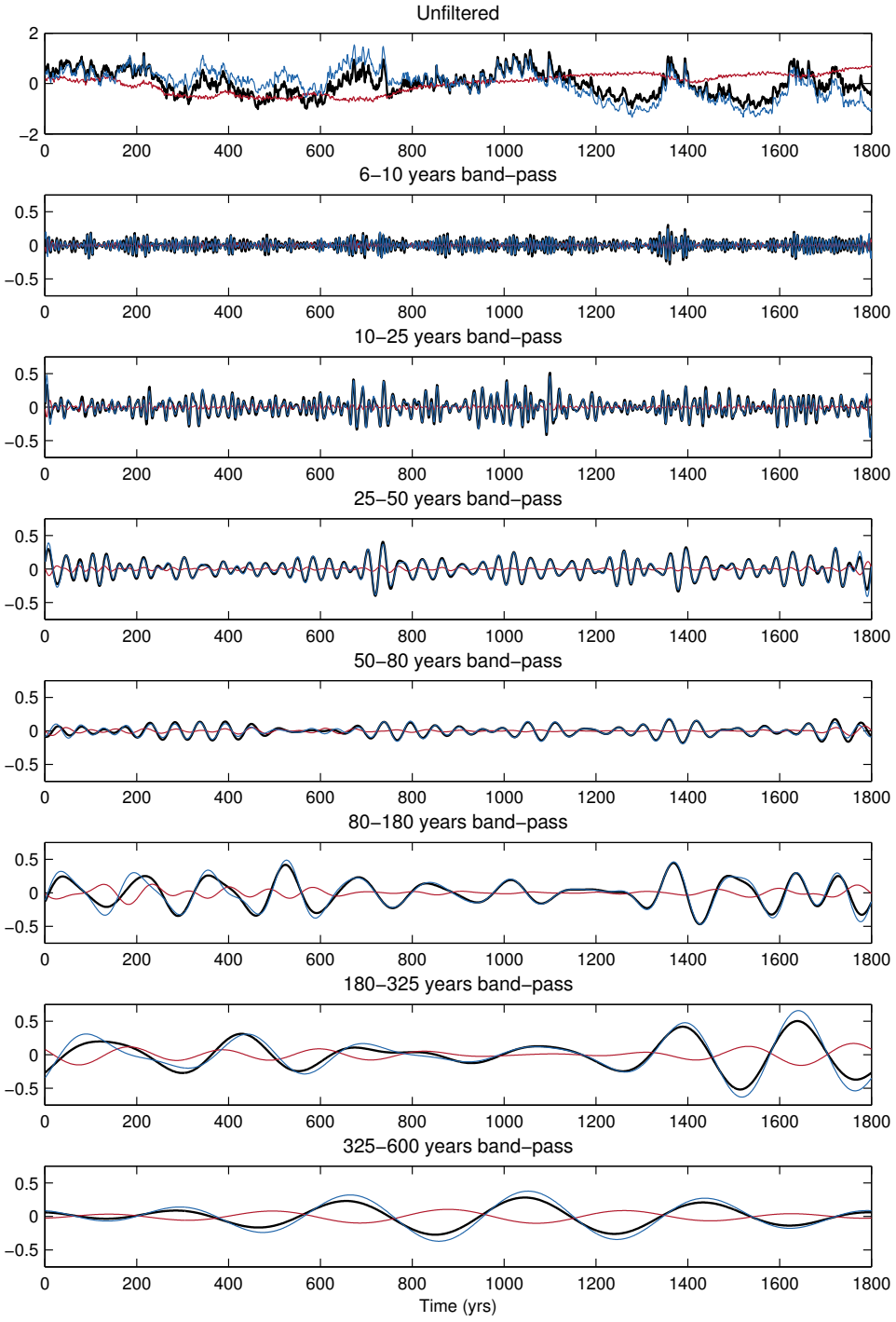

Figure 3.15: De-trended timeseries of Ψ_p at 1000m (35°N) in the North Atlantic for the stochastically forced ORCA05 simulation (band pass filtered for timescales comparable to the deterministic variable buoyancy forcing experiments) constructed using a) both a variable northern and southern boundary (bold black), b) a fixed northern boundary corresponding to the temporal mean profile of ρ_N (red) and c) a fixed southern boundary corresponding to the temporal mean profile of ρ_S (blue).

multiplied by the monthly NAO index and superimposed onto the CORE v2.0 normal year forcing dataset. In contrast to the deterministically forced ORCA2 experiments, there is variability in all atmospheric variables, including both 10m air temperature and wind velocity. For further details, the model setup and simulation is described in full in Mecking et al. (2014). Since deep ocean circulation is still drifting in this simulation, we only test Ψ_p in the upper Atlantic Ocean at a depth of 1000m at 35°N. We make use of 1800 years of model simulation allowing us to explore comparable timescales to many of those tested in the deterministic experimental setup (up to 600 year timescales) using a series of band pass filters to separate out the corresponding signal components (see Table 3.2). The scaled overturning streamfunction in ORCA05 is calculated in the same way as in ORCA2, according to the method set out in Section 3.3.

The correlation coefficients (r) between the model simulated overturning, Ψ, and Ψ_p are given in Table 3.2. The free geometric constant, c_ρ, is again taken to be the gradient of the linear fit of Ψ against Ψ_p for the longest timescale forcing (in this case, the 325-600 year band): 0.69. Despite the differences in resolution and forcing, this figure is comparable to that fitted to the ORCA2 control simulation depth profile in Section 3.3.1 (0.79) and at 1000m in the transient ORCA2 experiments in Section 3.3.2 (0.86). Timeseries of both Ψ and Ψ_p anomalies for each different frequency band are plotted in Figure 3.14. As in the periodically forced coarse resolution experiments, we see good correlations at short multi-decadal timescales (the 25-50 year band) with a correlation coefficient greater than or equal to 0.9 at the 80-180 year band and longer, explaining at least 81% of the observed variability. Moreover, the amplitude of overturning anomaly across these timescales is also well modelled. As a result, the unfiltered Ψ and Ψ_p timeseries correspond remarkably well (with an unfiltered correlation coefficient of 0.73). Northern boundary variability makes the largest contribution to Ψ_p at all timescales. As in Section 3.3, the effect of southern boundary variability is largely negligible on decadal timescales, but becomes increasingly significant at centennial timescales (Figure 3.15).

3.5 Scaling Indo-Pacific overturning

Whilst there are no direct variations in buoyancy forcing applied outside of the North Atlantic, variability induced in the Atlantic propagates internally throughout the global ocean. Idealised theoretical models suggest that transport anomalies can be transmitted globally (on timescales shorter than the advective timescale) via a combination of coastal and equatorial Kelvin waves, which are then conveyed into the ocean interior via Rossby waves propagating from the eastern boundary (Huang et al., 2000; Johnson and Marshall, 2004).

Forcing	1000m 10°S		4000m - 10°S	
Period (yrs)	Mean	Range	Mean	Range
8	-4.1	0.2	-10.5	0.0
16	-3.9	0.1	-10.3	0.1
32	-3.9	0.5	-10.7	0.2
64	-3.8	1.7	-10.4	0.7
128	-3.9	3.5	-10.5	2.4
256	-4.0	4.3	-10.8	3.8
512	-4.1	4.4	-10.6	4.7
1024	-4.0	2.8	-10.3	4.4
2048	-3.9	1.1	-10.2	4.5

Table 3.3: Mean and range of Ψ at 1000m (10°S) and 4000m (10°S) in the Indo-Pacific, computed for the final oscillation of each forcing series. All statistics are given in units of 1 Sv = 10^6 m^3 s^{-1}.

The mean and range of Indo-Pacific overturning are given in Table 3.3 and response timeseries are plotted in Figure 3.5 for both 1000m and 4000m at 10°S (where strong Indo-Pacific overturning exists in both the upper and abyssal ocean). At this latitude, mean overturning is approximately -4 Sv at 1000m and -10 Sv at 4000m, whilst the MOC response to remote buoyancy forcing has a maximum range of 4.4 Sv at 1000m and 4.7 Sv at 4000m. We do not see significant propagation of variability until 64 year timescales; consistent with the idea of an 'equatorial buffer' to the global propagation of MOC variability described by Johnson and Marshall (2004) in which the equator effectively acts as a low-pass filter on MOC anomalies, confining anomalies on multi-decadal (and shorter) timescales

to their basin of origin. At the longest forcing timescales we see that about 30-40% of the high-latitude AMOC variability propagates to the Indo-Pacific basin at 10°S. This is in good agreement with the asymptotic fraction predicted by Johnson and Marshall (2004) for centennial periodic forcing of a simple two basin model of inter-basin MOC anomaly propagation, though the timescales of intermediate propagation appear to be somewhat longer in our GCM experiments. As in the Atlantic, we see a resonant response in the Indo-Pacific. However, the resonant period of the Indo-Pacific basin is significantly longer at 512 years (compared with 128 years at 1000m in the North Atlantic) suggesting that it is not simply a propagation of the resonant Atlantic signal and could be linked, at least in part, to the differing basin geometry.

Forcing	a) N. Pacific - S. Indian		b) N. Pacific - S. Pacific	
Period (yrs)	1000m	4000m	1000m	4000m
64	0.442	0.813	0.158	0.877
124	0.871	0.837	0.861	0.995
256	0.956	0.972	0.953	0.990
512	0.993	0.995	0.498	0.973
1024	0.952	0.964	0.319	0.975
2048	0.619	0.888	-0.284	0.976

Table 3.4: Correlation coefficients between Ψ and Ψ_p for Indo-Pacific overturning at 10°S. Correlations are quoted without lag. Ψ_p is constructed using the meridional density difference between the North Pacific and both a) the southern Indian Ocean and b) the South Pacific.

A number of previous studies have attempted to scale Indo-Pacific overturning according to measures of meridional density gradient or meridional pressure gradient, typically using models with idealised topography. For example, de Boer et al. (2010) represent the Indo-Pacific basin as a simple rectangular box. Whilst Schewe and Levermann (2009) represent the Indian and Pacific Oceans with more realistic geometry, the low-latitude Indonesian connection between the Indian and Pacific Oceans is closed and the Indonesian through-flow is prescribed so the two basins could be regarded as distinct. The more realistic geometry of ORCA2 (Figure 3.1) makes scaling analysis in this region far less trivial. For instance, there is no immediately obvious definition of the western boundary of the combined Indo-Pacific basin along which to calculate the meridional density difference. Depending on

whether we consider the upper or abyssal ocean, the southern extent of a continuous western boundary will either be in the Indian Ocean or the Pacific Ocean.

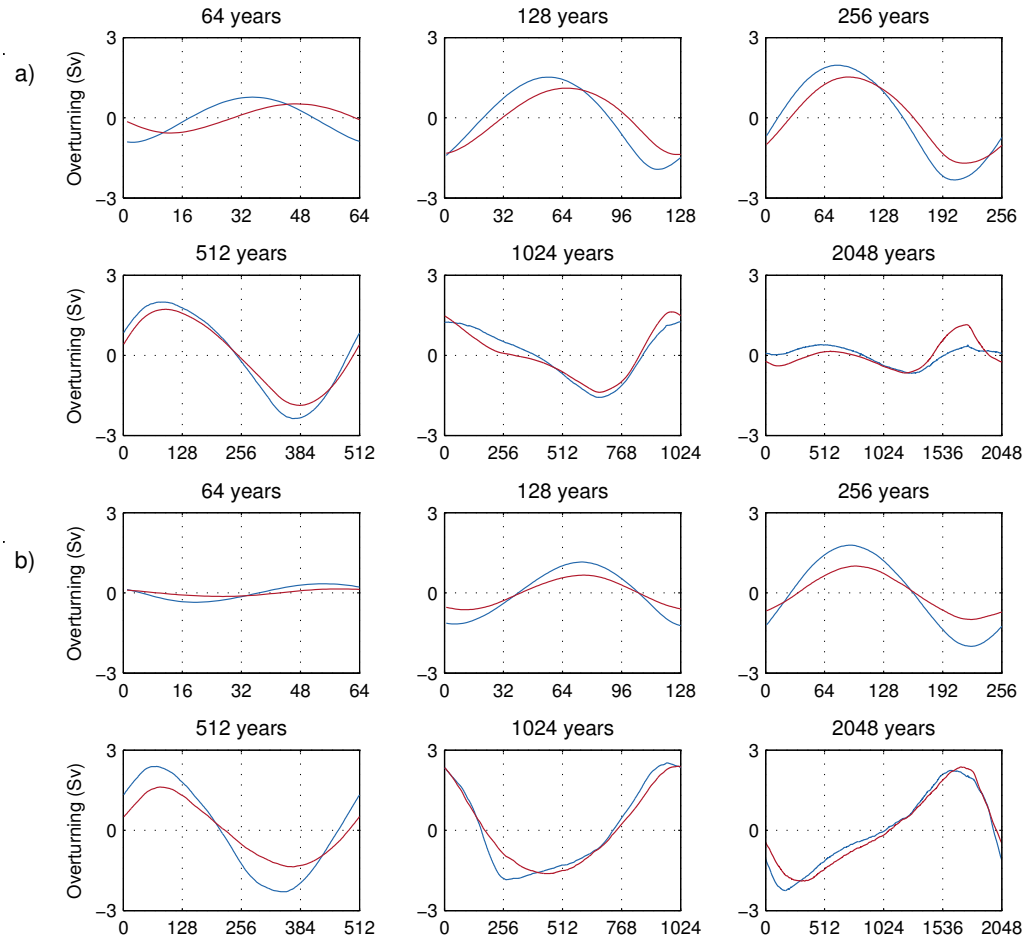

Figure 3.16: Temporal anomalies of Ψ (blue) and Ψ_p (red) at a) 1000m (10°S) (constructed using a meridional density gradient between the northern Pacific Ocean boundary and the southern Indian Ocean boundary) and b) 4000m (10°S) (constructed using a meridional density gradient calculated across the Pacific Ocean only) in the Indo-Pacific basin for the 64, 128, 256, 512, 1024, and 2048 year timescale experiments in the ORCA2 simulation.

Therefore, we construct two different measures of Ψ_p based on a meridional density difference defined along the western boundary between the North Pacific at 40°N and a) the southern Indian Ocean off the northeast tip of Madagascar at 25°S and b) the South Pacific at the northeast tip of New Zealand at 39°S (see Figure 3.1). The precise location of each southern boundary point is chosen such that we have sufficiently deep bathymetry to scale overturning throughout the water

column. Irrespective of the boundary definition, we take the zonal length scale, L_x, of the Indo-Pacific basin to be 15,000 km (three times that of the Atlantic) and leave the remaining scale parameters unchanged (see Section 3.3). The Indonesian connection facilitates the maintenance of zonal pressure gradients across the entire width of the upper Indo-Pacific basin and the propagation of upper ocean overturning anomalies (Johnson and Marshall, 2004) making scaling (a) physically more appropriate for upper ocean overturning. However, this is not the case in the abyssal ocean in which we have an intervening topographic barrier. At 4000m, Indo-Pacific overturning is dominated by the Pacific contribution making scaling (b) physically more appropriate at this location. Correlations between Indo-Pacific overturning Ψ and the two different Ψ_p scalings for Indo-Pacific overturning are shown in Table 3.4. No information is given for 8, 16, and 32 year forcing cycles as Indo-Pacific overturning failed to reach equilibrium during these forcing cycles and the amplitude of the response was very small (see Figure 3.5 and Table 3.3 respectively).

In line with our expectations, method (a) effectively predicts upper but not deep ocean overturning, whereas method (b) effectively predicts deep but not upper ocean overturning (Table 3.4). The progression in amplitude increase up to the resonant timescale of 512 years is also seen (Figure 3.16), but the observed correlation drops markedly for the upper ocean at 2048 year forcing timescales. This coincides with a marked change in overturning at this timescale to a weak 1.1 Sv biharmonic signal that is not understood here. Whilst Ψ and Ψ_p are not perfectly correlated at this timescale, Ψ_p does well predict this transition to a biharmonic signal.

Timeseries of Ψ and $\Psi_p(a)$ (for 1000m) and $\Psi_p(b)$ (for 4000m) are illustrated for selected forcing periods in Figure 3.16. As before, the free constant, c_ρ, is taken to be the gradient of the linear fit between Ψ and Ψ_p at the longest timescale forcing: 0.81 at 1000m for $\Psi_p(a)$ and 0.93 at 4000m for $\Psi_p(b)$ (consistent with $c_\rho = 0.86$ in the Atlantic at 1000m). Due to the weak correlation of $\Psi_p(a)$ at 2048 year timescales, c_ρ is estimated from the 1024 year forcing cycle for greater

accuracy. The relative contributions of northern and southern boundary variability to $\Psi_p(a)$ and $\Psi_p(b)$ are depicted in Figure 3.17. Despite the propagation of overturning variability from the Atlantic via the southern boundary, it can be seen that density variations at both the northern and southern boundaries make significant contributions to the overall streamfunction. Therefore, the meridional density *difference* is critical to reconstructing Indo-Pacific meridional overturning. Considering either northern or southern boundary density variability alone is

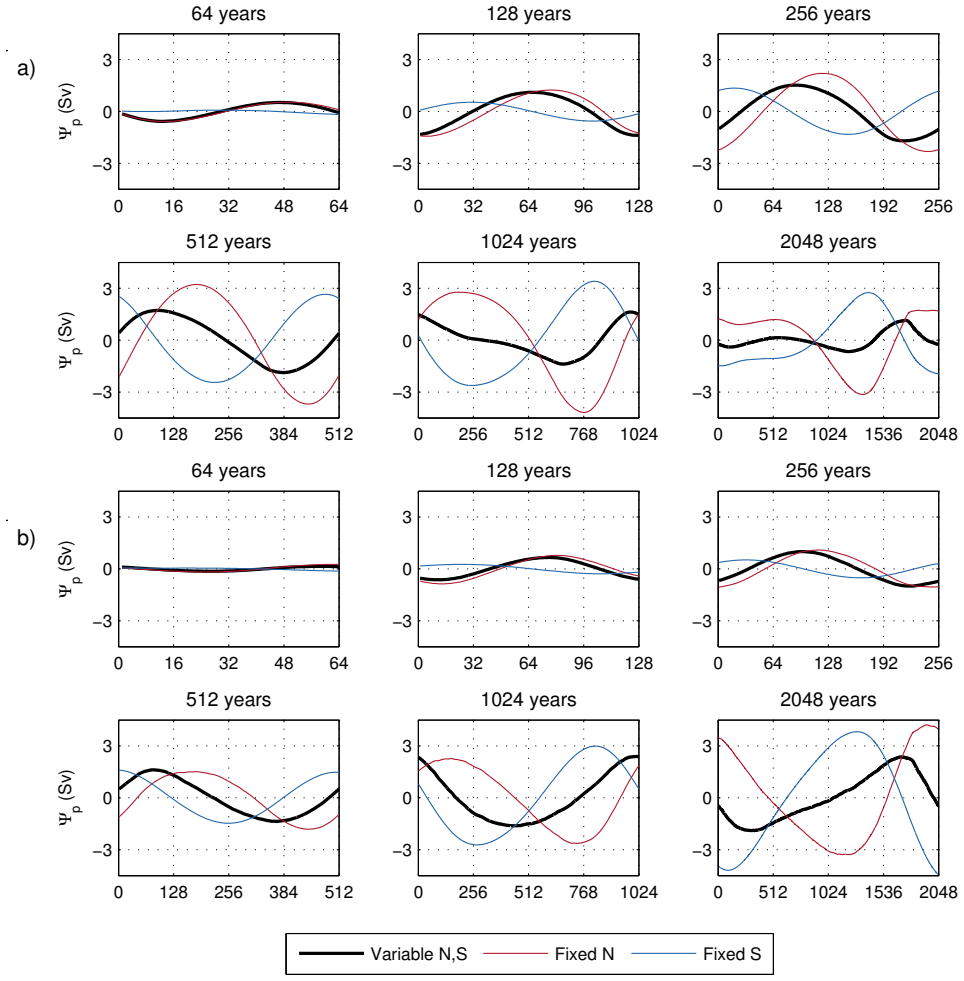

Figure 3.17: Temporal anomalies of scaled Indo-Pacific overturning, Ψ_p, at a) 1000m (10°S) (inferred from a meridional density gradient between the northern Pacific Ocean boundary and the southern Indian Ocean boundary) and b) 4000m (10°S) (inferred from a meridional density gradient calculated across the Pacific Ocean only). Ψ_p anomalies are constructed using 1) both a variable northern and southern boundary (bold black), 2) a fixed northern boundary corresponding to the temporal mean profile of ρ_N (red) and 3) a fixed southern boundary corresponding to the temporal mean profile of ρ_S (blue)

insufficient.

The results here demonstrate that the scaling law does hold in the Indo-Pacific basin and supports the notion that this is a general physical principle that holds throughout the global ocean and not simply a coincidence of Atlantic overturning. In doing so, however, we have also highlighted the topographic difficulties in applying such a scaling law to the Indo-Pacific basin under realistic geometric configurations.

3.6 Discussion and conclusions

In this study, we have presented a scaling for meridional overturning in terms of twice-integrated meridional density gradients, constructed from meridional pressure gradient anomalies and the hydrostatic relationship. We have demonstrated its predictive ability in the upper Atlantic Ocean across a broad range of timescales under deterministic buoyancy forcing scenarios and in response to stochastic atmospheric variability in global ocean models using realistic bathymetry. Furthermore, this scaling retains depth dependence, allowing both the upper and abyssal ocean overturning to be predicted in the same basin. Nonlinear elements of the overturning response to simple, periodic buoyancy forcing in a coarse resolution model are well predicted by Ψ_p, including the resonant timescale of upper Atlantic overturning at 1000m and the biharmonic response of abyssal Atlantic overturning at 4000m. In a higher resolution 0.5° stochastically forced simulation, both the pacing and magnitude of overturning variability at multi-decadal (and longer) timescales is accurately modelled with correlations greater than or equal to 0.8 observed at multi-decadal timescales and correlations greater than 0.9 observed at centennial timescales.

The timescale at which the derived relationship between meridional overturning and twice-integrated meridional density gradients is physically justified is determined by the timescale at which the governing assumption of a linearly proportional relationship between basin-scale zonal and meridional pressure gradients holds. In

principle, buoyancy anomalies can propagate around a basin boundary (via Kelvin waves) in a matter of months (Johnson and Marshall, 2002). However, basin-scale interior adjustment is determined by the propagation of Rossby waves from the eastern boundary (taking place over a number of years) and advective processes acting on decadal timescales. Consequently, we see weak predictive ability of the inferred overturning streamfunction at sub-decadal 8 year timescales. However, this scaling becomes a very good predictor of meridional overturning variability at multi-decadal through millennial timescales. The shorter timescales in this spectral band are directly relevant to contemporary climate change discussions.

It should be noted at this point that, since ORCA2 is a coarse resolution model, high-frequency Kelvin waves are unlikely to well-represented in our simulations. This does not preclude the possibility of boundary anomaly propagation in a manner similar to that described in Johnson and Marshall (2002), but the associated timescales may differ. Indeed, the fast, equatorward propagation of circulation anomalies along the western boundary has been observed in many ocean modelling studies (Marshall and Johnson (2013) and references therein), including the coarse resolution oceanic component of the coupled climate model HadCM3 (Dong and Sutton, 2002). Whilst the precise method of anomaly propagation throughout the Atlantic (and, indeed, the global ocean) in our experiments is not investigated here, we do note that there are consistencies with the wave propagation theories set out by Johnson and Marshall (2002) and Johnson and Marshall (2004) (amongst others). For instance, the 'equatorial buffer' is observed in the Atlantic (Johnson and Marshall, 2002) and the fraction of variability reaching the Indo-Pacific basin is well-predicted by the theory of Johnson and Marshall (2004).

It has previously been argued by de Boer et al. (2010) that meridional density gradients do not inevitably correlate well with meridional overturning. It is important to stress that our results are not in conflict with these findings. This paper attempts to reconcile the issues raised therein, arguing here that meridional overturning is well predicted by meridional pressure gradients that can then be expressed in terms of integrated meridional density gradients via the hydrostatic

relationship. Indeed, when de Boer et al. (2010) use a $\Psi \sim \Delta\rho_y H^2$ scaling relationship with the scale depth, H, determined by the depth at which the north-south pressure gradient anomaly is zero (the implicit solution of $V(H) = 0$ in the framework presented here) then a reasonable prediction of Atlantic overturning strength is obtained. It should also be emphasised here that the focus of our study is on the predictability of overturning variability using twice-integrated meridional density gradients, not on the causes or drivers of overturning variability. However, whilst we do not seek to demonstrate here whether meridional pressure gradients do or do not drive changes in meridional overturning, we do observe that Ψ_p precedes Ψ in the Atlantic Ocean at 1000m (by approximately 4 years).

One of the suggested explanations in de Boer et al. (2010) for why meridional density gradients failed to explain changes in meridional overturning in their experiments was because their experimental setup was strongly influenced by remote forcing (e.g. Southern Ocean winds and Antarctic Bottom Water formation). Although our deterministic experimental setup is focussed on directly forced, high-latitude variability in the Atlantic Ocean, we have demonstrated that remote changes in density at the southern boundary do make an important contribution to the overturning scale at the longest timescales and the accuracy of the scaling law is maintained. Indeed, southern boundary variability is critical to the maintenance of this accuracy, particularly in the abyssal ocean.

We conclude by observing that the scaling relationship proposed here has obvious applicability at centennial and millennial timescales in paleoclimate modeling studies, particularly in the Atlantic Ocean. This relationship has also been verified at far shorter timescales. In principle, our results suggest that multi-decadal variability in real ocean Atlantic overturning could be reconstructed in much the same way, only requiring knowledge of the vertical density profile at the northern and southern boundaries.

Chapter 4

Available potential energy generation: understanding AMOC variability and the 'bipolar seesaw'

4.1 Introduction

In Chapter 3, we conducted a series of transient experiments in which the global ORCA2 configuration of the NEMO ocean model (Madec, 2008) was forced with periodic, sinusoidal air temperature perturbations over the North Atlantic. These forcing scenarios induced large magnitude oscillations in global ocean overturning that varied in both amplitude and structure with forcing period. This variability was well predicted by a scaling relationship that reconstructed a depth-dependent overturning streamfunction from twice-integrated, basin-scale meridional density gradients. The sensitivity of the meridional overturning circulation (MOC) to high-latitude surface buoyancy forcing is well known, particularly in the North Atlantic (e.g. Stouffer et al. (2006)). Nevertheless, traditional energetics arguments suggest that the energetic effect of these fluxes is too small to be considered

a mechanical driver of the MOC (e.g. Wunsch and Ferrari (2004); Kuhlbrodt et al. (2007)). It remains unclear, therefore, how such variations in surface buoyancy forcing can have such a large impact on ocean circulation without altering the supply of mechanical energy.

In Chapter 2, we provided evidence (using a coupled climate model) that surface buoyancy forcing is actually a leading order source of mechanical energy in the ocean when considered within the available gravitational potential energy (AGPE) framework. This fact has only recently been realised at steady-state (e.g. Hughes et al. (2009); Tailleux (2009)) and the application of these concepts to transient ocean simulations has, thus far, been limited to idealised ocean models with simplified bathymetry and a linear equation of state (e.g. Hogg et al. (2013); Dijkstra et al. (2014)). Despite this, it has already been shown that globally integrated energy budgets are not necessarily very informative about local changes in circulation occurring during transient ocean simulations (Gregory and Tailleux, 2011; Hogg et al., 2013). Hogg et al. (2013) applied freshwater perturbations to an idealised ocean model (with a rectilinear basin and a linear equation of state), finding scenarios in which both global KE and AGPE increased, but the strength of the Atlantic MOC (AMOC) decreased. However, regional energetics analyses can be more explanatory. Hogg et al. (2013) found a good correlation between instantaneous North Atlantic AGPE input integrated north of 40°N and changes in the AMOC instigated by a series of 400 year freshwater perturbation experiments. This broad correlation also extended to the directly-forced Southern Ocean, linking regional AGPE content and lower cell overturning, supporting the idea that changes in global overturning can be energetically linked to changes in surface buoyancy forcing.

The relationship between the generation of AGPE by surface buoyancy forcing and changes in large-scale ocean circulation (as encapsulated by large-scale kinetic energy, KE) can be elucidated by considering the regional conversion of AGPE to KE. In order for an increase in AGPE generation to translate into an increase in overturning, a portion of this AGPE must be converted to large-scale KE. In a Boussinesq ocean model, this conversion occurs through the work done by the

horizontal pressure gradient on the circulation or, conversely, through the work of the circulation against the horizontal pressure gradient (Gregory and Tailleux, 2011). Gregory and Tailleux (2011) argue that this term is the most important in the KE budget and that, locally, its sign is critical, distinguishing between areas of directly wind-driven flow and regions in which the flow is being energised by the AGPE reservoir. They found that this conversion was negative in the global integral (implying net conversion from large-scale KE to AGPE), but locally positive in regions of deepwater formation and within western boundary currents. Within the Atlantic, the concentration of the conversion from AGPE (much of which is supplied diabatically by surface buoyancy fluxes, Chapter 2) to KE in these regions strongly imply that the AGPE reservoir is supplying energy to the AMOC (Gregory and Tailleux, 2011). If there is a reduction in the energy supplied locally by the AGPE reservoir then local KE dissipation will be reduced to maintain a local KE balance. Gregory and Tailleux (2011) hypothesised that this reduction will entail some form of weakening in the circulation. To test this hypothesis, they correlated the simulated decline in AMOC intensity in a transient CO_2-forced climate change simulation with the reduction in conversion from AGPE to KE (integrated between 50°N and 70°N). This decline was largest in the overflow regions in which the AMOC descends the Greenland-Scotland ridge (see Figure 7a in Gregory and Tailleux (2011)). This correlation was also found to hold well in nine CMIP3 coupled climate models (Gregory and Tailleux, 2011) and has also be shown to hold during AMOC recovery in a climatic perturbation experiment in CanESM2 (Saenko, 2013).

Dijkstra et al. (2014) combined both of these ideas in a minimal model of AMOC multi-decadal variability, determining the energetics underlying the internal dynamics. The multi-decadal variability in this model arises due to the internal propagation of temperature anomalies by a thermal Rossby mode. This propagation creates temporal changes in AGPE content that are then converted into the KE associated with multi-decadal AMOC variability.

Whilst previous global modelling studies have focussed on the relationship between

the AMOC and the AGPE to KE conversion taking place at high northern latitudes (Gregory and Tailleux, 2011; Saenko, 2013), little emphasis has been placed on those occurring along the western boundary. Sijp et al. (2012) developed an analytical description of the western boundary velocity within the deep return limb of the AMOC as a function of the interface separating Antarctic Intermediate Water (AAIW) and North Atlantic Deep Water (NADW). An energetics analysis of this simple model revealed that the deep return limb of the AMOC consumes potential energy at a rate determined by the meridional gradient of this interface along the western boundary. This supports the principles of our scaling relationship developed in Chapter 3, in which we found that the western boundary was critical to successfully scaling meridional overturning using meridional density gradients. However, a study of AMOC variability and the energetics of the western boundary has yet to be carried out in a general circulation model.

In this study, we will apply similar techniques to the suite of periodically forced ocean simulations described in Chapter 3, exploring the response of both the upper and lower cells of the global meridional overturning circulation to variable buoyancy forcing, with particular focus on multi-decadal through millennial timescales. In Chapter 3, we showed that the simulated MOC exhibited different responses to different timescales of forcing, despite the amplitude of the atmospheric perturbation remaining the same for each timescale. In particular, we observed a centennial resonant timescale in the Atlantic MOC. In this chapter, we will seek to explain this behaviour by quantifying the transient energetic diagnostics associated with each forcing scenario. In Section 4.2, we describe our methods for calculating transient energetic diagnostics and evaluate their steady-state distribution in the ORCA2 control simulation. In Section 4.3, we diagnose the AGPE power input by surface buoyancy forcing during each forcing scenario and relate the amplitude of these oscillations to the amplitude of the AMOC response. We will elucidate this link by examining the local energy conversion from AGPE to KE occurring in the North Atlantic deepwater formation/overflow regions and along the western boundary. In Section 4.4, we expand the focus of this study to the Southern Ocean, exploring the effect that remote buoyancy forcing in the North Atlantic has

on lower cell overturning through changes in global stratification. We conclude by providing a novel interpretation of the 'bipolar see-saw' observed between upper and lower cell overturning at millennial timescales, suggesting that it is directly forced by local changes in AGPE generation in the Southern Ocean that occur in response to changes in global stratification.

4.2 Energetics diagnostics: the control simulation

In this section, we will describe the AGPE power input by surface buoyancy forcing and the distribution of the AGPE/KE conversion in the ORCA2 control simulation. The model was spun up from rest and forced with CORE v2.0 normal year forcing (Large and Yeager, 2008) repeated annually for 2000 years until an equilibrium in global meridional overturning was reached. This control simulation is described in more detail in Section 3.2.

4.2.1 Power input by surface buoyancy forcing

4.2.1.1 Method

The power input by surface buoyancy fluxes is calculated using the AGPE framework developed in Chapter 2. The globally integrated AGPE generation by surface buoyancy fluxes is given by:

$$\mathrm{G} = \int \mathrm{g} \left(\mathrm{z} \frac{\partial \rho}{\partial \mathrm{t}}_{\mathrm{BUOY}} - \mathrm{z}_{\mathrm{ref}} \frac{\partial \rho_{\mathrm{ref}}}{\partial \mathrm{t}}_{\mathrm{BUOY}} \right) \mathrm{dV}. \tag{4.1}$$

where ρ = density, ρ_{ref} = reference state density, z = vertical displacement, and z_{ref} = vertical displacement in the reference state of minimum GPE, and g = the gravitational constant. As in Section 2.2, z and z_{ref} are defined relative to the surface and the GPE reference state profile is determined via the adiabatic sorting

method of Huang (2005). We define G^{A} to be the areal concentration of G, such that $\mathrm{G} = \int \mathrm{G}^{\mathrm{A}} \, \mathrm{d}A$.

Density, ρ, is a function of potential temperature θ, salinity S, and pressure p. In a Eulerian framework, the time derivative of ρ is given by:

$$\frac{1}{\rho_0}\frac{\partial \rho}{\partial t}_{\,\mathrm{BUOY}} := -\alpha \frac{\partial \theta}{\partial t}_{\,\mathrm{BUOY}} + \beta \frac{\partial S}{\partial t}_{\,\mathrm{BUOY}} \tag{4.2}$$

$$\alpha := -\left.\frac{1}{\rho_0}\frac{\partial \rho}{\partial \theta}\right|_{p=p(z)}, \quad \beta := \left.\frac{1}{\rho_0}\frac{\partial \rho}{\partial S}\right|_{p=p(z)} \tag{4.3}$$

where α is the thermal expansion coefficient and β is the haline contraction coefficient. The time derivative of ρ_{ref} is calculated analogously, with α and β evaluated at reference state pressure, as opposed to in situ pressure.

The local salinity (S) tendency due to surface buoyancy fluxes is given by:

$$\frac{\partial S}{\partial t}_{\,\mathrm{BUOY}} = \frac{emp_S \, S}{\rho_0 \Delta z_1} \qquad k = 1 \tag{4.4}$$

where emp_S quantifies the concentration/dilution effect of virtual mass fluxes of salt through the surface and the freezing/melting of sea ice. The local potential temperature (θ) tendency due to surface buoyancy forcing is decomposed into contributions from non-penetrative (Q_{ns}) and penetrative (Q_{sr}) heat fluxes, such that:

$$\frac{\partial \theta}{\partial t}_{\,\mathrm{BUOY}} = \frac{\partial \theta}{\partial t}_{\,Q_{ns}} + \frac{\partial \theta}{\partial t}_{\,Q_{sr}} \tag{4.5}$$

These contributions can then be expressed as:

$$\frac{\partial \theta}{\partial t}_{\,\mathrm{Q_{ns}}} = \frac{Q_{ns}}{\rho_0 C_p \Delta z_1} \qquad k = 1 \tag{4.6}$$

$$\frac{\partial \theta}{\partial t}_{\,\mathrm{Q_{sr}}} = \frac{Q_{sr}}{\rho_0 C_p \Delta z_k}\frac{\partial I}{\partial k} \qquad k \geq 1 \tag{4.7}$$

where ρ_0 = reference value of density, C_p = specific heat capacity of seawater, k = model layer (numbered from the surface), and Δz_k = the thickness of the k-th model layer. I is a non-dimensional function describing the penetration of light through the water column (Madec, 2008). The variations in surface buoyancy flux induced by the periodic atmospheric air temperature perturbations over the North Atlantic are, predominantly, encapsulated in Q_{ns} (the sum of the sensible, latent and long wave radiative heat fluxes). The bulk formulae by which surface buoyancy fluxes are computed from the prescribed atmospheric forcing fields are described in Large and Yeager (2008). Further details regarding the implementation of surface boundary conditions in NEMO can be found in Section 7 of Madec (2008).

4.2.1.2 AGPE generation in the control simulation

Globally integrated, the AGPE power input by surface buoyancy fluxes in the ORCA2 control simulation is +1.12 TW. This is comparable with the 1 TW estimate of the mechanical energy input into the ocean by winds (Wunsch, 1998). Since z is small near the surface, G^{A} is largest where the reference level, z_{ref}, is deepest. The correspondence between the surface layer reference state displacement (Figure 4.1) and AGPE generation (Figure 4.2) is clear. At low-latitudes, G^{A} is small. This is because the low-latitude ocean is capped by a buoyant surface layer that is also positioned near the surface of the GPE reference state. However, it is possible to find very dense water masses at the surface at high-latitudes, particularly in regions of deepwater formation in the North Atlantic and in the Weddell and Ross Seas. These dense water masses are situated much deeper in the global reference state (such that $z - z_{\mathrm{ref}} > 0$) (Figure 4.1). Therefore, variations in surface buoyancy fluxes in the deepwater formation zones can have a large impact on the global mechanical energy budget. This is consistent with the sensitivity of global ocean circulation to perturbations in these regions seen in a multitude of modelling studies (e.g. Stouffer et al. (2006); Hogg et al. (2013)). Since the net effect of surface buoyancy forcing at high-latitudes is to make the ocean denser (i.e. $\partial\rho/\partial t > 0$), the AGPE tendency associated with high-latitude buoyancy forcing is both large and positive. In short, AGPE is generated in regions in which surface

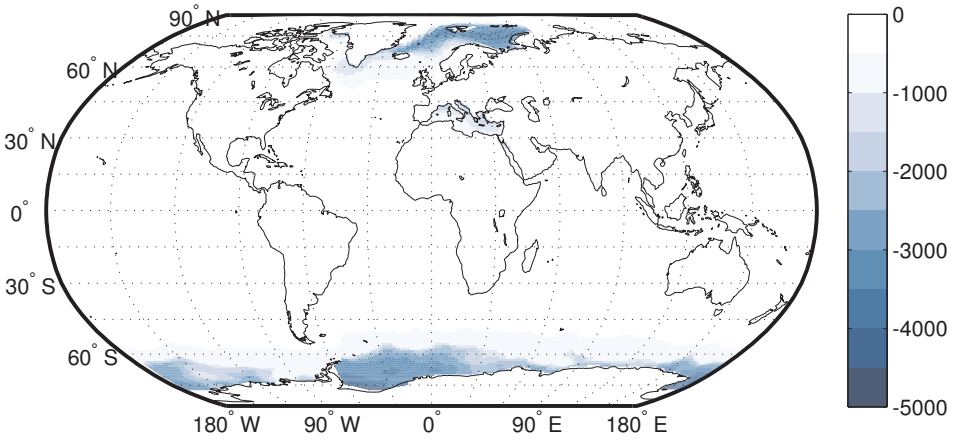

Figure 4.1: The reference state displacement, z_{ref}, of the surface layer in the ORCA2 control simulation (units: m).

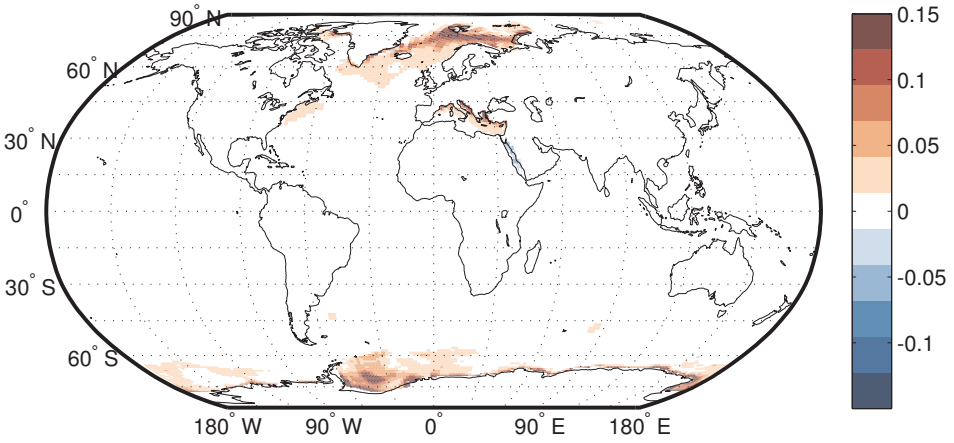

Figure 4.2: The global distribution of G^A in the ORCA2 control simulation, the local generation of AGPE by surface buoyancy forcing (units: W m^{-2}).

buoyancy forcing is making already dense surface water denser. The greatest regional contributions come from the Southern Ocean (+0.51 TW) and the Atlantic Ocean (+0.41 TW), providing 46% and 36% of the global AGPE source respectively. Conversely, the mechanical energy generated by surface buoyancy forcing in the North Pacific is just +0.06 TW. This is consistent with the lack of deepwater formation and high-latitude overturning found in the Pacific basin.

The value of G in ORCA2 compares well with that of HadCM3 (+0.72 TW, Chapter 2). However, it is somewhat larger. This is likely due to the high salinity (and, therefore, density) of the Mediterranean simulated in HadCM3 (in comparison to observations and other AOGCMs (Marcos and Tsimplis, 2008)).

Consequently, the Mediterranean is deeper in the reference state than any other water mass in HadCM3, which reduces the AGPE generation at high-latitudes (cf. Figure 2.4 and Figure 4.1).

4.2.2 Conversion from AGPE to KE

4.2.2.1 Method

The rate at which KE is supplied by the pressure gradient force is given by:

$$B = -\int \mathbf{u_h} \cdot \nabla_h p \, \mathrm{d}V \tag{4.8}$$

in which $\mathbf{u_h}$ is the horizontal velocity vector and $\nabla_h p$ is the horizontal pressure gradient. This term is typically thought of as the conversion from potential energy to KE energy in a hydrostatic Boussinesq model (e.g. Hughes et al. (2009); Gregory and Tailleux (2011); Saenko (2013); Tailleux (2013a)). The conversion between KE and GPE can be derived in the global integral by rewriting (4.8) as:

$$B = -\int \left(\mathbf{u} \cdot \nabla p - w \frac{\partial p}{\partial z} \right) \mathrm{d}V. \tag{4.9}$$

By using vector algebra and the divergence theorem, it can be shown that the first term is equal to:

$$\int \mathbf{u} \cdot \nabla p \, \mathrm{d}V = \oint p \mathbf{u} \cdot \mathbf{n} \, \mathrm{d}S - \int p \nabla \cdot \mathbf{u} \, \mathrm{d}V \tag{4.10}$$

where V is the ocean volume, S is the ocean boundary surface, and $\mathbf{n}$ is the outward pointing vector normal to this surface. The surface integral disappears under the assumption of no normal flow at the boundary ($\mathbf{u} \cdot \mathbf{n} = 0$ on S) and the volume integral disappears under the assumption of incompressibility ($\nabla \cdot \mathbf{u} = 0$ in V). Therefore, $\int \mathbf{u} \cdot \nabla p \, \mathrm{d}V = 0$. The second term of (4.9) can then be re-expressed

using the hydrostatic appoximation ($\partial p/\partial z = -\rho g$) to give:

$$B = -\int \rho g w \, \mathrm{d}V \tag{4.11}$$

Thus, $-B$ is often regarded as the GPE ($\int \rho g z \, \mathrm{d}V$) tendency due to the resolved circulation and, thus, B is regarded as the conversion from GPE to resolved KE (Toggweiler and Samuels, 1998; Huang, 1999; Hughes et al., 2009; Gregory and Tailleux, 2011; Hogg et al., 2013; Dijkstra et al., 2014). Since advection is considered an adiabatic process, B can also be regarded as the tendency in AGPE (Chapter 2). This supposition is supported, to first order, in the globally integrated HadCM3 KE and (A)GPE budgets. A net conversion rate of +0.49 TW (given by -B) between resolved KE and (A)GPE is implied by the globally integrated KE budget (Gregory and Tailleux, 2011). Correspondingly, the net change in GPE due to the resolved circulation is equal to +0.57 TW (AGPE: +0.59 TW) (Table 2.1). In the absence of numerical leakage and nonlinearities in the equation of state, these terms should be identical. However, when implemented in general circulation models, numerical advection schemes are not purely adiabatic and can result in the spurious mixing of water masses (Griffies et al., 2000). The reader is encouraged to refer to Chapter 2 for further discussion of the effect of numerical leakage and nonlinearities in the equation of state on global (A)GPE budgets.

Since B is a conversion between energy reservoirs, it can be analysed either from the perspective of the global KE framework (the work of the pressure-gradient force) or from the perspective of the global (A)GPE framework (the work of the resolved circulation). Locally, however, the GPE tendency due to advection (neglecting numerical leakage and the variable compressibility of seawater) is well-approximated by:

$$\frac{\partial \mathrm{GPE}}{\partial \mathrm{t}}_{\mathrm{ADV}} \approx \int -\nabla \cdot (\rho g z \mathbf{u}) + \rho \mathrm{g} w \, \mathrm{dV} \tag{4.12}$$

Therefore, this term includes the divergence of GPE transport in addition to the local conversion between KE and GPE. Whilst the transport divergence term integrates globally to zero, it can be locally large and noisy. Consequently, an

analysis of the local tendency from the perspective of the (A)GPE budget is unfeasible. Therefore, we diagnose the local AGPE to KE conversion directly from the KE budget (Tailleux, 2013a), defining B^A to be the areal concentration of B (such that $B^A = -\int \mathbf{u_h} \cdot \nabla_h p \, \mathrm{d}z$). Unlike sources and sinks of AGPE, we can easily calculate $\mathbf{u_h} \cdot \nabla_h p$ online to avoid errors associated with temporal averaging. Note that B^A is necessarily zero for geostrophic flow. Therefore, it is only the small ageostrophic components of velocity that are responsible for the conversion between AGPE and KE (and vice versa).

Unlike in the atmosphere, the conversion between AGPE and KE is able to take either sign in the ocean, because AGPE can also be generated adiabatically (through wind-driven upwelling) as well as diabatically (by surface buoyancy fluxes) (Tailleux, 2013a). $B > 0$ implies conversion of AGPE to KE, whilst $B < 0$ implies adiabatic generation of AGPE at the expense of KE (i.e. conversion from KE to AGPE). Globally integrated, B has been shown to be negative in HadCM3 (and other non-eddy resolving ocean models) (Gregory and Tailleux, 2011), thus implying net conversion from large-scale KE to AGPE. Although we found that the resolved circulation was a source of AGPE in our analysis of HadCM3, this interpretation is incomplete as it does not include the effects of unresolved, mesoscale advection. When the effect of unresolved advection is accounted for (through the parameterisation of mesoscale eddies), the net conversion is, in fact, implied to be from AGPE to KE (i.e. $B > 0$) (see Section 2.4). This is consistent with the value of B found in the idealised eddy-resolving configuration of Saenz et al. (2012).

4.2.2.2 AGPE/KE conversion in the control simulation

In the global integral, $B = -0.41$ TW in ORCA2. This is similar to $B = -0.49$ TW in HadCM3 (Gregory and Tailleux, 2011) and $B = -0.54$ TW in CanESM2 (Saenko, 2013). However, B^A can be positive locally. It has been proposed that a regional analysis of B^A can be used to distinguish between areas in which the flow is primarily directly wind-driven and areas in which the flow is being energised

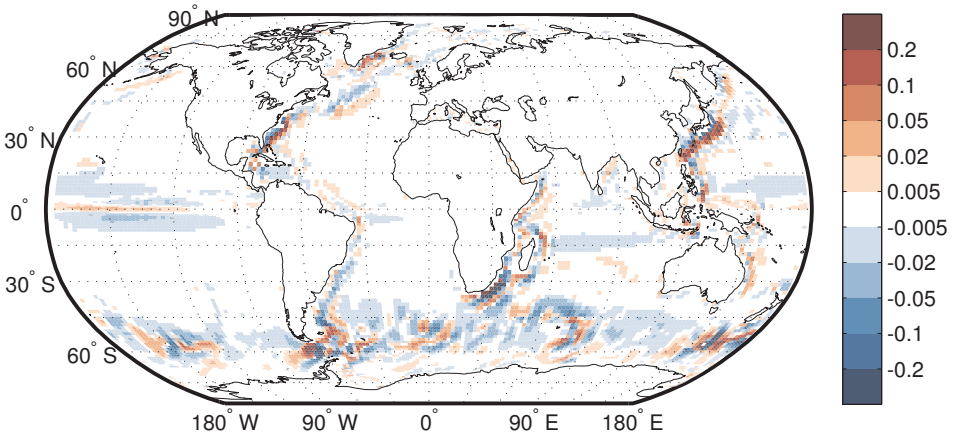

Figure 4.3: The global distribution of B^A in the ORCA2 control simulation, the local conversion from AGPE to KE (units: W m^{-2}). Note: a nonlinear colour scale is used in this figure.

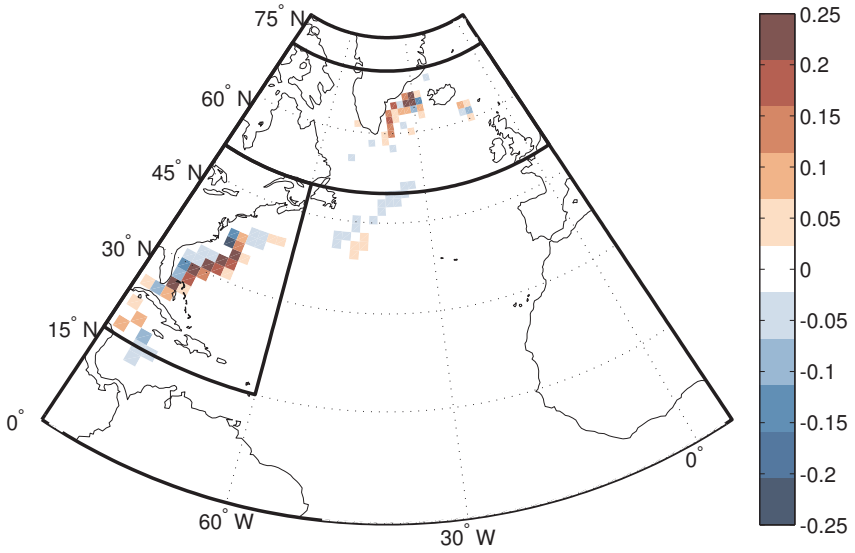

Figure 4.4: Distribution of B^A in the North Atlantic (units: W m^{-2}). The boxes depict the regions of integration for the western boundary and the high-latitude box between 50°N-70°N.

at the expense of AGPE (Tailleux, 2013a). Such an approach was first utilised by Gregory and Tailleux (2011) and, subsequently, by Saenko (2013). The global distribution of B^A is illustrated in Figure 4.3.

The global integral is dominated by the large negative integrated contribution from the Southern Ocean (-0.43 TW) in which Ekman transport and wind-driven upwelling against the horizontal pressure gradient (raising dense fluid parcels and pushing down light fluid parcels) adiabatically generates AGPE at the expense of KE. However, integrated over the Atlantic basin alone (extending to 30°S),

B is positive (ORCA2: +42 GW; HadCM3: +43 GW (Gregory and Tailleux, 2011)). Positive contributions come from the deepwater formation/overflow regions between 50°N and 70°N (+26 GW) and the western boundary (+64 GW) (as depicted in Figure 4.4), with opposing negative contribution arising elsewhere, particularly in the North Atlantic drift. Whilst western boundary currents globally (e.g., the Kuroshio current in the North Pacific) are typically positive, a regional integral over the Agulhas (in the southwest Indian Ocean) is negative. In general, B^A is somewhat noisier close to topography in regions bordering the dynamic Southern Ocean and the Antarctic Circumpolar Current (ACC), such as the Drake Passage and near the Agulhas. A full understanding of this effect is beyond the scope of this study.

The size and location of the high-latitude box spanning 50°N to 70°N has been chosen to be consistent with Gregory and Tailleux (2011), who determined that this region maximised the correlation between zonally integrated B^A and the AMOC response across a multi-model ensemble of CO_2-forced experiments. This region also spans the latitude of largest amplitude forcing in our suite of transient, periodically forced experiments.

4.3 The energetics of the upper MOC cell response

In our experimental setup, the upper cell is directly forced by periodic changes in atmospheric air temperature over the North Atlantic. The period of oscillation is increased incrementally from multi-annual to millennial timescales, but the amplitude of the forcing cycle remains constant. As described in Chapter 3, the strength of meridional overturning (measured at 1000m, 35°N) undergoes oscillations in response to these perturbations and the magnitude of the response varies with forcing period, peaking in amplitude at 128 year timescales (see Chapter 3).

4.3.1 AGPE power input

We begin our analysis of the upper cell response to periodic surface buoyancy forcing by diagnosing the transient high-latitude AGPE generation by surface buoyancy forcing in the Atlantic (integrated between 50°N and 70°N) associated with each forcing cycle. The reference state computation (using a nonlinear equation of state) is complicated and expensive, which prohibits the online calculation of AGPE tendencies. Instead, we must calculate them offline using temporally averaged data. However, due to data storage and computational constraints, we are restricted to the use of annually averaged data at multi-centennial and millennial timescales. The subsequent lack of seasonality in the reference state results in an underestimation of winter AGPE generation at high-latitudes. For example, the AGPE generated by surface buoyancy forcing in the control simulation is reduced to +0.43 TW when calculated using annually averaged model output (cf. +1.12 TW when calculated using monthly averaged model output, Section 4.2.1).

However, we are interested in capturing the characteristics of longer period variability induced by the periodic forcing, as opposed to resolving sub-annual features of AGPE generation. Figure 4.5 plots the AGPE source term in the North Atlantic calculated using both monthly and annually averaged model output for forcing periods $P = 8, 16, 32, 64, 128$, and 256 years (with an equivalent plot for the Southern Ocean given in Section 4.4.5, Figure 4.18). Whilst the magnitude of the mean power input is larger when calculated using monthly averaged data (by a scale factor of approximately 2.2), the pattern of variability is broadly coherent, being well correlated at all timescales and with the range of each signal converging towards a consistent ratio by multi-decadal timescales (between the monthly and annually generated signals). It is noted that the amplitude of variability in AGPE generation is overestimated at 8 year timescales, but this is likely to be a result of using annually averaged data to sample a sub-decadal forcing cycle. However, since the focus of this study is on the centennial resonant timescale, we do not consider that the use of annually averaged data will have a detrimental impact on our results or discussion. For consistency across multi-decadal through millennial

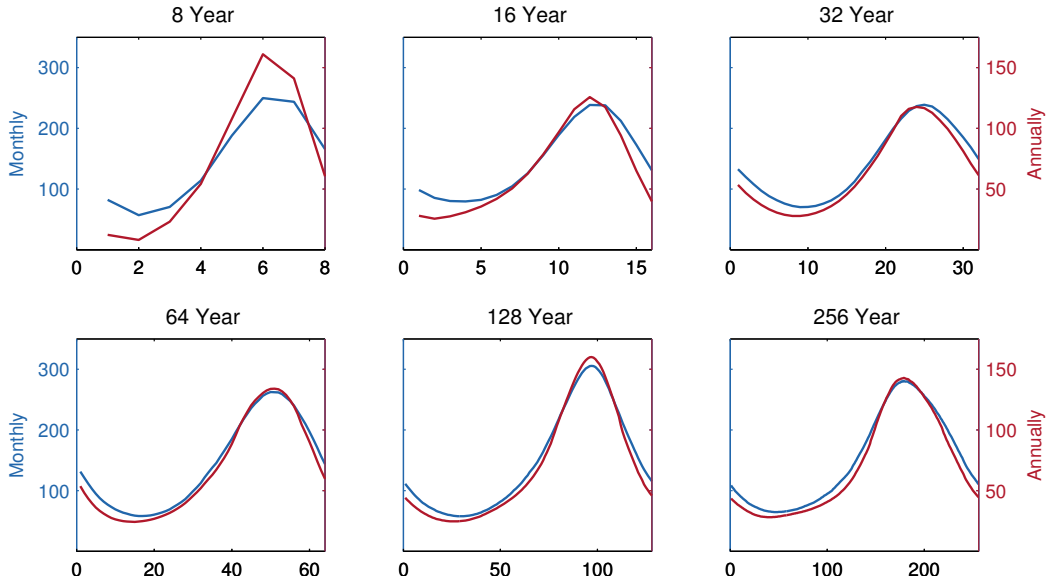

Figure 4.5: G^A, integrated between 50°N and 70°N in the North Atlantic, calculated using both monthly (blue) and annually (red) averaged model output (units: 1 GW = 10^9 W).

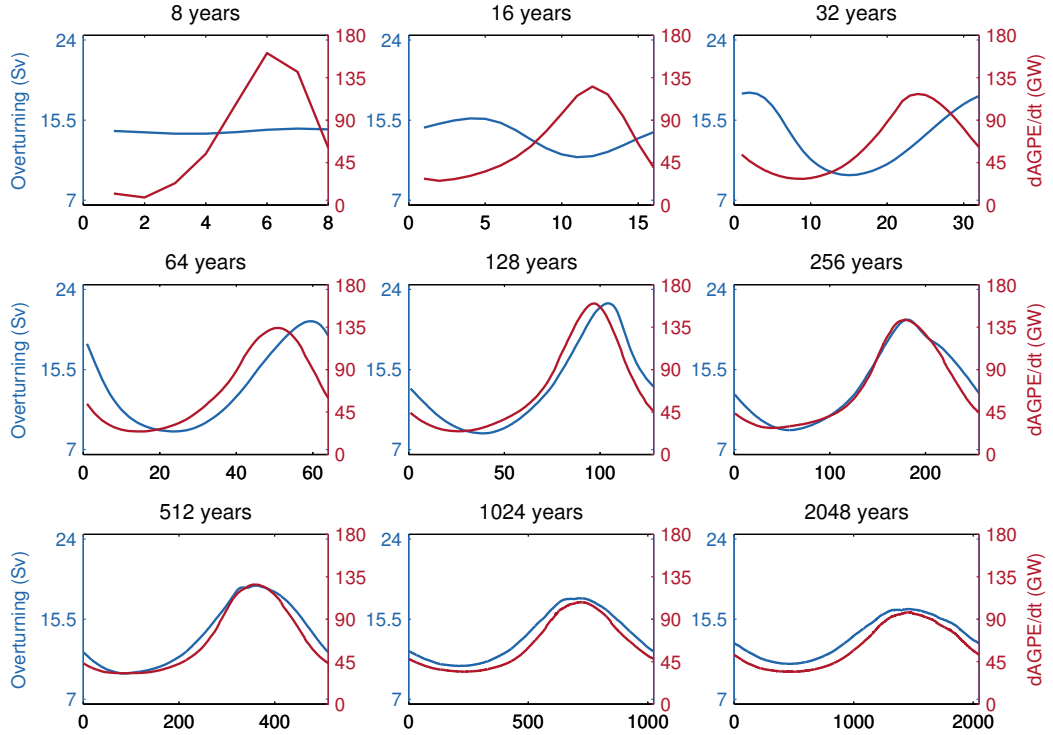

Figure 4.6: Timeseries of the AMOC response at 1000m, 35°N (blue) and G^A integrated between 50°N and 70°N (red, units: 1 GW = 10^9 W, calculated using annually averaged model output).

timescales, we will use only annually averaged data in the following analysis. Since it is not central to this chapter, we will exclude the 8 year forcing timescale (for which the error arising from the use of annually averaged data is largest) from the following discussion of the power input by transient surface buoyancy fluxes.

Despite the amplitude of the sinusoidal air temperature perturbations being held constant for each forcing period, it is apparent that there are large, frequency-dependent variations in AGPE generation with timescale (Figure 4.6). Moreover, the amplitude of these oscillations in AGPE generation are predictive of the amplitude of the response in the upper overturning cell at multi-decadal (and longer) timescales (Figure 4.7). This strongly implies that the magnitude of the AMOC response is determined by the magnitude of the AGPE power source.

The variability in AGPE generation is overwhelmingly dominated by the induced variability in the GPE of the reference state. Variability in the GPE of the surface layer in the physical state, for which z is small, makes a negligible contribution to the overall sum. The tendency in reference state GPE due to surface buoyancy forcing is given by $-g\frac{\partial \rho_{\mathrm{ref}}}{\partial t}_{\mathrm{BUOY}} z_{\mathrm{ref}}$ (see Equation 4.1). We can quantify the separate contributions of each term to the overall variability in AGPE generation by decomposing each term of this product (say, $x(t)$) into the sum of its temporally constant control value, x_{con}, and a temporally variable perturbation, $x'(t)$, defined such that $x(t) = x_{con} + x'(t)$. In this manner, $-g\frac{\partial \rho_{\mathrm{ref}}}{\partial t}_{\mathrm{BUOY}} z_{\mathrm{ref}}$ can be expressed as:

$$ab = a_{con}b_{con} + a_{con}b' + a'b_{con} + a'b' \tag{4.13}$$

in which $a := g\frac{\partial \rho_{\mathrm{ref}}}{\partial t}_{\mathrm{BUOY}}$ (the reference state density tendency) and $b := -z_{\mathrm{ref}}$ (the reference *depth*). $a_{con}b'$ quantifies the contribution of variability in the reference depth, $a'b_{con}$ quantifies the contribution of variability in the density tendency, and $a'b'$ quantifies the contribution of covariations in these two terms to overall variability in the reference state GPE tendency.

Each of the terms in this decomposition are plotted for all forcing cycles in Figure 4.8. It is clear that variability in both the density tendency and reference depth play an important role in the variability of G^{A} in the North Atlantic. The

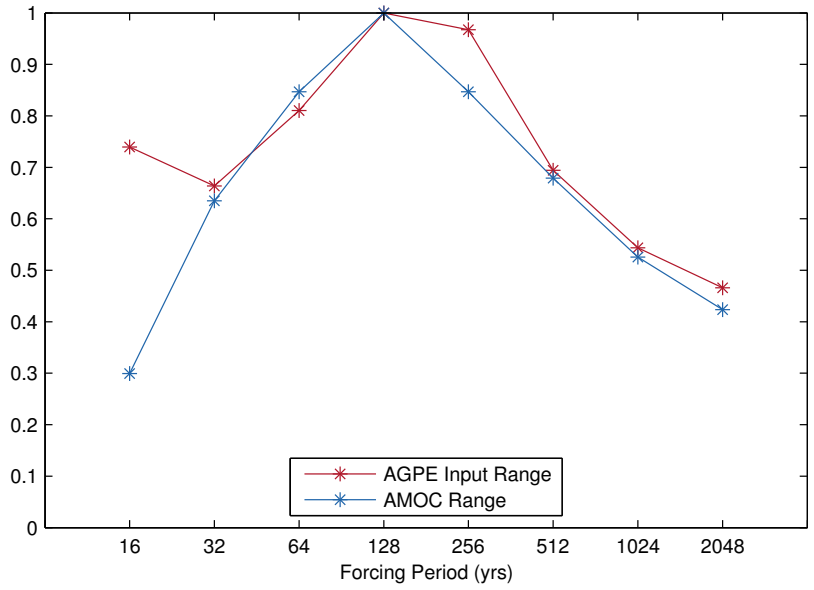

Figure 4.7: Range of the AMOC response at 1000m, 35°N (blue) and range of G^A integrated between 50°N and 70°N (red, calculated using annually averaged model output), with both signals normalised by their respective (maximum) range at the 128 year forcing period.

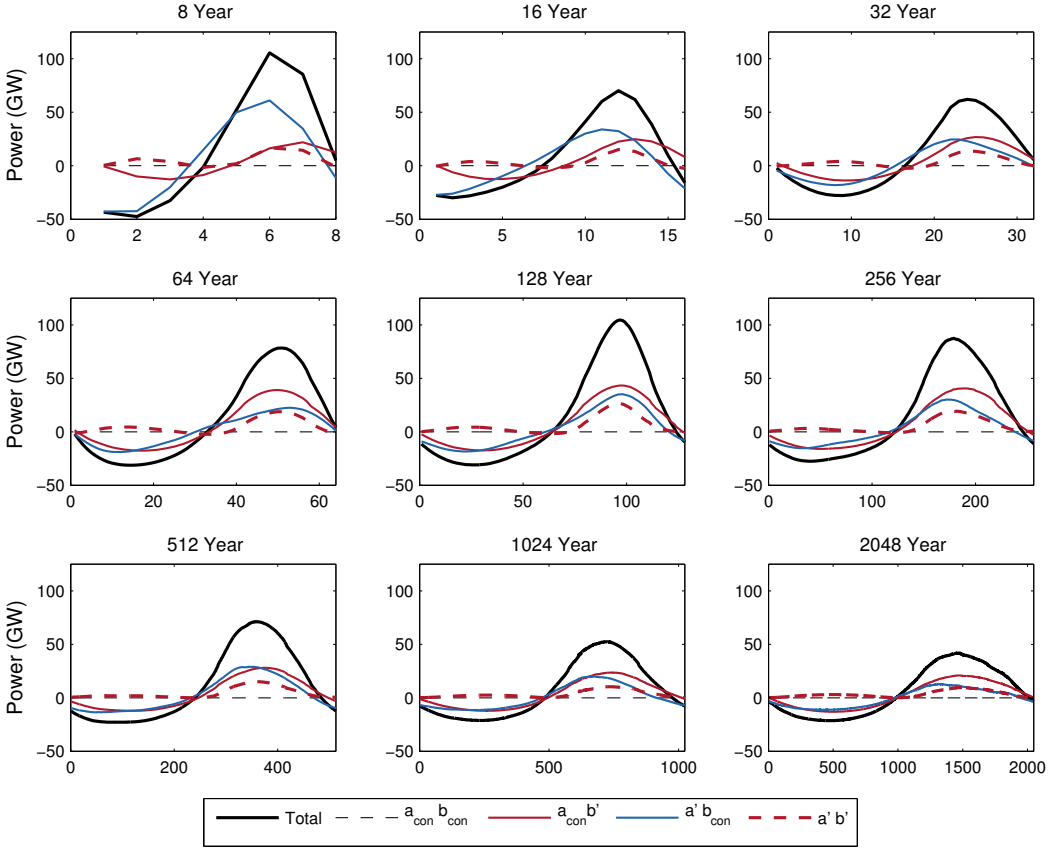

Figure 4.8: The reference state GPE component of G^A (integrated between 50°N and 70°N, units: 1 GW = 10^9 W), decomposed into contributions from: the temporally invariant control values (black dashed), variability in the reference depth (red), variability in the density tendency (blue), and covariations between these two terms (red dashed).

covariance term, $a'b'$ is positive in almost all instances, regardless of the phase of the oscillation. When $a' < 0$, the buoyancy of the surface layer is being increased and, consequently, its reference depth shoals ($b' < 0$). Conversely, when $a' > 0$, the buoyancy of the surface layer is being decreased and, consequently, its reference level deepens ($b' > 0$). This correlation acts to accentuate the increase in AGPE generation during the cooling phase and attenuate the reduction in AGPE generation during the warming phase.

The largest power input by surface buoyancy fluxes occurs at 128 year timescales, when the reference depth (averaged between 50°N and 70°N) for $t = 3P/4$ (where P is the forcing period, i.e. the year of maximum atmospheric cooling perturbation) is also greatest. At this timescale, the largest contribution comes from $a_{con}b'$, the variability in the reference level. The dominant control of the reference state on AGPE generation was also found to account for the difference in AMOC collapse and recovery timescales in an idealised, freshwater perturbation study (Hogg et al., 2013). However, it is not clear why the maximum reference state displacement occurs at this centennial timescale. The reference displacement of a fluid parcel is jointly determined by both its local density and the density profile of the global reference state. In principle, we would expect the maximum density attained by a surface fluid parcel during a forcing cycle to saturate at relatively short, decadal timescales. Conversely, we would not expect to see significant changes in the global reference state until centennial timescales, due to the filling of the deep ocean with dense water. As the depth of the global pycnocline shoals, the reference depth a surface fluid parcel might attain will also shoal accordingly. Therefore, one might hypothesise that maximum reference state displacement would occur at a short, intermediate timescale when the sea surface density is maximised, but the deep ocean has not yet had time to respond. However, Figure 4.9a shows that sea surface density *alone* is a good predictor of maximum reference state displacement.

The dominant role of sea surface density in determining z_{ref} can be isolated by calculating z_{ref} (at maximum cooling) for each forcing cycle using a fixed reference state profile, $\rho_{\text{ref}}(z)$. This can be done by solving $\rho(\theta, S, z_{\text{ref}}) - \rho_{\text{ref}}(z_{\text{ref}}) = 0$ for z_{ref} to find the level of zero buoyancy in an arbitrary reference state (Tailleux, 2013b).

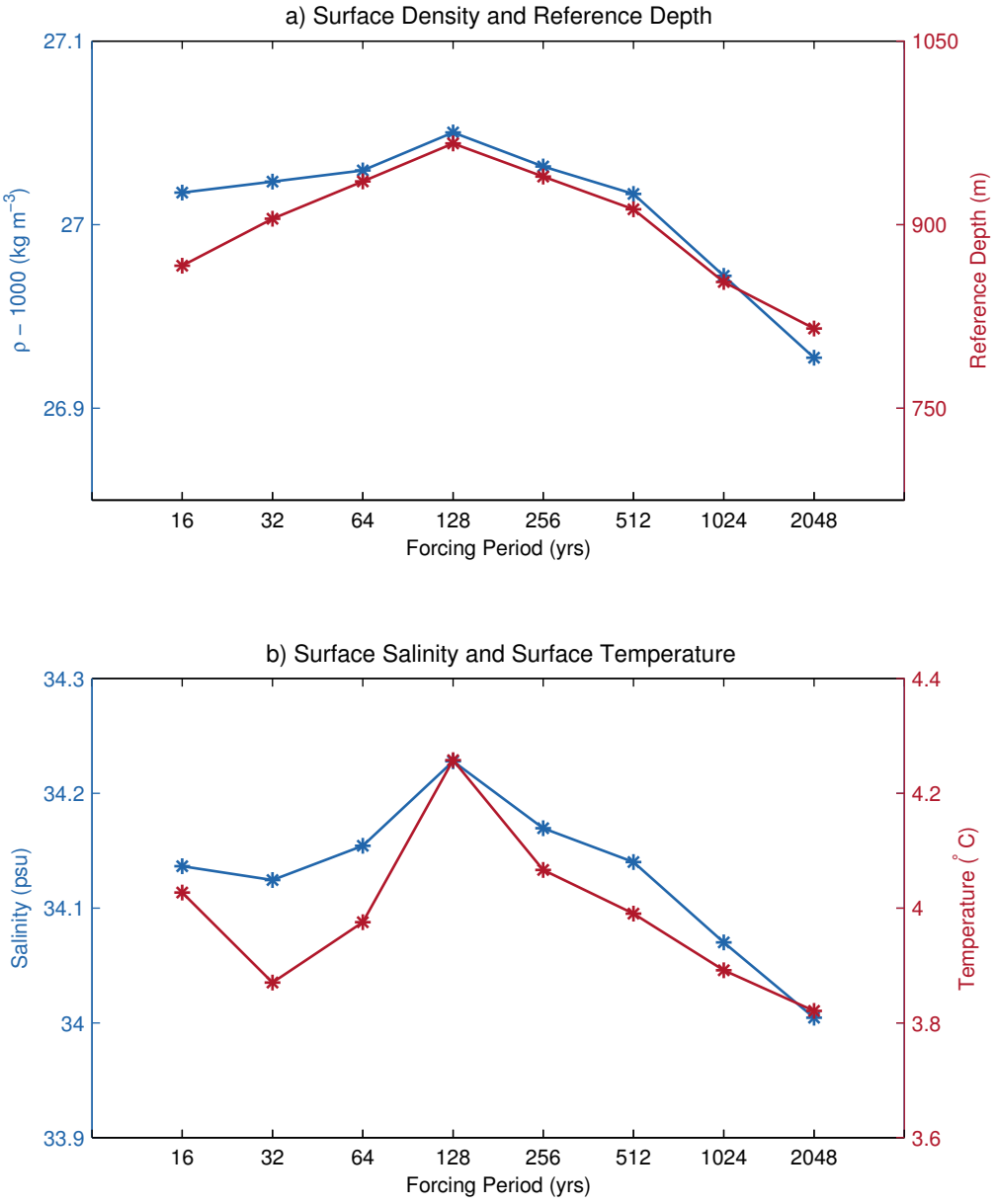

Figure 4.9: Plot showing a) the sea surface density anomaly, $\rho - 1000$ (units: kg m^{-3}), plotted alongside the surface reference depth (units: m) and b) the sea surface salinity (units: psu) plotted alongside sea surface temperature (units: °C). Each value is taken at time $t = 3P/4$, where P is the length of the forcing cycle, i.e. the point of maximum cooling. All quantities are averaged annually and spatially averaged over the Atlantic between 50°N and 70°N.

We use values of θ and S taken at time $t = 3P/4$ for each forcing cycle (of length P), spatially-averaging them over the high-latitude North Atlantic between 50°N and 70°N. We define the fixed reference state profile to be that of the resonant 128 year forcing cycle (in Year 96). The pattern of maximum reference state

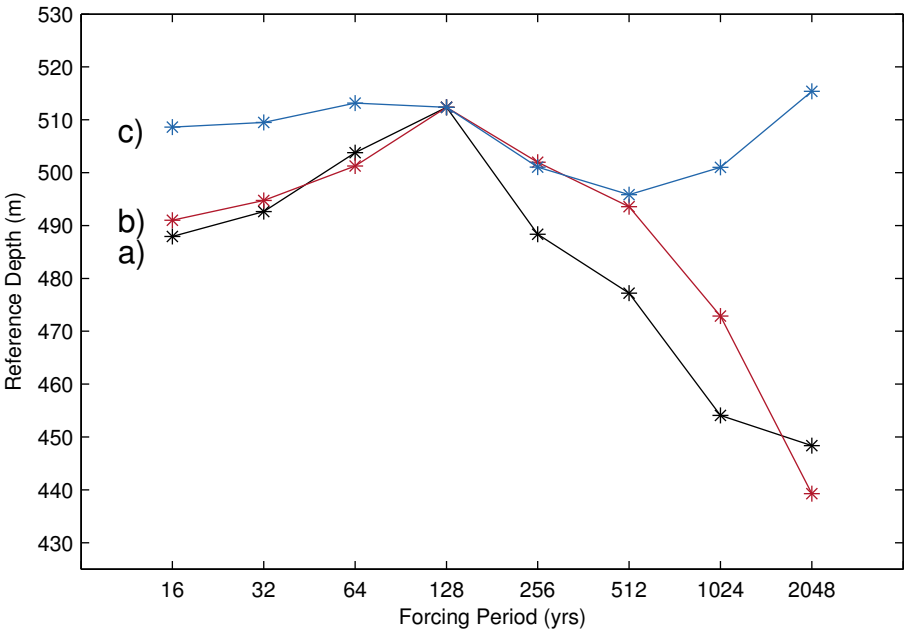

Figure 4.10: Plot showing the reference depth (at time $t = 3P/4$) calculated using a) variable θ, S and variable reference state profiles, b) variable θ, S and a fixed reference state profile (from the 128 year forcing cycle), and c) fixed θ, S (from the 128 year forcing cycle) and variable reference state profiles. θ, S are spatially-averaged over the Atlantic between 50°N and 70°N.

displacement attained during each forcing cycles is well reconstructed using this method (Figure 4.10, red line). Alternatively, we can investigate the influence of the global reference state profile by taking spatially-averaged θ and S properties from the 128 year oscillation and solving for the reference depth using reference state density profiles from each of the other forcing cycles. In this case, we see much smaller variations in reference state displacement, especially at short timescales (Figure 4.10, blue line). Note that the reference depths attained here are smaller than those shown in Figure 4.9a due to the spatial-averaging of surface properties prior to the calculation of the reference depth and the inherent nonlinearity of the reference depth calculation.

4.3.2 Conversion from AGPE to KE

Whilst the previous section strongly implies that the magnitude of the AMOC response is determined by the magnitude of power input by surface buoyancy

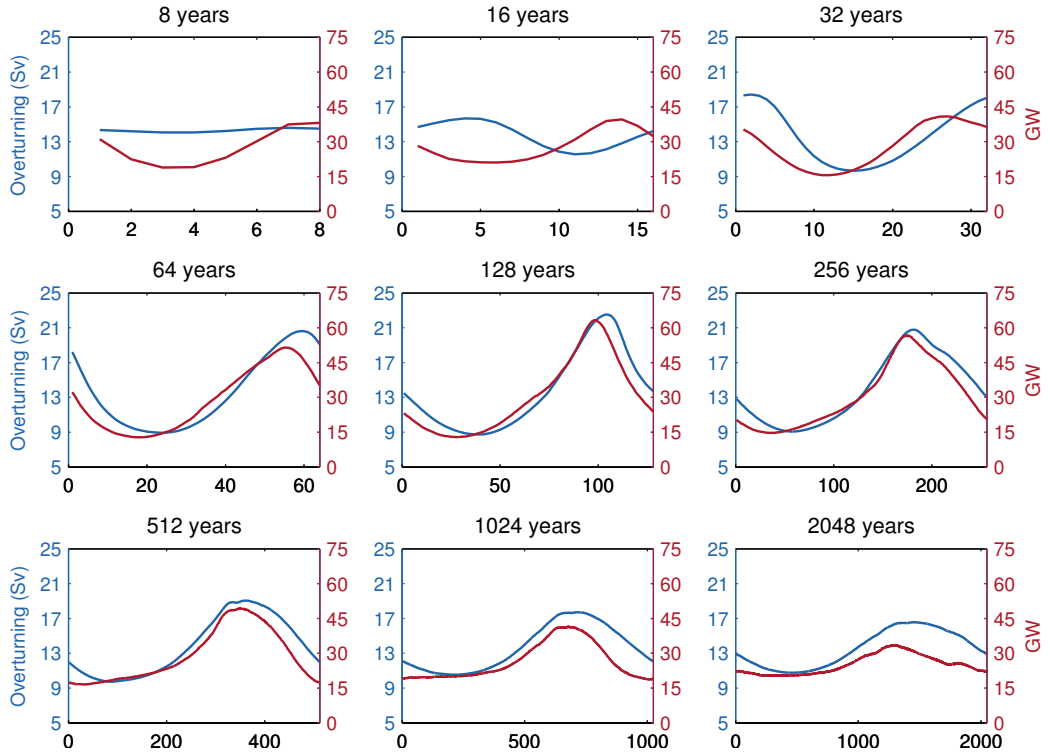

Figure 4.11: Timeseries of the AMOC response at 1000m, 35°N (blue, units: 1 Sv = 10^6 m^3 s^{-1}) and B^A integrated between 50°N and 70°N in the North Atlantic (red, units: 1 GW = 10^9 W) for each forcing cycle.

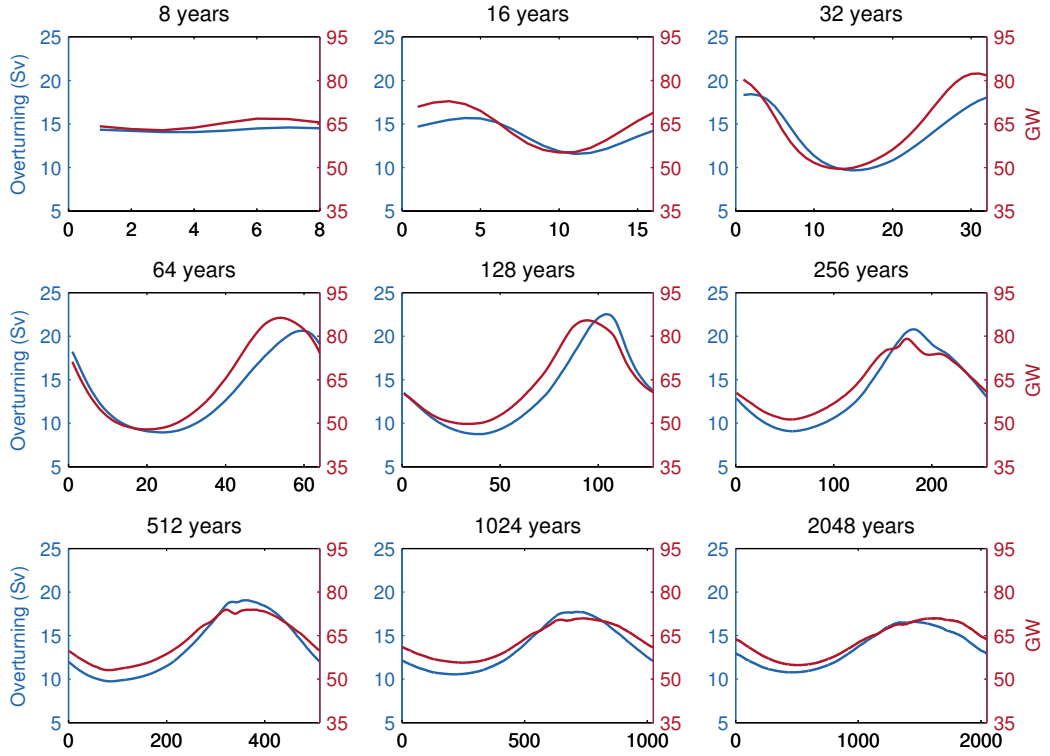

Figure 4.12: Timeseries of the AMOC response at 1000m, 35°N (blue, units: 1 Sv = 10^6 m^3 s^{-1}) and B^A integrated over the western boundary in the North Atlantic (red, units: 1 GW = 10^9 W) for each forcing cycle.

forcing, it would only be true to say that these changes in AGPE generation are driving variability in overturning if they were accompanied by changes in the conversion rate between AGPE and KE. In particular, it must be demonstrated that increased overturning directly corresponds to an increased consumption of AGPE in our transient experiments. This can be verified by calculating temporal variations in the conversion term in B^A over the Atlantic. Alternatively, increased AGPE input might simply result in an increased reservoir of AGPE or be dissipated via alternative pathways (e.g. through convective adjustment or the parameterised effect of mesoscale eddies) and need not be manifested in changes in large-scale ocean circulation.

Figures 4.11 and 4.12 show timeseries of B^A integrated regionally in the Atlantic over the western boundary and between 50°N and 70°N, respectively. These regions are delineated by the black boxes shown in Figure 4.4. In general, when the AMOC is stronger, more AGPE is consumed by the circulation in both the deepwater overflow regions and along the western boundary. Gregory and Tailleux (2011) found a strong correlation between AMOC weakening and a reduction in B^A integrated between 50°N and 70°N. However, we find that the AGPE to KE conversion occurring in the western boundary is a much stronger predictor of both the amplitude and pacing of the AMOC response. For instance, the high-latitude integral of B^A overestimates the amplitude of the response at short timescales and underestimates the amplitude of the response at multi-centennial timescales. This supports the Sijp et al. (2012) analytical model linking the strength of the AMOC to western boundary AGPE/KE conversion, facilitated by meridional density gradients.

4.4 The energetics of the lower MOC cell response

The global meridional overturning circulation is comprised of two overturning cells: an upper and a lower cell (e.g. Lumpkin and Speer (2007)). The upper cell

is the recirculation of deep water formed in the North Atlantic (NADW), whilst the lower cell is the recirculation of Antarctic Bottom Water (AABW) formed in the Southern Ocean, principally in the Ross and Weddell Seas. Thus far in this chapter, we have focussed on the upper cell response to variable buoyancy forcing in the North Atlantic. However, in Chapter 3, we saw that overturning variability induced in the North Atlantic does not remain confined to the basin, but, instead, propagates throughout the global ocean at centennial timescales. In this section we discuss the remote response of the lower overturning cell in the Southern Ocean to variability in North Atlantic buoyancy forcing.

4.4.1 Residual overturning

Meridional transport in the Southern Ocean consists of the northward wind-driven Ekman transport of dense water by the Eulerian mean circulation and the opposing southward eddy return flow of light water. The net meridional transport is referred to as the residual overturning circulation: the sum of the Eulerian-mean overturning streamfunction and the eddy-induced overturning streamfunction (Marshall and Radko, 2003). Both of these components (and their sum) are plotted for the ORCA2 control simulation in Figure 4.13. The eddy-induced contribution is largest across the Antarctic Circumpolar Current (ACC) and is generally small elsewhere. In ORCA2, the simulated lower cell in the residual overturning framework has a strength of 13.6 Sv with the maximum intensity occurring at a depth of 3500m. Observations suggest that the strength of the lower cell is approximately 20 Sv (Ganachaud and Wunsch, 2003; Lumpkin and Speer, 2007), but there are large uncertainties in these estimations. Numerical general circulation models vary widely in their simulation of lower cell overturning in the Southern Ocean (e.g. Figure 7 of Downes and Hogg (2013)). Given the uncertainty that exists, both the strength and structure of lower cell overturning in ORCA2 appear reasonable.

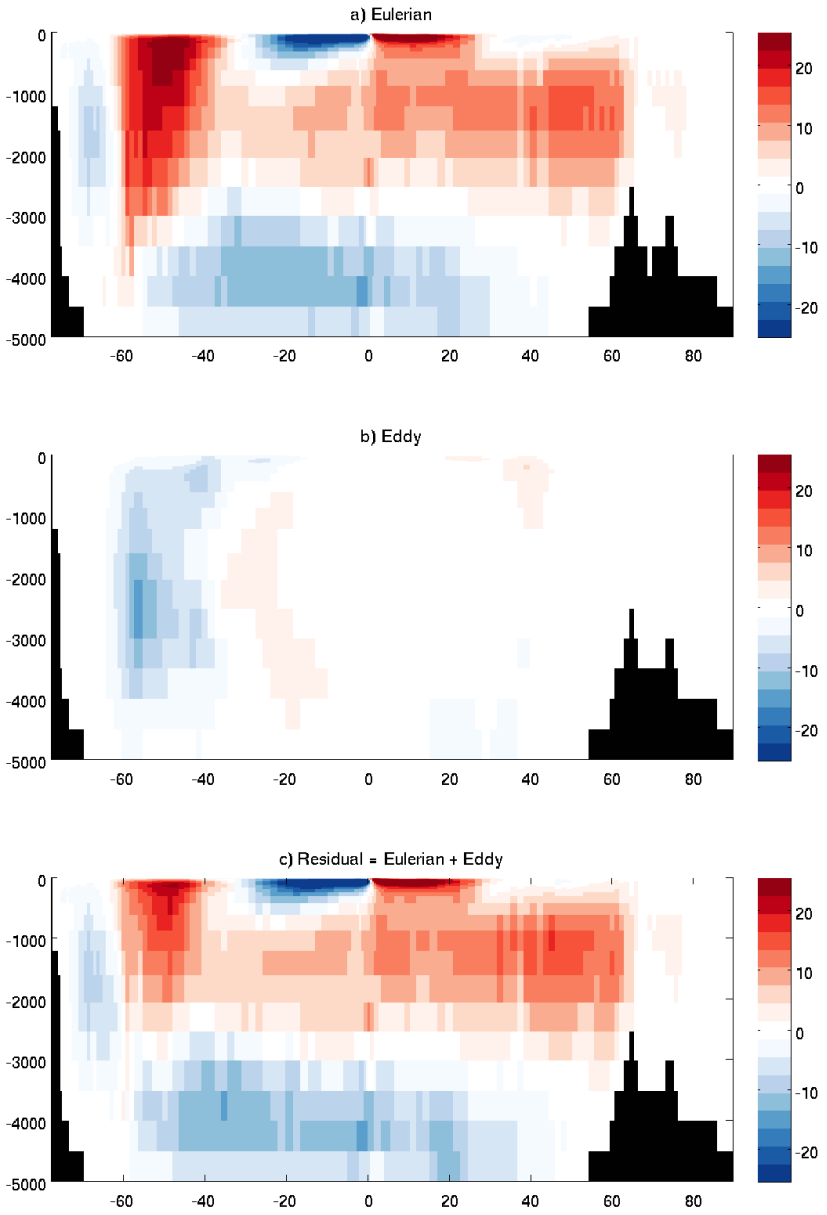

Figure 4.13: The a) Eulerian mean, b) eddy-induced, and c) residual overturning streamfunctions for the ORCA2 control simulation (units: 1 Sv = 10^6 m^3 s^{-1}). Contours are at 3 Sv intervals.

4.4.2 The lower cell response to North Atlantic buoyancy forcing

In the following analysis, we will measure the strength of lower cell overturning in the Southern Ocean by the magnitude of the residual overturning streamfunction

at 3500m, 30°S. This point is, approximately, situated in the region of strongest control overturning (Figure 4.13). The timeseries of lower cell overturning for each forcing period are plotted in Figure 4.14 (blue line) and the mean and range statistics are tabulated for each forcing cycle in Table 4.1. At multi-decadal timescales, the magnitude of the response is small. However, at longer timescales the amplitude of the lower cell response increases, becoming larger with forcing period. The structure of the response is broadly consistent with the concept of a 'bipolar seesaw': when upper cell overturning is strong, lower cell overturning is weak, and vice versa (Figure 4.14).

Forcing Periods (yrs)	Mean (Sv)	Range (Sv)
8	12.0	0.1
16	12.0	0.3
32	12.2	0.9
64	12.0	1.7
128	12.2	2.4
256	12.6	1.4
512	12.5	3.0
1024	12.4	6.0
2048	12.4	7.4

Table 4.1: The mean magnitude and range of lower cell overturning at 3500m, 30°S for each forcing period (units: 1 Sv = 10^6 m^3 s^{-1}).

Although many traditional conceptual models of upper cell overturning consider only local processes, Gnanadesikan (1999) approached the discussion from an alternative perspective, framing the dynamics of ocean overturning in terms of the global pycnocline depth separating the buoyant surface layer from the dense deep ocean (connected to the surface only at high-latitudes). The Gnanadesikan (1999) model incorporates fluxes of dense water from the deep ocean into the buoyant surface layer through low-latitude upwelling and wind-driven upwelling in the Southern Ocean. Light water is then returned in the Southern Ocean via the compensating Eddy-induced circulation or transported into the deep ocean via Northern Hemisphere deepwater formation and downwelling. This model can, in effect, be thought of as a global GPE budget (Johnson et al., 2007): deepening the global pycnocline increases global GPE, whilst shoaling the global pycnocline reduces global GPE.

Since there are no atmospheric forcing perturbations applied outside of the North Atlantic, we hypothesise that changes in lower cell overturning occur in passive response to changes in the depth of the global pycnocline (and, therefore, the amount of available potential energy) caused by changes in upper cell overturning in the North Atlantic. Increased upper cell overturning drains the buoyant surface layer and fills the deep ocean with dense water (over centennial timescales), resulting in a shoaling of the low-latitude pycnocline, a reduction in internal density gradients and, consequently, a reduction in the AGPE reservoir. Conversely, weaker upper cell overturning results in a deepening of the low-latitude pycnocline and an increase in global AGPE. We hypothesise that this reduction/increase in global available potential energy leads to a reduction/increase in lower cell overturning at multi-centennial and millennial timescales.

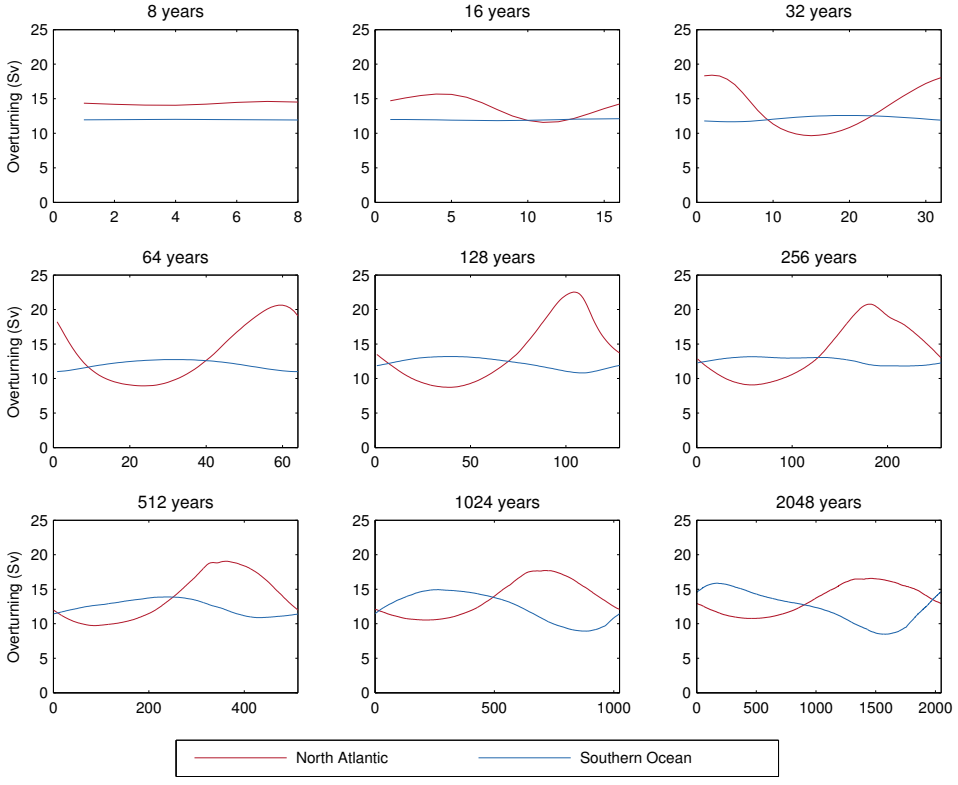

Figure 4.14: Timeseries of the magnitude of North Atlantic overturning at 1000m, 35°N (red) and Southern Ocean overturning at 3500m, 30°S (blue) for each forcing cycle (units: 1 Sv = 10^6 m^3 s^{-1}).

4.4.3 Conversion from AGPE to KE

In order to link changes in lower cell overturning to changes in the amount of potential energy available, it must first be shown that the lower cell requires (consumes) AGPE in our model (as we demonstrated for the upper cell in Section 4.3.2). This can be determined by examining the relationship between the strength of lower cell overturning and the local conversion rate from AGPE to KE. Whilst we have already stated that B^A integrated over the Southern Ocean is large and negative (unlike in the Atlantic, in which it is positive, Section 4.2.2), this integral is dominated by the large adiabatic generation of AGPE through the wind-driven upwelling of dense water and downwelling of light water occurring across the ACC in the upper 300m of the ocean. Below approximately 650m, $-\int \mathbf{u_h} \cdot \nabla_h p \, \mathrm{d}A$ (horizontally integrated over the Southern Ocean south of 30°S) reverses sign, becoming positive throughout the remainder of the water column (Figure 4.15).

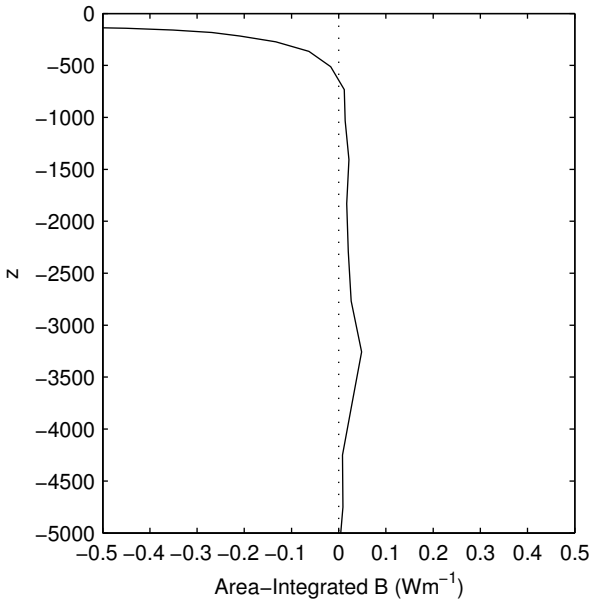

Figure 4.15: Vertical profile of $-\int \mathbf{u_h} \cdot \nabla_h p \, \mathrm{d}A$, horizontally integrated over the Southern Ocean south of 30°S (units: W m^{-1}). Note: the x-axis scale is saturated near the surface.

Integrated over the thickness of the lower cell (below 3500m, south of 30°S), we see a very strong correlation between lower cell overturning and the conversion of AGPE to KE (Figure 4.16), in which increased overturning in the Southern Ocean

coincides with an increased consumption of AGPE. Such a relationship has not been previously identified for the lower overturning cell in a realistic global ocean model.

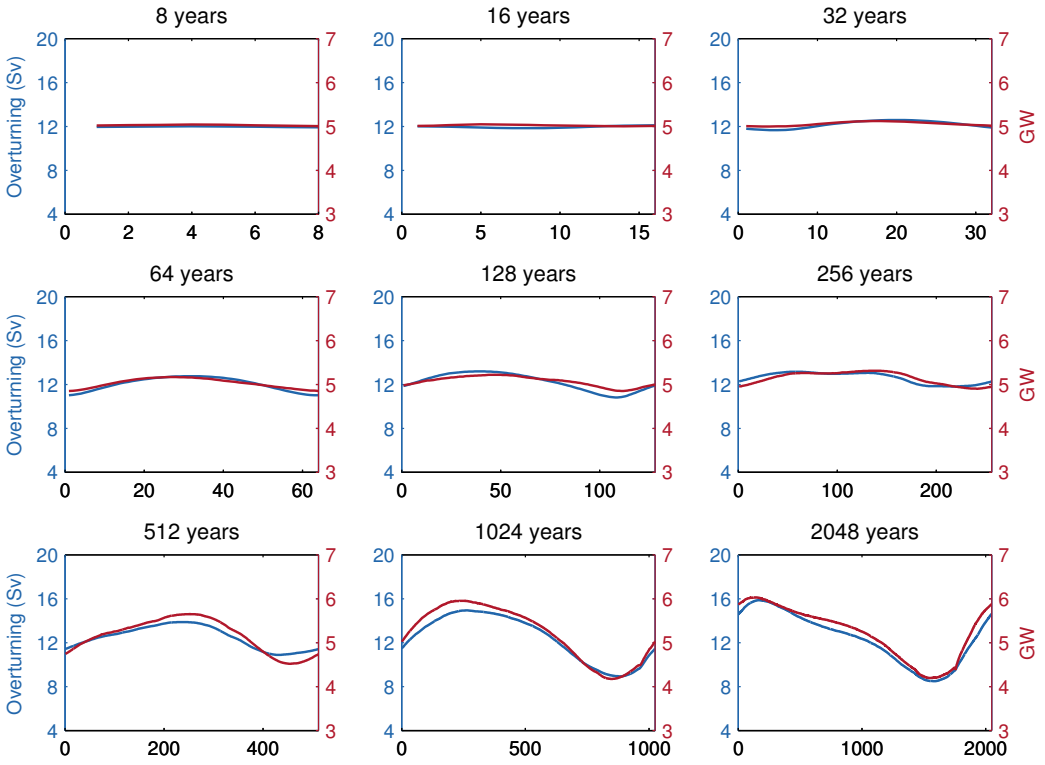

Figure 4.16: Timeseries of the magnitude of Southern Ocean overturning at 3500m, 30°S (blue, units: 1 Sv = 10^6 m^3 s^{-1}) and $-\mathbf{u_h} \cdot \nabla_h p$ volume integrated over the Southern Ocean below 3500m and south of 30°S (red, units: 1 GW = 10^9 W) for each forcing cycle.

4.4.4 Regional variations in available PE

The fundamental basis of our hypothesis is that the strength of lower cell overturning is limited by the amount of potential energy available for conversion to KE in the Southern Ocean. A number of definitions of positive-definite available potential energy (APE) densities have been proposed recently to enable APE to be quantified at a regional level (e.g. Winters and Barkan (2013); Tailleux (2013b)). We utilise the APE density of Tailleux (2013b), defined to be the work done against buoyancy forces when moving a fluid parcel between its physical position and its

reference state position:

$$\xi_a(x, y, z) = -\int_{z_{\text{ref}}}^{z} b_{\text{ref}}(x, y, z')\, \mathrm{d}z' \tag{4.14}$$

in which the buoyancy, b_{ref}, is calculated relative to the reference state profile, ρ_{ref}:

$$b_{\text{ref}}(x, y, z') = -\frac{g}{\rho_0}\left(\rho(x, y, z') - \rho_{\text{ref}}(z')\right). \tag{4.15}$$

The APE of a fluid volume is then given by:

$$\text{APE} = \rho_0 \int \xi_{\text{a}}\, \mathrm{d}V. \tag{4.16}$$

Equation 4.14 can be interpreted as the sum of 1) the difference between the potential energy of the fluid parcel at z and z_{ref} and 2) the work done against the background pressure gradient in moving between z and z_{ref} (Tailleux, 2013b). The definition of potential energy here includes both gravitational potential energy and the adiabatic change in internal energy in moving from z to z_{ref}. The latter arises due to the compressibility of seawater. Huang (2005) showed the contribution of available internal energy, AIE, to overall APE (AGPE+AIE) in the ocean is significant, being both large and negative. However, in ocean models that utilise a linear equation of state (as is typical of many of the existing studies of ocean energetics: e.g. Saenz et al. (2012); Hogg et al. (2013); Dijkstra et al. (2014)) AIE = 0 and, therefore, APE and AGPE are equivalent. The reader is encouraged to refer to Tailleux (2013b) for a more comprehensive description of this measure of APE density and for derivations of its physical properties.

The regional amount of APE in both the North Atlantic (north of 30°N) and the Southern Ocean (south of 30°S) are plotted in Figure 4.17 for multi-centennial and millennial timescales. It is evident that lower cell overturning correlates well with APE content in the Southern Ocean at millennial timescales, supporting our hypothesis that strong upper cell overturning results in a reduction in APE elsewhere at long timescales and that this reduction explains the weakening of lower cell overturning in the Southern Ocean. The converse is also true: weak

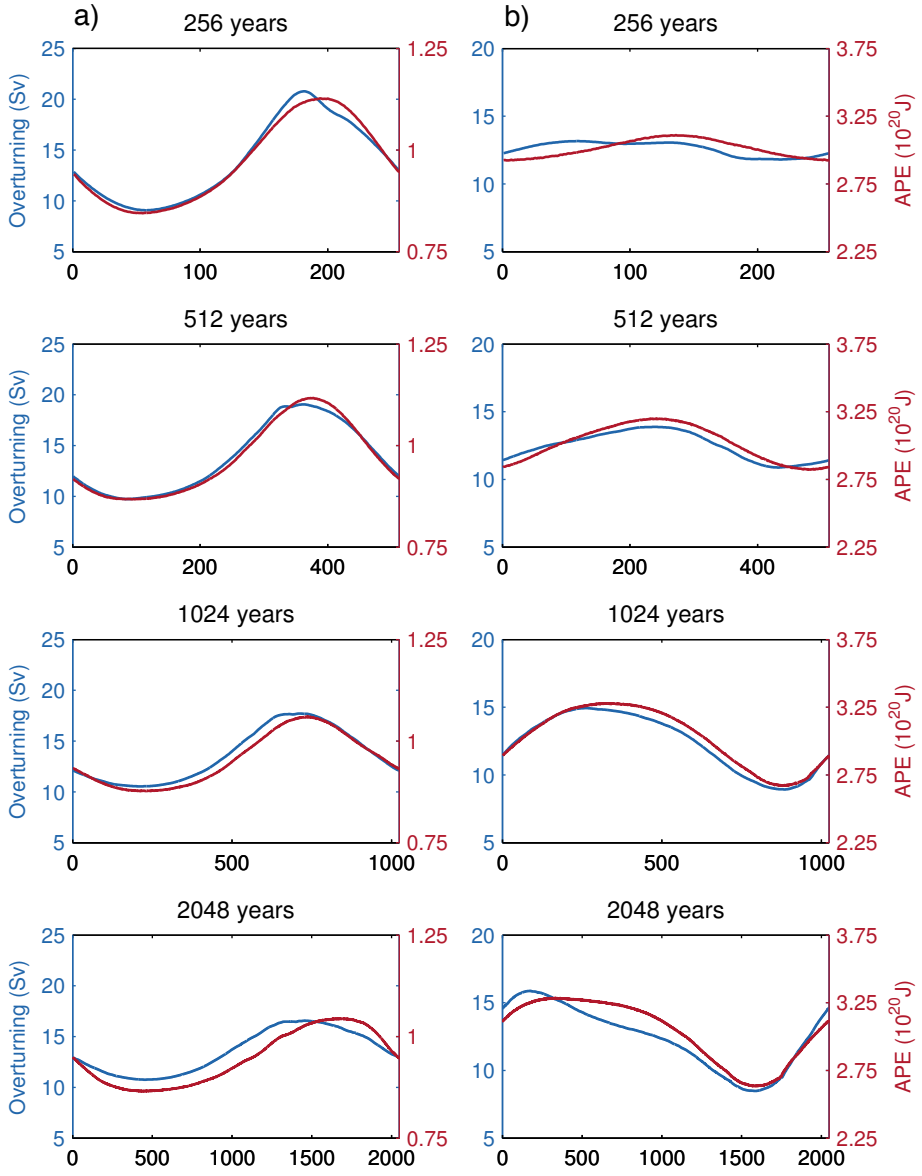

Figure 4.17: Comparative plots of a) upper cell overturning in the North Atlantic and APE density integrated north of 30°N in the Atlantic and b) lower cell meridional overturning in the Southern Ocean and APE density integrated south of 30°. Overturning strength is given in units of 1 Sv = 10^6 m^3 s^{-1} and APE density is given in units of 10^{20} J.

upper cell overturning results in an increase in global APE and a strengthening of lower cell overturning. Meanwhile, upper cell overturning also correlates well with local APE content in the North Atlantic (north of 30°N).

4.4.5 AGPE generation in the Southern Ocean

Whilst it is evident that lower cell overturning weakens with a reduction in the APE content, the explanation of this being a passive response to changes in the global pycnocline appears to be incomplete when considered from the perspective of the ocean's mechanical energy budget. Though there are no buoyancy forcing perturbations applied outside of the North Atlantic, the direct AGPE input by surface buoyancy forcing in the Southern Ocean varies substantially at long timescales (Figure 4.19). As discussed previously in Section 4.3.1, we are restricted to the use of annually averaged model output at the longest forcing timescales. Figure 4.18 plots AGPE generation by surface buoyancy fluxes in the Southern Ocean using both monthly and annually averaged model output. As in the North Atlantic, the mean power input is underestimated (in this case, by a scale factor of 3.5), but the relative interannual variability is well predicted at all timescales. Consequently, we are confident that we are able to describe multi-centennial variability in AGPE generation in the Southern Ocean using annually averaged model output.

The buoyancy anomaly associated with the dense surface waters surrounding Antarctica, relative to the global ocean, is jointly dependent on both local density and ocean density elsewhere. Consequently, significant changes in North Atlantic buoyancy can remotely affect the relative buoyancy of the surface ocean surrounding Antarctica and, therefore, alter the local value of z_{ref} in the Southern Ocean. This effect is so large at millennial timescales that the range in power input by buoyancy forcing in the Southern Ocean during the 2048 year forcing cycle is significantly larger than that integrated over the entire North Atlantic. The difference in surface layer reference state displacement is shown concurrently for both the northern and southern hemispheres in Figure 4.20. Timeseries of the AGPE input by surface buoyancy forcing in the Southern Ocean (integrated south of 30°S) for each forcing period are plotted in Figure 4.19. The magnitude of variability is small at multi-decadal timescales, but increases with forcing period. At multi-centennial (and longer) timescales, the direct AGPE input by surface buoyancy

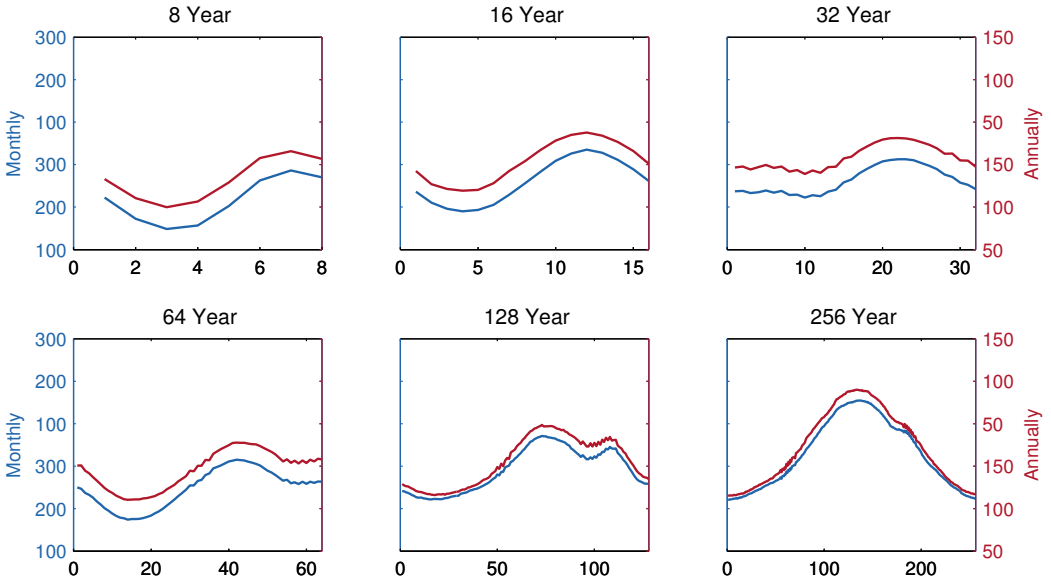

Figure 4.18: G^A, integrated over the Southern Ocean south of 30°S, calculated using both monthly (blue) and annually (red) averaged model output (units: 1 GW = 10^9 W).

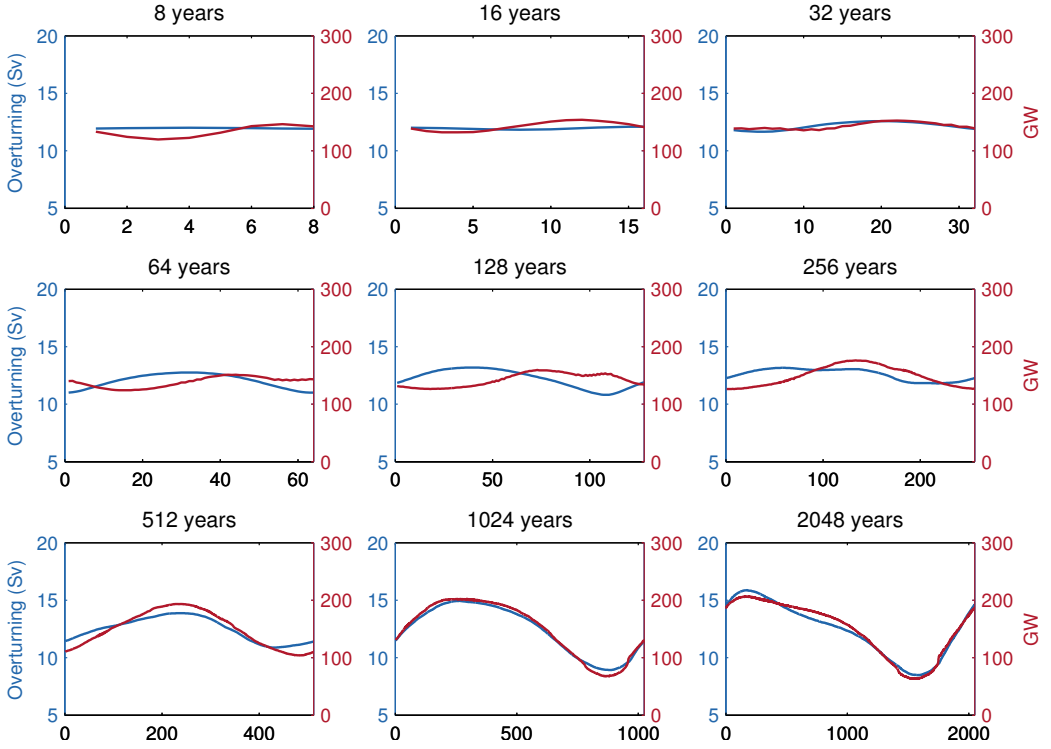

Figure 4.19: Timeseries of the strength of lower cell overturning at 3500m, 30°S (blue, units: 1 Sv = 10^6 m^3 s^{-1}) and G^A integrated over the Southern Ocean south of 30°S (red, units: 1 GW = 10^9 W, calculated using annually averaged model output)

forcing in the Southern Ocean strongly correlates with the strength of lower cell overturning. This suggests a directly mechanically forced response, rather than a passive adjustment to internal stratification. There is the suggestion of a lag between power input and overturning at multi-decadal timescales, though this is somewhat inconclusive given the element of nonlinearity in the structure of the signal at intermediate timescales.

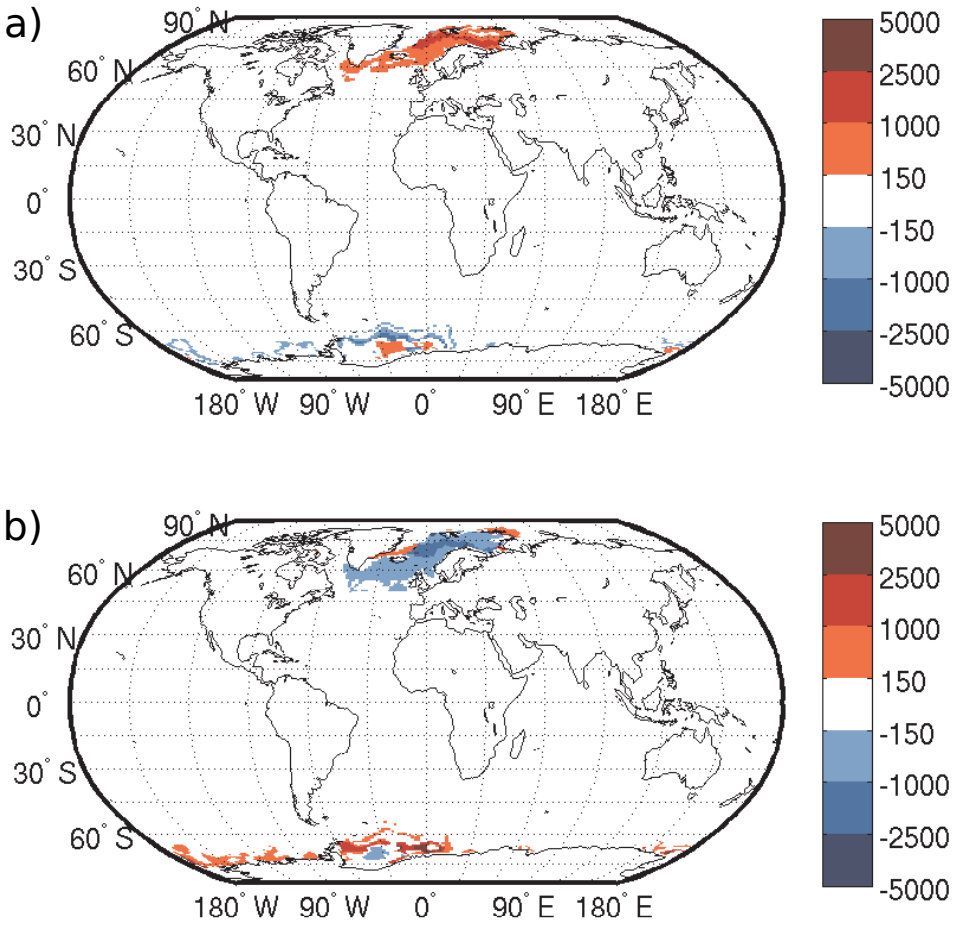

Figure 4.20: The surface layer reference state displacement (given as an anomaly from the control simulation) for the 2048 year forcing cycle at a) the warmest perturbation (year 512) and b) the coldest perturbation (year 1536) to atmospheric air temperature over the North Atlantic (calculated using annually averaged temperature, units: m). Note: a nonlinear colour scale is used in this figure.

4.5 Discussion and conclusions

In this chapter, we have sought to describe the mechanisms underlying the transient response of the global MOC to different timescales of variability in surface buoyancy forcing. We have diagnosed two of the key components of the ocean's potential energy budget and these have provided invaluable insights into the transient behaviour of both the upper and lower overturning cells. In doing so, we have extended the existing transient energetics literature (e.g. Gregory and Tailleux (2011); Saenko (2013); Hogg et al. (2013); Dijkstra et al. (2014)) across a broad range of timescales using a realistic ocean general circulation model.

Though the amplitude of the oscillations in atmospheric forcing imposed over the North Atlantic are held constant for all timescales, the magnitude of AGPE input by surface buoyancy fluxes varies with forcing period. The range of high-latitude AGPE input was found to be predictive of the range of the AMOC response (including its resonant period) at multi-decadal (and longer) timescales. This variability in power generation was determined by the magnitude of the reference state displacement. Contrary to our expectations, the dominant mechanism underlying changes in the reference depth of the high-latitude surface layer was actually local sea surface density and not adjustments in deep ocean stratification. It is beyond the scope of this chapter to fully explore the reasons for the increase in surface density at centennial timescales that leads to this maxima in AGPE power generation. However, Figure 4.9b implies that some form of advective feedback involving the advection of warm, saline water from low-latitudes to high-latitudes may be responsible. The effect of salinity is dominant, leading to an increase in density and a deepening of the reference level. Such an advective feedback has also been previously invoked in mechanistic descriptions of multi-decadal and centennial AMOC oscillations (e.g. Griffies and Tziperman (1995)). There is an additional secondary effect of this feedback: when the sea surface is warmer, the sensible heat flux through the surface due to atmospheric cooling is larger (due to the greater temperature gradient between atmosphere and ocean (Large and

Yeager, 2008)), thus explaining the increase in the contribution of $a'b_{con}$ to overall AGPE generation that is also seen at the resonant timescale.

In the North Atlantic, AGPE is converted to KE both in regions of deepwater formation and along the western boundary. Gregory and Tailleux (2011) and Saenko (2013) found a very good correlation between changes in B^A at high-latitudes (integrated between 50°N and 70°N) and changes in AMOC strength in response to perturbations in atmospheric CO_2. However, AGPE conversion to KE is more than twice as large in the western boundary than at high-latitudes in the ORCA2 control simulation (Section 4.2.2). Our results suggest that B^A integrated over the western boundary is, in fact, a better predictor of the AMOC response to periodic buoyancy forcing across all timescales. This is in agreement with the analytical model of Sijp et al. (2012), in which AMOC strength is linked to western boundary meridional density gradients through the local conversion between AGPE and KE. Whilst it is generally true that increased/decreased AGPE conversion at high-latitudes coincides with a stronger/weaker AMOC, the correlation is not as strong as that of Gregory and Tailleux (2011) in our experiments. This could be due to the pronounced periodicity in forcing in our experimental setup, in contrast to the CO_2 doubling scenarios of Gregory and Tailleux (2011) and Saenko (2013) in which there is a strong linear trend in both forcing and response.

A similar relationship can also be extended to the lower overturning cell, where we found an equally strong correlation between the strength of overturning and the AGPE to KE conversion taking place below 3500m in the Southern Ocean. However, the magnitude of the AGPE to KE conversion occurring in the deep Southern Ocean (Figure 4.16) is much smaller than that found in the North Atlantic (Figure 4.11), even when the variability in overturning is comparable. The strength of meridional overturning (as measured by a volume transport) is an integrated function of the meridional velocity alone, but B is a joint function of both the horizontal velocity field and the horizontal pressure gradient. Despite the approximate equivalence in volume transport, we, thus, interpret the smaller energetic demand of the lower cell here to be due to the smaller density contrast

between the upwelling and downwelling branches of the lower cell (in comparison to that found in the upper Atlantic overturning cell).

The primary focus of this work has been on the generation of available potential energy and its subsequent conversion to kinetic energy. In this chapter, we have linked variability in upper cell overturning to the magnitude of local AGPE generation in the North Atlantic. This variability in upper cell overturning affects global ocean stratification through its control on the low-latitude pycnocline at centennial timescales (e.g. Gnanadesikan (1999)). Such adjustments of the global pycnocline have been previously used as a mechanism by which to explain how changes in surface buoyancy forcing in the North Atlantic can affect the strength of the ACC in the Southern Ocean. Fučkar and Vallis (2007) demonstrated that a reduction in North Atlantic deep water production resulted in a deepening of the low-latitude thermocline in both hemispheres. This resulted in an increased meridional density gradient across the ACC and, consequently, an increase in zonal transport via the thermal wind relationship. Similarly, Munday et al. (2011) showed that changes in the pycnocline induced by remote changes in diapycnal mixing also led to changes in ACC intensity. Both of these scenarios result in a change in interior density gradients and a change in the amount of available potential energy. However, the physical processes describing the large-scale strength of the ACC are relatively well understood, but a concise physical description of the strength of lower cell overturning in the Southern Ocean does not exist. Consequently, conventional dynamical arguments cannot be developed in the same way.

Instead, we must utilise large-scale energetic concepts to explain how variations in North Atlantic buoyancy forcing might lead to remote variations in global overturning, particularly in the lower Antarctic cell. As described in Section 4.4.2, a strengthening/weakening of the upper cell leads to a decrease/increase in the depth of low-latitude pycnocline and a decrease/increase in global AGPE. By quantifying the amount of potential energy locally available for conversion to KE, we were able to show that the magnitude of the variability induced in the upper and lower overturning cells at centennial timescales is well-predicted by the APE density integrated over the North Atlantic and Southern Ocean, respectively (Figure 4.17).

When upper cell overturning is strong, the buoyant surface layer is drained and the deep, global ocean fills with dense water. This reduction in the depth of the low-latitude pycnocline reduces the amount of APE in the Southern Ocean and lower cell overturning weakens. This relationship was also shown to hold in the North Atlantic, where the intensity of local APE generation by surface buoyancy fluxes in the North Atlantic is sufficient to dominate the reduction in APE content occurring through changes in the global pycnocline.

Surprisingly, we have shown that changes in North Atlantic surface buoyancy forcing can lead to large amplitude, remote oscillations in AGPE generation in the Southern Ocean, despite no perturbations in atmospheric forcing being imposed here. This is due to the dependence of local AGPE generation on the local surface buoyancy anomaly relative to the global ocean, as encapsulated by z_{ref}. It follows from this dependence that the Southern Ocean AGPE input due to remote buoyancy forcing forcing varies and, moreover, it varies out of phase with AGPE generation in the North Atlantic. When the high-latitude North Atlantic is warmed, the local surface layer becomes more buoyant (and the local AGPE input is reduced). Dense Southern Ocean fluid parcels then move to replace these, formerly dense, North Atlantic fluid parcels in the global reference state and, therefore, the Southern Ocean AGPE input due to surface cooling increases. Conversely, when the high-latitude North Atlantic is cooled, the opposite occurs (Figure 4.20). This spatial asymmetry provides an alternative perspective on the forced 'bipolar see-saw', suggesting that it is not simply a passive, interior response to remote buoyancy forcing, but is, instead, a phenomenon directly driven by hemispheric asymmetry in AGPE power input.

In conclusion, we have shown that diagnostics of transient ocean energetics can provide valuable insights into the role that surface buoyancy fluxes and the potential energy reservoir play in determining the response of the global MOC to variability in atmospheric forcing. These findings support the developing idea that surface buoyancy forcing is not energetically redundant, but does in fact exert an active energetic control on global ocean overturning.

Chapter 5

Conclusion

5.1 Summary and discussion

In this thesis, I have investigated the driving processes of the global meridional overturning circulation, revisiting the traditional notion of an MOC whose transport is determined by basin-scale meridional density gradients and exploring the role of surface buoyancy fluxes in driving changes in ocean circulation.

In recent years, the ocean's sources of mechanical energy have come into question, but much uncertainty over their magnitude remains (Wunsch and Ferrari, 2004) and the implications for ocean overturning are much debated (Kuhlbrodt et al., 2007). In Chapter 2, we explored the ocean's potential energy budget in the control simulation of the coupled atmosphere-ocean general circulation model HadCM3, diagnosing both the gravitational potential energy (GPE) and available gravitational potential energy (AGPE) budgets. This is the first time that the ocean's AGPE budget has been calculated using output from a coupled climate model. Discussing both of the GPE and AGPE budgets in a unified manner, we were able to highlight the similarities and differences between these two energetic frameworks. In physical oceanography, the more intuitive GPE is most widely referred to, particularly in the discussion of the driving processes of the MOC (e.g., Kuhlbrodt et al. (2007)). Nevertheless, only a small fraction of total GPE is

available for conversion to KE (e.g., Tailleux (2013a)) and this fraction is referred to as AGPE. Despite its dynamic importance, AGPE is largely only discussed within the energetics-focussed literature. This could be because the computation of AGPE budgets is far more complicated and expensive than the consideration of GPE, particularly when a nonlinear equation of state is used.

However, the distinction between GPE and AGPE is both useful and informative, enabling us to illustrate and isolate the different energetic roles played by adiabatic and diabatic processes. The resolved, large-scale circulation is a leading order source of (A)GPE (GPE: +0.57 TW, AGPE: +0.59 TW), whilst the unresolved, mesoscale eddy transports are the largest sink of (A)GPE (GPE: -0.82 TW, AGPE: -0.74 TW). These adiabatic processes have an almost identical effect on both GPE and AGPE, with the small discrepancies attributed to the effect of nonlinearities in the equation of state on numerical mixing. The adiabatic balance is dominated by Southern Ocean processes (Figure 2.5). Diabatic processes, however, have differing effects on GPE and AGPE, by mixing the background reference state. In this framework, diapycnal mixing (e.g., Munk and Wunsch (1998)) raises background GPE (+0.44 TW), but this is not made available (-0.12 TW). Conversely, surface buoyancy forcing acts to generate AGPE (+0.72 TW) at the expense of background GPE (-0.46 TW). We, thus, conclude that these diabatic processes are playing complementary roles in diabatically sustaining large-scale ocean circulation. Although it has been hypothesised previously that the AMOC is rate-limited by the adiabatic (e.g., wind-driven upwelling (Webb and Suginohara, 2001)) and diabatic (e.g., diapycnal mixing (Munk and Wunsch, 1998)) sources of GPE available to upwell dense water back across the pycnocline, it is apparent that the consideration of GPE alone is only sufficient for understanding the role of adiabatic processes, but insufficient for our understanding of the role of diabatic processes in driving ocean circulation. In HadCM3, diapycnal mixing is the primary source of background potential energy. However, this energy cannot be imparted to ocean circulation without the effect of surface buoyancy forcing. Therefore, it could be argued that surface buoyancy forcing also plays an active, and potentially rate-limiting, role in the energetics of MOC variability.

The distinction between adiabatic and diabatic processes using the global (A)GPE budget allows one to speculate on the nature of the ocean circulation that might exist if certain physical processes were removed from the ocean energy cycle. From Table 2.1, we can see that the primary balance in the GPE reference state budget (which is only affected by diabatic processes) is between diapycnal mixing and surface buoyancy forcing. For instance, in the limit of no vertical mixing (e.g., Toggweiler and Samuels (1998)), it is likely that the AGPE generated by surface buoyancy forcing would be reduced in the new equilibrium. In fact, this was seen by Toggweiler and Samuels (1998) using the quasi-geostrophic approximation for APE. In this adiabatic limit, the AGPE budget is effectively equivalent to the GPE budget. An adiabatic circulation might, thus, persist with wind-driven upwelling in the Southern Ocean supplying mechanical energy with mesoscale eddies then removing potential energy in the Southern Ocean and convection removing potential energy at high-latitudes.

Whilst the present-day MOC is considered to be driven by a combination of both adiabatic and diabatic processes (e.g., Wunsch (2002); Kuhlbrodt et al. (2007)), the complexities of this idea are not well-represented by the more traditional GPE framework. However, the influential Gnanadesikan (1999) two-layer conceptual model of overturning is, in effect, an ocean GPE budget (Johnson et al., 2007). The ideas developed within this thesis suggest that a conceptual model built around the AGPE framework might provide a more realistic representation of the driving processes of ocean circulation (and their associated feedbacks), though the precise construction of such a model is beyond the scope of this thesis. Despite this, we have seen how global changes in stratification can remotely alter ocean circulation, supporting the key premise of the Gnanadesikan (1999) model.

Despite the complexity of the global ocean system and mechanical arguments to the contrary, numerous attempts have been made to scale the strength of the meridional overturning circulation (MOC), principally in the North Atlantic, with large-scale, basin-wide hydrographic properties. In particular, various approaches to scaling the MOC with meridional density gradients have been proposed in a manner akin to Stommel (1961)'s 'thermohaline circulation', but the success of

these has only been demonstrated under limited conditions. Much of our understanding of the driving processes of the global MOC is based on steady-state or equilibrated perturbation experiments and not under genuinely transient conditions. Consequently, little effort has been made to determine the timescales over which such a relationship may hold. In Chapter 3, we presented a scaling relationship linking overturning to twice vertically integrated meridional density gradients (along the western boundary) via the hydrostatic equation and a 'rotated' form of the geostrophic equation. Using a series of periodically forced experiments in a global, coarse resolution configuration of the general circulation model NEMO, we explored the timescales over which this scaling is temporally valid. Despite nonlinearities in the ocean's response, we found that this scaling holds well in both the upper and abyssal Atlantic Ocean at multi-decadal (and longer) timescales. This relationship also carried over well to a higher-resolution simulation with stochastic, NAO-inspired forcing. These results demonstrate that meridional density gradients and meridional overturning are linked via meridional pressure gradients, and that both the strength and structure of the MOC can be predicted from hydrography on multi-decadal and longer timescales. This supports the use of such scalings in parameterising meridional volume transport in simplified box modelling studies (e.g., Oliver et al. (2005)). Such a scaling can also be used to help interpret long-timescale changes in global overturning.

However, the energetics of this induced variability is not clear. As discussed above, typical GPE-based arguments suggest that surface buoyancy forcing might play an important role in setting the structure of the AMOC, but not in energising it. In Chapter 2, however, we demonstrated that the role of surface buoyancy forcing in the more dynamically-relevant AGPE framework is quite different, providing a mechanism by which background GPE can be made available for conversion to KE. Therefore, in Chapter 4, we diagnosed the AGPE generation associated with each forcing scenario and the subsequent conversion to KE. We found that the amplitude of AMOC variability is well predicted by the amplitude of high-latitude AGPE generation variability in the North Atlantic. The overturning response to this increase in AGPE input appears to be determined, or at least well-predicted,

by the rate of conversion from AGPE to KE occurring in the western boundary, consistent with the strong relationship between AMOC strength and western boundary density gradients found in Chapter 3. Such a relationship was also seen to extend to the lower Antarctic cell in the Southern Ocean, with periods of increased overturning in both hemispheres coinciding with periods of increased local AGPE generation (triggered in the Southern Ocean by remote changes in the global density profile) and an increased reservoir of regionally-integrated APE density, accompanied by an increased regional consumption of AGPE by the resolved circulation. The amplitude of both the upper and lower cell response is well-predicted by the magnitude of variability in each of these terms in the North Atlantic and the Southern Ocean, respectively.

One of the key contributions of this thesis has been to inextricably link changes in large-scale density gradients and stratification to variability in meridional overturning through both scaled volume transport and the amount of potential energy made available for conversion to kinetic energy. We have shown that the western boundary plays a critical role in both of these processes, supporting the idea that western boundary meridional density gradients play a fundamental part in facilitating the conversion of potential energy to kinetic energy and driving changes in ocean circulation (Sijp et al., 2012). Variability in surface density can affect how much background GPE is made available locally by surface buoyancy fluxes (as seen in the Atlantic) and remotely alter AGPE generation elsewhere (as seen in the Southern Ocean). Meanwhile, the scaling relationship presented in Chapter 3 emphasises the importance of internal horizontal density gradients throughout the water column for determining meridional volume transport. This variability in internal stratification also affects the amount of potential energy made available regionally. At multi-centennial timescales, some of these effects can be well understood by the concept of a variable low-latitude pycnocline (e.g., Gnanadesikan (1999)). When North Atlantic overturning is strong, the ocean's buoyant surface layer is drained and the low-latitude pycnocline shoals. This reduces the amount of potential energy available in the Southern Ocean and also acts to attenuate the increase in APE in the North Atlantic (Figure 4.17). The effect of variability in

the low-latitude pycnocline was also evident in Chapter 3, in which the southern boundary density (representative of the low latitude pycnocline) acted to reduce the magnitude of the scaled AMOC response, opposing the influence of northern boundary buoyancy forcing (Figure 3.10). However, whilst Gnanadesikan (1999) only used pycnocline depth as a prognostic variable, it is evident that the variable meridional density difference is also important to AMOC dynamics. For instance, strong surface buoyancy forcing at high latitudes is sufficient to sustain an increase in both North Atlantic APE and the strength of the AMOC, despite the shoaling of the global pycnocline at long timescales.

5.2 Future Work

During the course of my postgraduate research, I have also contributed to two other studies aimed at improving our understanding of ocean energetics. Saenz et al. (2015) (in press) addresses two important issues in the construction of the GPE reference state when using a nonlinear equation of state: uniqueness and computational expense. By presenting a new analytical expression for the reference state based on the frequency distribution of volume occupied by different temperature and salinity classes, the range of fluid parcels that have a non-unique position in the reference state is shown to be small. Moreover, this construct allows for a much more efficient reference state computation, which opens up the possibility of the calculation of available potential energy budgets offline using high resolution model output. My contribution to the preparation of Saenz et al. (2015) (in press) was to provide an alternative implementation of the Huang (2005) adiabatic sorting algorithm, sorting the ocean from the surface, as opposed to filling from the bottom. These reference states are not identical due to nonlinearities in the equation of state, but the regions in which they differ are small and are well predicted by the region of non-uniqueness derived analytically. I have also assisted in the supervision of a Masters research student applying the methods developed in Chapter 2 to a transient, CO_2-forced climate change simulation of HadCM3 (Wu et al., 2015) (in preparation). This study has found (using a full decomposition

of the (A)GPE energy budget, as in Chapter 2) that the most important changes in the ocean's (A)GPE budget in response to an increase in atmospheric CO_2 are in the work of surface buoyancy forcing and advection (i.e., the KE/AGPE conversion term), supporting the restricted focus of Chapter 4.

Due to the broad scope of the experimental setup used in Chapters 3 and 4, there remains much to be understood in the ocean's response to periodic buoyancy forcing. For example, we have discussed the transient energetics of the global MOC from the perspective of AGPE generation by surface buoyancy forcing and the subsequent conversion of AGPE to KE. Whilst these diagnostics have proven to be highly informative, we do not have a complete diagnosis of all terms in the ocean's AGPE budget in ORCA2. In the future, it would be interesting to implement online diagnosis of the complete energy budget in NEMO to help further elucidate the role of surface buoyancy forcing in energising large-scale ocean circulation, although we do acknowledge that this a nontrivial exercise due the complex nature of the AGPE framework. Doing so, however, might help us to better understand the role of other physical processes in the ocean's response to transient buoyancy forcing. For example, a large amount of AGPE is input by surface buoyancy fluxes at high latitudes during the 8 year forcing cycle (Figure 4.6), but little of this is converted into KE (Figure 4.12). It is possible that this energy is dissipated locally via convective processes. However, a full AGPE budget would be required to verify this speculation. The role of internal energy could also be incorporated into the analysis by constructing a budget of Tailleux (2013b)'s APE density. However, this framework is even more computationally expensive and has yet to be applied to an ocean GCM, even at steady state. Although the role of internal energy must be clarified, we demonstrated in Chapter 2 that the global (A)GPE budget is schematically similar in multiple simulations, whether a linear or nonlinear equation of state is used. Whilst we have motivated the idea that both overturning cells depend on the amount of potential energy available for conversion to kinetic energy, it remains to get a full dynamical understanding of how this potential energy is converted to kinetic energy, particularly in western boundary currents. However, it is likely that future advances in conceptual modelling of the

MOC and western boundary dynamics will help advance our understanding even further.

Appendix A

Authorship Declaration: This appendix was authored by Kevin Oliver and has been published as supplementary material in Butler et al. (2013). This appendix is included here to support the derivation of the GPE framework used in Chapter 2. The analysis contained therein is my own.

Choosing a reference level for GPE budget calculations within the incompressible framework

Here, we examine the dependence of the error in the GPE budget (introduced by the use of the incompressible framework) on the choice of reference level for the GPE calculation. An expression for the time derivative of the areal concentration of GPE, GPE_A, valid for all frameworks, is

$$\begin{aligned}\frac{\partial(GPE_A)}{\partial t} &= \frac{\partial}{\partial t}\int_{-H}^{z_s}\rho g(z-z_0)\mathrm{d}z \\ &= \rho(z_s)g\big(z_s-z_0\big)\frac{\partial z_s}{\partial t}+\int_{-H}^{z_s}\frac{\partial}{\partial t}\Big(\rho g\big(z-z_0\big)\Big)\mathrm{d}z\ ,\end{aligned} \tag{A.1}$$

where z_0 is the reference level used in the GPE calculation, H is bathymetric depth, and z_s is the height of the surface. The only time-dependent variables here are ρ and potentially z_s, where $\partial z_s/\partial t = w(z_s)$, so we can write

$$\frac{\partial(GPE_A)}{\partial t} = \rho(z_s)g\big(z_s-z_0\big)w(z_s)+\int_{-H}^{z_s}g\big(z-z_0\big)\frac{\partial\rho}{\partial t}\mathrm{d}z\ . \tag{A.2}$$

Provided that the mass of the ocean does not vary, $\partial(GPE_A)/\partial t$ does not depend on the choice of z_0, because $\frac{\partial}{\partial t}\int_{-H}^{z_s} \rho g z_0 \, \mathrm{d}z$ vanishes in (A.1). However, the conservation of volume, as opposed to mass, within incompressible Boussinesq ocean models introduces a spurious mass generation term which also leads to a spurious z_0-dependent GPE generation term. We show here that this spurious term is small provided that the surface is chosen as the reference level (i.e. $z_0 = z_s$).

We first consider the expression for $\partial\rho/\partial t$. In the fully compressible framework, this is:

$$\frac{\partial \rho}{\partial t} = -\nabla.\big(u\rho\big) \ . \tag{A.3}$$

However, we also have

$$\rho \nabla.u = -\frac{D\rho}{Dt} \ , \tag{A.4}$$

so we can write

$$\frac{\partial \rho}{\partial t} = \frac{D\rho}{Dt} - u.\nabla\rho \ . \tag{A.5}$$

In the incompressible framework, the expression for $\partial\rho/\partial t$ is:

$$\frac{\partial \rho}{\partial t} = \frac{D\rho}{Dt} - \nabla.\big(u\rho\big) \ . \tag{A.6}$$

However, since in the incompressible framework,

$$\nabla.u = 0 \ , \tag{A.7}$$

we can again write

$$\frac{\partial \rho}{\partial t} = \frac{D\rho}{Dt} - u.\nabla\rho \ . \tag{A.8}$$

Therefore, for either framework, we have:

$$\frac{\partial(GPE_A)}{\partial t} = \rho(z_s)g\big(z_s - z_0\big)w(z_s) + \int_{-H}^{z_s} g\big(z - z_0\big)\left(\frac{D\rho}{Dt} - u.\nabla\rho\right)\mathrm{d}z \ . \tag{A.9}$$

Spurious generation of mass results from calculating a vertical velocity field that is consistent with the horizontal velocity field under the incompressible continuity equation. From (A.7) the vertical velocity in the incompressible framework is

$$w^v = \int -\nabla_h.u_h\mathrm{d}z \ . \tag{A.10}$$

From (A.4) the vertical velocity in the compressible framework is

$$w^m = \int \left(-\nabla_h.u_h - \frac{1}{\rho}\frac{D\rho}{Dt}\right)\mathrm{d}z \ . \tag{A.11}$$

We can treat the difference between w^v and w^m, as an error in vertical velocity, w^e

$$w^e(z) = w^v(z) - w^m(z) = \int_{-H}^{z} \frac{1}{\rho}\frac{D\rho}{Dt}\mathrm{d}Z \ , \tag{A.12}$$

where we have used $w^v(-H) = w^m(-H) = 0$.

We can now determine the error in GPE generation, $\partial(GPE^e_A)/\partial t$:

$$\begin{aligned}\frac{\partial(GPE^e_A)}{\partial t} &= \rho(z_s)g\big(z_s - z_0\big)w^e(z_s) - \int_{-H}^{z_s} g\big(z - z_0\big)w^e\frac{\partial\rho}{\partial z}\mathrm{d}z \\ &= \rho(z_s)g\big(z_s - z_0\big)\int_{-H}^{z_s}\frac{1}{\rho}\frac{D\rho}{Dt}\mathrm{d}z - \int_{-H}^{z_s} g\big(z - z_0\big)\frac{\partial\rho}{\partial z}\int_{-H}^{z}\frac{1}{\rho}\frac{D\rho}{Dt}\mathrm{d}Z\ \mathrm{d}z\end{aligned} \tag{A.13}$$

Visual inspection of the RHS of (A.13) reveals that, unless z_0 is chosen to be close to z_s, the ratio of the magnitude of the second term to that of the first term is $O\big(\frac{\rho(-H)-\rho(z_s)}{\rho}\big) = O(10^{-2})$. The first term is the leading order effect of spurious generation of mass. The second term arises due to the small inhomogeneity in

ocean density, and is therefore comparable in nature and magnitude to errors in dynamical calculations introduced through the Boussinesq approximation. The priority must be to minimise the error due to the first term. This is zero provided that $z_0 = z_s$. Therefore, the surface, or a geopotential near the surface in cases where models have an explicit free surface, should always be used as the reference level in GPE budget calculations within the incompressible framework.

Bibliography

Aiki, H. and Richards, K. J. (2008). Energetics of the Global Ocean: The Role of Layer-Thickness Form Drag. *Journal of Physical Oceanography*, 38(9):1845–1869.

Brunnabend, S.-E., Dijkstra, H. A., Kliphuis, M. A., van Werkhoven, B., Bal, H. E., Seinstra, F., Maassen, J., and van Meersbergen, M. (2014). Changes in extreme regional sea surface height due to an abrupt weakening of the Atlantic meridional overturning circulation. *Ocean Science*, 10(6):881–891.

Bryden, H. L., King, B. A., McCarthy, G. D., and McDonagh, E. L. (2014). Impact of a 30% reduction in Atlantic meridional overturning during 20092010. *Ocean Science*, 10(4):683–691.

Butler, E. D., Oliver, K. I., Gregory, J. M., and Tailleux, R. (2013). The ocean's gravitational potential energy budget in a coupled climate model. *Geophysical Research Letters*, 40:5417–5422.

Cunningham, S. A., Kanzow, T., Rayner, D., Baringer, M. O., Johns, W. E., Marotzke, J., Longworth, H. R., Grant, E. M., Hirschi, J. J.-M., Beal, L. M., Meinen, C. S., and Bryden, H. L. (2007). Temporal variability of the Atlantic meridional overturning circulation at 26.5 degrees N. *Science*, 317(5840):935–8.

Cunningham, S. A., Roberts, C. D., Frajka-Williams, E., Johns, W. E., Hobbs, W., Palmer, M. D., Rayner, D., Smeed, D. A., and McCarthy, G. (2013). Atlantic Meridional Overturning Circulation slowdown cooled the subtropical ocean. *Geophysical Research Letters*, 40(23):2013GL058464.

Czeschel, L., Marshall, D. P., and Johnson, H. L. (2010). Oscillatory sensitivity of Atlantic overturning to high-latitude forcing. *Geophysical Research Letters*, 37(10).

de Boer, A. M., Gnanadesikan, A., Edwards, N. R., and Watson, A. J. (2010). Meridional Density Gradients Do Not Control the Atlantic Overturning Circulation. *Journal of Physical Oceanography*, 40(2):368–380.

Delworth, T. L. and Greatbatch, R. J. (2000). Multidecadal thermohaline circulation variability driven by atmospheric surface flux forcing. *Journal of Climate*, 13:1481–1495.

Dijkstra, H. A. (2008). Scaling of the Atlantic meridional overturning circulation in a global ocean model. *Tellus A*, 60(4):749–760.

Dijkstra, H. A., Saenz, J. A., and McC. Hogg, A. (2014). Energetics of Multidecadal Atlantic Ocean Variability. *Journal of Climate*, 27(20):7874–7889.

Dong, B.-W. and Sutton, R. T. (2002). Adjustment of the coupled oceanatmosphere system to a sudden change in the Thermohaline Circulation. *Geophysical Research Letters*, 29(15):14–18.

Downes, S. M. and Hogg, A. M. (2013). Southern Ocean Circulation and Eddy Compensation in CMIP5 Models. *Journal of Climate*, 26(18):7198–7220.

Fürst, J. J. and Levermann, A. (2011). A minimal model for wind- and mixing-driven overturning: threshold behavior for both driving mechanisms. *Climate Dynamics*, 38(1-2):239–260.

Fučkar, N. S. and Vallis, G. K. (2007). Interhemispheric influence of surface buoyancy conditions on a circumpolar current. *Geophysical Research Letters*, 34(14):L14605.

Ganachaud, A. and Wunsch, C. (2000). Improved estimates of global ocean circulation, heat transport and mixing from hydrographic data. *Nature*, 408:453–457.

Ganachaud, A. and Wunsch, C. (2003). Large-scale ocean heat and freshwater transports during the World Ocean Circulation Experiment. *Journal of Climate*, 16:696–705.

Ganopolski, A. and Rahmstorf, S. (2001). Rapid changes of glacial climate simulated in a coupled climate model. *Nature*, 409(6817):153–8.

Gent, P. and McWilliams, J. (1990). Isopycnal mixing in ocean circulation models. *Journal of Physical Oceanography*, 20:150–155.

Gnanadesikan, A. (1999). A simple predictive model for the structure of the oceanic pycnocline. *Science*, 283(5410):2077–2079.

Gnanadesikan, A., de Boer, A. M., and Mignone, B. (2007). A simple theory of the pycnocline and overturning revisited. In Schmittner, A., Chiang, J. C. H., and Hemming, S. R., editors, *Ocean Circulation: Mechanisms and Impacts - Past and Future Changes of Meridional Overturning*. American Geophysical Union, Washington, D. C.

Gnanadesikan, A., Slater, R. D., Swathi, P. S., and Vallis, G. K. (2005). The Energetics of Ocean Heat Transport. *Journal of Climate*, 18(14):2604–2616.

Gordon, C., Cooper, C., Senior, C. A., Banks, H., Gregory, J. M., Johns, T. C., Mitchell, J. F. B., and Wood, R. A. (2000). The simulation of SST, sea ice extents and ocean heat transports in a version of the Hadley Centre coupled model without flux adjustments. *Climate Dynamics*, 16(2-3):147–168.

Gregory, J. M. and Tailleux, R. (2011). Kinetic energy analysis of the response of the Atlantic meridional overturning circulation to CO2-forced climate change. *Climate Dynamics*, 37(5-6):893–914.

Griesel, A. and Maqueda, M. A. M. (2006). The relation of meridional pressure gradients to North Atlantic deep water volume transport in an ocean general circulation model. *Climate Dynamics*, 26(7-8):781–799.

Griffies, S., Pacanowski, R., and Hallberg, R. (2000). Spurious diapycnal mixing associated with advection in a z-coordinate ocean model. *Monthly Weather Review*, 128:538–564.

Griffies, S. and Tziperman, E. (1995). A linear thermohaline oscillator driven by stochastic atmospheric forcing. *Journal of Climate*, 8(10):2440–2453.

Hawkins, E., Smith, R. S., Allison, L. C., Gregory, J. M., Woollings, T. J., Pohlmann, H., and de Cuevas, B. (2011). Bistability of the Atlantic overturning circulation in a global climate model and links to ocean freshwater transport. *Geophysical Research Letters*, 38(10):n/a–n/a.

Hirschi, J. J.-M., Killworth, P. D., and Blundell, J. R. (2007). Subannual, Seasonal, and Interannual Variability of the North Atlantic Meridional Overturning Circulation. *Journal of Physical Oceanography*, 37(5):1246–1265.

Hogg, A. M., Dijkstra, H. A., and Saenz, J. A. (2013). The Energetics of a Collapsing Meridional Overturning Circulation. *Journal of Physical Oceanography*, 43(7):1512–1524.

Huang, R. X. (1998). Mixing and Available Potential Energy in a Boussinesq Ocean*. *Journal of Physical Oceanography*, 28(4):669–678.

Huang, R. X. (1999). Mixing and Energetics of the Oceanic Thermohaline Circulation*. *Journal of Physical Oceanography*, 29(4):727–746.

Huang, R. X. (2005). Available potential energy in the world's oceans. *Journal of Marine Research*, 63(1):141–158.

Huang, R. X., Cane, M. A., Naik, N., and Goodman, P. (2000). Global adjustment of the thermocline in response to deepwater formation. *Geophysical Research Letters*, 27(6):759–762.

Huang, R. X. and Jin, X. (2006). Gravitational Potential Energy Balance for the Thermal Circulation in a Model Ocean. *Journal of Physical Oceanography*, 36(7):1420–1429.

Hughes, G. O., Hogg, A. M., and Griffiths, R. W. (2009). Available Potential Energy and Irreversible Mixing in the Meridional Overturning Circulation. *Journal of Physical Oceanography*, 39(12):3130–3146.

Hughes, T. M. C. and Weaver, A. J. (1994). Multiple Equilibria of an Asymmetric Two-Basin Ocean Model. *Journal of Physical Oceanography*, 24(3):619–637.

Jackson, L. and Vellinga, M. (2013). Multidecadal to Centennial Variability of the AMOC: HadCM3 and a Perturbed Physics Ensemble. *Journal of Climate*, 26(7):2390–2407.

Johns, W. E., Baringer, M. O., Beal, L. M., Cunningham, S. A., Kanzow, T., Bryden, H. L., Hirschi, J. J. M., Marotzke, J., Meinen, C. S., Shaw, B., and Curry, R. (2011). Continuous, Array-Based Estimates of Atlantic Ocean Heat Transport at 26.5N. *Journal of Climate*, 24(10):2429–2449.

Johnson, H. L. and Marshall, D. P. (2002). A theory for the surface Atlantic response to thermohaline variability. *Journal of Physical Oceanography*, 32(4).

Johnson, H. L. and Marshall, D. P. (2004). Global Teleconnections of Meridional Overturning Circulation Anomalies. *Journal of Physical Oceanography*, 34:1702–1722.

Johnson, H. L., Marshall, D. P., and Sproson, D. A. J. (2007). Reconciling theories of a mechanically driven meridional overturning circulation with thermohaline forcing and multiple equilibria. *Climate Dynamics*, 29(7-8):821–836.

Kanzow, T., Johnson, H. L., Marshall, D. P., Cunningham, S. A., Hirschi, J. J.-M., Mujahid, A., Bryden, H. L., and Johns, W. E. (2009). Basinwide Integrated Volume Transports in an Eddy-Filled Ocean. *Journal of Physical Oceanography*, 39(12):3091–3110.

Knight, J. R. (2005). A signature of persistent natural thermohaline circulation cycles in observed climate. *Geophysical Research Letters*, 32(20):L20708.

Kostov, Y., Armour, K. C., and Marshall, J. (2014). Impact of the Atlantic meridional overturning circulation on ocean heat storage and transient climate change. *Geophysical Research Letters*, 41(6):2108–2116.

Kuhlbrodt, T., Griesel, A., Montoya, M., Levermann, A., Hofmann, M., and Rahmstorf, S. (2007). On the driving processes of the Atlantic meridional overturning circulation. *Reviews of Geophysics*, 45(2).

Large, W. G. and Yeager, S. G. (2004). Diurnal to decadal global forcing for ocean and sea-ice models - the data sets and flux climatologies. *NCAR Technical Note NCAR/TN-460+STR*.

Large, W. G. and Yeager, S. G. (2008). The global climatology of an interannually varying airsea flux data set. *Climate Dynamics*, 33(2-3):341–364.

Large, W. G. and Yeager, S. G. (2009). The global climatology of an interannually varying airsea flux data set. *Climate Dynamics*, 33(2-3):341–364.

Levermann, A. and Fürst, J. J. (2010). Atlantic pycnocline theory scrutinized using a coupled climate model. *Geophysical Research Letters*, 37(14):L14602.

Lorenz, E. N. (1955). Available Potential Energy and the Maintenance of the General Circulation. *Tellus*, 7(2):157–167.

Lucas, M. A., Hirschi, J. J.-M., Stark, J. D., and Marotzke, J. (2005). The response of an idealized ocean basin to variable buoyancy forcing. *Journal of Physical Oceanography*, 35:601–615.

Lumpkin, R. and Speer, K. (2007). Global Ocean Meridional Overturning. *Journal of Physical Oceanography*, 37(10):2550–2562.

Madec, G. (2008). *NEMO ocean engine*. Institut Pierre-Simon Laplace (IPSL), France, ISSN No 1288-1619.

Manabe, S. and Stouffer, R. (1988). Two stable equilibria of a coupled ocean-atmosphere model. *Journal of Climate*, 1:841–866.

Marcos, M. and Tsimplis, M. N. (2008). Comparison of results of AOGCMs in the Mediterranean Sea during the 21st century. *Journal of Geophysical Research*, 113(C12):C12028.

Marotzke, J. (1997). Boundary mixing and the dynamics of three-dimensional thermohaline circulation. *Journal of Physical Oceanography*, 27:1713–1728.

Marshall, D. P. and Johnson, H. L. (2013). Propagation of Meridional Circulation Anomalies along Western and Eastern Boundaries. *Journal of Physical Oceanography*, 43(12):2699–2717.

Marshall, J. and Radko, T. (2003). Residual-Mean Solutions for the Antarctic Circumpolar Current and Its Associated Overturning Circulation. *Journal of Physical Oceanography*, 33(11):2341–2354.

McCarthy, G., Frajka-Williams, E., Johns, W. E., Baringer, M. O., Meinen, C. S., Bryden, H. L., Rayner, D., Duchez, A., Roberts, C., and Cunningham, S. a. (2012). Observed interannual variability of the Atlantic meridional overturning circulation at 26.5N. *Geophysical Research Letters*, 39(19).

Mecking, J. V., Keenlyside, N. S., and Greatbatch, R. J. (2014). Stochastically-forced multidecadal variability in the North Atlantic: a model study. *Climate Dynamics*, 43(1-2):271–288.

Munday, D. R., Allison, L. C., Johnson, H. L., and Marshall, D. P. (2011). Remote forcing of the Antarctic Circumpolar Current by diapycnal mixing. *Geophysical Research Letters*, 38:L08609.

Munk, W. and Wunsch, C. (1998). Abyssal recipes II: energetics of tidal and wind mixing. *Deep Sea Research Part I: Oceanographic Research Papers*, 45(12):1977–2010.

Nilsson, J. and Walin, G. (2001). Freshwater forcing as a booster of thermohaline circulation. *Tellus A*, 53:629–641.

Oliver, K. I. C. and Edwards, N. R. (2008). Location of potential energy sources and the export of dense water from the Atlantic Ocean. *Geophysical Research Letters*, 35(22):1–17.

Oliver, K. I. C., Watson, A. J., and Stevens, D. P. (2005). Can limited ocean mixing buffer rapid climate change? *Tellus A*, 57(4):676–690.

Park, Y.-G. and Bryan, K. (2000). Comparison of Thermally Driven Circulations from a Depth-Coordinate Model and an Isopycnal-Layer Model. Part I: Scaling-Law Sensitivity to Vertical Diffusivity. *J Phys Oceanogr*, 30:590–605.

Rahmstorf, S. (1996). On the freshwater forcing and transport of the Atlantic thermohaline circulation. *Climate Dynamics*, 12(12):799–811.

Rahmstorf, S. (2002). Ocean circulation and climate during the past 120,000 years. *Nature*, 419(6903):207–214.

Rahmstorf, S., Crucifix, M., Ganopolski, A., Goosse, H., Kamenkovich, I., Knutti, R., Lohmann, G., Marsh, R., Mysak, L. A., Wang, Z., and Weaver, A. J. (2005). Thermohaline circulation hysteresis: A model intercomparison. *Geophysical Research Letters*, 32(23):L23605.

Rahmstorf, S. and Ganopolski, A. (1999). Long-term global warming scenarios computed with an efficient coupled climate model. *Climatic Change*, 43(2):353–367.

Roberts, C., Jackson, L., and McNeall, D. (2014). Is the 20042012 reduction of the Atlantic meridional overturning circulation significant? *Geophysical Research Letters*, 41:3204–3210.

Rocha, J., Yletyinen, J., Biggs, R., Blenckner, T., and Peterson, G. (2015). Marine regime shifts: drivers and impacts on ecosystems services. *Philosophical Transactions of the Royal Society B: Biological Sciences*, 370:20130273.

Saenko, O. A. (2013). Energetics of weakening and recovery of the Atlantic overturning in a climate change simulation. *Geophysical Research Letters*, 40(5):888–892.

Saenz, J. A., Hogg, A. M., Hughes, G. O., and Griffiths, R. W. (2012). The mechanical power input from buoyancy and wind in an ocean model. *Geophysical Research Letters*, 39(13).

Saenz, J. A., Tailleux, R., Butler, E. D., Hughes, G. O., and Oliver, K. I. C. (2015). Estimating Lorenzs reference state in an ocean with a non-linear equation of state for seawater (in press). *Journal of Physical Oceanography*.

Samelson, R. (2004). Simple mechanistic models of middepth meridional overturning. *Journal of Physical Oceanography*, 34:2096–2103.

Sandström, J. (1908). Dynamische Versuche mit Meerwasser. *Annals in Hydrodynamic Marine Meteorology*, 36:6–23.

Schewe, J. and Levermann, A. (2009). The role of meridional density differences for a wind-driven overturning circulation. *Climate Dynamics*, 34(4):547–556.

Schmittner, A. (2005). Decline of the marine ecosystem caused by a reduction in the Atlantic overturning circulation. *Nature*, 434:628–633.

Sijp, W. P., Gregory, J. M., Tailleux, R., and Spence, P. (2012). The Key Role of the Western Boundary in Linking the AMOC Strength to the North South Pressure Gradient. *Journal of Physical Oceanography*, 42(4):628–643.

Smeed, D. A., McCarthy, G. D., Cunningham, S. A., Frajka-Williams, E., Rayner, D., Johns, W. E., Meinen, C. S., Baringer, M. O., Moat, B. I., Duchez, A., and Bryden, H. L. (2014). Observed decline of the Atlantic meridional overturning circulation 20042012. *Ocean Science*, 10(1):29–38.

Smith, R. S., Gregory, J. M., and Osprey, A. (2008). A description of the FAMOUS (version XDBUA) climate model and control run. *Geoscientific Model Development*, 1:53–68.

Sonnewald, M., Hirschi, J. J.-M., Marsh, R., McDonagh, E. L., and King, B. A. (2013). Atlantic meridional ocean heat transport at 26 N: impact on subtropical ocean heat content variability. *Ocean Science*, 9(6):1057–1069.

Srokosz, M., Baringer, M., Bryden, H., Cunningham, S., Delworth, T., Lozier, S., Marotzke, J., and Sutton, R. (2012). Past, Present, and Future Changes in the Atlantic Meridional Overturning Circulation. *Bulletin of the American Meteorological Society*, 93(11):1663–1676.

Stewart, K., Saenz, J., Hogg, A., Hughes, G., and Griffiths, R. (2014). Effect of topographic barriers on the rates of available potential energy conversion of the oceans. *Ocean Modelling*, 76:31–42.

Stocker, T. F., Qin, D., Plattner, G.-K., Tignor, M., Allen, S., Boschung, J., Nauels, A., Xia, Y., Bex, V., and Midgley, P. (2013). *IPCC, 2013: Climate Change 2013: The Physical Science Basis. Contribution of Working Group I to the Fifth Assessment Report of the Intergovernmental Panel on Climate Change*. Cambridge University Press, Cambridge, United Kingdom and New York, NY, USA.

Stommel, H. (1961). Thermohaline Convection with Two Stable Regimes of Flow. *Tellus*, 13(2):224–230.

Stouffer, R. J., Yin, J., Gregory, J. M., Dixon, K. W., Spelman, M. J., Hurlin, W., Weaver, A. J., Eby, M., Flato, G. M., Hasumi, H., Hu, A., Jungclaus, J. H., Kamenkovich, I. V., Levermann, A., Montoya, M., Murakami, S., Nawrath, S., Oka, A., Peltier, W. R., Robitaille, D. Y., Sokolov, A., Vettoretti, G., and Weber, S. L. (2006). Investigating the Causes of the Response of the Thermohaline Circulation to Past and Future Climate Changes. *Journal of Climate*, 19(8):1365–1387.

Tailleux, R. (2009). On the energetics of stratified turbulent mixing, irreversible thermodynamics, Boussinesq models, and the ocean heat engine controversy. *Journal of Fluid Mechanics*, 638:339–382.

Tailleux, R. (2010). Entropy versus APE production: On the buoyancy power input in the oceans energy cycle. *Geophysical Research Letters*, 37(22):1–5.

Tailleux, R. (2013a). Available Potential Energy and Exergy in Stratified Fluids. *Annual Review of Fluid Mechanics*, 45(1):35–58.

Tailleux, R. (2013b). Available potential energy density for a multicomponent Boussinesq fluid with arbitrary nonlinear equation of state. *Journal of Fluid Mechanics*, 735:499–518.

Thomas, M. D. and Zhai, X. (2013). Eddy-induced variability of the meridional overturning circulation in a model of the North Atlantic. *Geophysical Research Letters*, 40(11):2742–2747.

Thorpe, R. B., Gregory, J. M., Johns, T. C., Wood, R. A., and Mitchell, J. F. B. (2001). Mechanisms Determining the Atlantic Thermohaline Circulation Response to Greenhouse Gas Forcing in a Non-Flux-Adjusted Coupled Climate Model. *Journal of Climate*, 14:3102–3116.

Toggweiler, J. and Samuels, B. (1995). Effect of Drake Passage on the global thermohaline. *Deep Sea Research Part I: Oceanographic Research Papers*, 42(4):477–500.

Toggweiler, J. R. and Samuels, B. (1998). On the Ocean's Large-Scale Circulation near the Limit of No Vertical Mixing. *Journal of Physical Oceanography*, 28(9):1832–1852.

Urakawa, L. S. and Hasumi, H. (2009). The Energetics of Global Thermohaline Circulation and Its Wind Enhancement. *Journal of Physical Oceanography*, 39(7):1715–1728.

Vellinga, M. and Wood, R. A. (2002). Global climatic impacts of a collapse of the Atlantic thermohaline circulation. *Climatic Change*, 54(3):251–267.

Vellinga, M. and Wu, P. (2004). Low-latitude freshwater influence on centennial variability of the Atlantic thermohaline circulation. *Journal of Climate*, 17:4498–4511.

Visbeck, M., Marshall, J., Haine, T., and Spall, M. (1997). Specification of eddy transfer coefficients in coarse-resolution ocean circulation models*. *Journal of Physical Oceanography*, 27:381–402.

Webb, D. and Suginohara, N. (2001). Oceanography: Vertical mixing in the ocean. *Nature*, 409(January).

Winters, K., Lombard, P., and Riley, J. (1995). Available potential energy and mixing in density-stratified fluids. *Journal of Fluid Mechanics*, 289:115–128.

Winters, K. B. and Barkan, R. (2013). Available potential energy density for Boussinesq fluid flow. *Journal of Fluid Mechanics*, 714:476–488.

Wright, D. G., Vreugdenhil, C. B., and Hughes, T. M. C. (1995). Vorticity dynamics and zonally averaged ocean circulation models. *Journal of Physical Oceanography*, 25:2141–2154.

Wu, J., Oliver, K. I. C., Butler, E. D., Gregory, J. M., and Kuhlbrodt, T. (2015). The response of the ocean's gravitational potential energy budget to CO2-forced climate change (in preparation).

Wunsch, C. (1998). The work done by the wind on the oceanic general circulation. *Journal of Physical Oceanography*, pages 2332–2340.

Wunsch, C. (2002). What is the thermohaline circulation? *Science*, 298(5596):1179–1181.

Wunsch, C. and Ferrari, R. (2004). Vertical Mixing, Energy, and the General Circulation of the Oceans. *Annual Review of Fluid Mechanics*, 36(1):281–314.

Zickfeld, K., Eby, M., and Weaver, A. J. (2008). Carbon-cycle feedbacks of changes in the Atlantic meridional overturning circulation under future atmospheric CO2. *Global Biogeochemical Cycles*, 22:GB3024.